SMRT | A WORLD OF KNOWLEDGE
FOR MR TECHNOLOGISTS & RADIOGRAPHERS

SECTION FOR MAGNETIC RESONANCE TECHNOLOGISTS
OF THE INTERNATIONAL SOCIETY FOR MAGNETIC RESONANCE IN MEDICINE

Home Studies Educational Seminars

VOLUME 17 • NUMBER 3

Musculoskeletal MRI: Cartilage and Ligaments

Editor, SMRT Educational Seminars, Home Study Program

Anne Marie Sawyer, B.S., R.T.(R)(MR), FSMRT
Home Study Program
Lucas Center for Imaging
Stanford University, Stanford, California, USA
T: +1 650 725 9697
E: amsawyer@stanford.edu

Chair, SMRT Publications Committee

Vanessa Orchard, DCR(D), PGDip.(Nuc Med), M.Sc.(MRI)
Lead Radiographer
Cardiac Imaging Centre
Golden Jubilee National Hospital
Dunbartonshire, Glasgow, Scotland, UK
T: +0141 951 5187
E: vanessa.orchard@gjnh.scot.nhs.uk

Musculoskeletal MRI: Cartilage and Ligaments

July 2014

We are pleased to present the SMRT Educational Seminars, Volume 17, Number 3: "Musculoskeletal MRI: Cartilage and Ligaments." This is the 65th accredited Home Study developed by the SMRT, exclusively for SMRT members. The accreditation is conducted by the SMRT acting as a RCEEM (Recognized Continuing Education Evaluation Mechanism) for the ARRT. Category A credits are assigned to each Home Study, which can be used to maintain one's ARRT advanced registry. SMRT Home Studies are also approved for AIR (Australian Institute of Radiography), NZIMRT (New Zealand Institute of Radiation Technology) and CPD Now (The College of Radiographers, United Kingdom) continuing professional development (CPD) activities.

Three peer-reviewed articles have been chosen for this home study issue. As introduced in the first article, "The complex osseous geometry of the wrist combined with the thin articular cartilage, poses challenges for consistent diagnostic imaging." The authors outline the "technical aspects of performing high-resolution MRI of the wrist. The use of MRI in detecting osseous pathologies such as occult fractures, osteonecrosis, and abutment syndromes is discussed. The role of MRI in assessing articular cartilage defects and the MRI appearance of osteoarthritis and inflammatory arthropathies is reviewed."

The authors of the second article tell us "Cartilage is one of the most essential tissues for healthy joint function and is compromised in degenerative and traumatic joint disease." After reviewing cartilage composition and degeneration, methods are discussed that "grade and quantify morphologic changes as well as the techniques that quantify changes in the extracellular matrix." Given the increasing focus on the wide spread effects of osteoarthritis (OA), this is an especially timely article as testimony that "quantitative MRI provides noninvasive measures of cartilage degeneration at the earliest stages of joint degeneration, which is essential for efforts towards prevention and early intervention of OA."

"Quantitative MRI provides noninvasive measures of cartilage degeneration at the earliest stages of joint degeneration, which is essential for efforts towards prevention and early intervention of OA."

In the third and final article, the authors focus on injury and reconstruction of ligaments in the knee. "Knee ligament instability may lead to meniscal and chondral damage, resulting in early osteoarthritis." This article aims to provide an understanding of "MRI appearances of knee ligament structures associated with knee instability, and to review the common patterns of altered knee mechanics that lead to ligament failure."

A special thank you to Steven P. Shannon, R.T.(R)(MR) from Cambridge, Massachusetts, USA for acting as the Expert Reviewer.

Thanks also to Heidi Berns, M.S., R.T.(R)(MR), FSMRT, Chair of the SMRT RCEEM Ad-hoc committee from Coralville, Iowa, USA and all those who participate on this committee by reviewing the home studies for accreditation. Finally, many thanks to Jennifer Olson, Associate Executive Director; Mary Keydash, Publications Director; Linda O-Brown, SMRT Coordinator; Sally Moran, Director of Electronic Communications and the entire staff in the Berkeley, California, USA office of the ISMRM and SMRT for their insight and long hours spent supporting these educational symposia.

It is with great sadness that I acknowledge that this particular Home Study is the last issue that the SMRT Publications Committee, chair Vanessa Orchard from Scotland and I as the Home Study sub-committee chair will create with Jennifer Olson. Since 1990 Jennifer has provided enormous support and valuable direction for the Technologists' section of the ISMRM, the SMRT. Jennifer has been our non-stop resource to ensure that the SMRT continues to grow not only their membership, but also their educational offerings for the membership. She has constantly cultivated ideas on how to better serve the SMRT members. Jennifer has been relentless when it comes to providing quality education for MR Technologists and Radiographers. We will miss her terribly but know that she is off to a new and rewarding chapter in her life and congratulate her for it. And thank, thank, thank Jennifer a millions times over for all her hard work and long hours spent supporting education for MR Technologists and Radiographers.

Musculoskeletal MRI: Cartilage and Ligaments

SECTION FOR MAGNETIC RESONANCE TECHNOLOGISTS

Home Studies *Educational Seminars* VOLUME 17 • NUMBER 3

Educational Objectives

Magnetic Resonance Imaging of the Wrist: Bone and Cartilage Injury

- Describe technical considerations including coils and patient positioning, imaging at 3T, and pulse sequences and scan protocols;
- Discuss osseus abnormalities including scaphoid fractures and complications, carpal bone fractures, stress fractures and Gymnast's Wrist, avascular necrosis, and impaction/ impingement syndromes;
- Review cartilage imaging and the SLAC/SNAC wrist including osteoarthritis, and inflammatory arthropathies; and
- Show image examples of osseus abnormalities including fractures, and cartilage imaging to look at osteoarthritis and other inflammatory processes.

Quantitative MRI of Articular Cartilage and Its Clinical Applications

- Review cartilage composition and degeneration;
- Describe morphological changes in cartilage in osteoarthritis;
- Discuss quantitative MRI for cartilage matrix composition;
- Explain the use of postcontrast T1 relaxation time by delayed gadolinium-enhanced proton MRI of cartilage;
- Describe T2 relaxation time including basic principles and in vivo applications;
- Review T1r relaxation time quantification including basic principles and *in vivo* applications;

(Quantitative MRI of Articular Cartilage.... continued)

- Discuss other cartilage MR imaging methods including Magnetization Transfer (MT), Chemical Exchange-Dependent Saturation Transfer (CEST), Diffusion, sodium, and Ultra Short Echo (UTE); and
- Show image examples of all acquisition methods, proton and sodium.

MRI of Knee Ligament Injury and Reconstruction

- MRI of Knee Ligament Injury and Reconstruction;
- Describe the Anterior Cruciate Ligament (ACL) including anatomy and normal appearance, tears, and ganglion cysts;
- Review reconstruction of the ACL including grafts and complications;
- Discuss the Posterior Cruciate LIgament (PCL) including anatomy and normal appearance, and tears;
- Describe reconstruction of the PCL;
- Review the Medial Collateral Ligament (MCL) including anatomy and normal appearance, pathology, and reconstruction;
- Explain the Posterolateral Corner (PLC) including anatomy and normal appearance, and pathologic appearance; and
- Show image examples of the ACL, PCL and MCl including tears, pathology and post-reconstruction.

Expert Reviewer

Steven P. Shannon, RT (R)(MR)
Operations Manager/MR Research Technologist
Athinoula A. Martinos Imaging Center
McGovern Institute for Brain Research
Massachusetts Institute of Technology
Cambridge, Massachusetts USA

NZIMRT APPROVED CPD ACTIVITY
SMRT Home Studies, Online Electronic Studies & Online Video Studies
Credits: 1 per activity, max of 6/yr
Valid: 2014

Accreditation by cpd now the College of Radiographers

ENDORSED BY THE COLLEGE OF RADIOGRAPHERS - UNITED KINGDOM
Credit levels according to SMRT certificate - Valid 2012 - 2014
CoR Assessment: A combined programme covering a wide range of clinical applications and current issues in MR imaging.
May support outcomes 1-13, 18 and 19 of CPD Now

Magnetic Resonance Imaging of the Wrist: Bone and Cartilage Injury

Catherine L. Hayter, MBBS,[1] Stephanie L. Gold, B.A.,[1] and Hollis G. Potter, M.D.[1,2*]

Reprinted from the ISMRM Journal of Magnetic Resonance Imaging: Volume 37: Pages: 1005-1019, © 2013 from Wiley Periodicals, Inc.

This article is accredited as a journal-based CME activity. If you wish to receive credit for this activity, please refer to the website: www.wileyhealthlearning.com

ACCREDITATION AND DESIGNATION STATEMENT

Blackwell Futura Media Services designates this journal-based CME activity for a maximum of 1 *AMA PRA Category 1 Credit*™. Physicians should only claim credit commensurate with the extent of their participation in the activity.

Blackwell Futura Media Services is accredited by the Accreditation Council for Continuing Medical Education to provide continuing medical education for physicians.

EDUCATIONAL OBJECTIVES

Upon completion of this educational activity, participants will be better able to describe the technical aspects of performing high-resolution MRI of the wrist.

ACTIVITY DISCLOSURES

No commercial support has been accepted related to the development or publication of this activity.

Faculty Disclosures:

The following contributors have no conflicts of interest to disclose:

Editor-in-Chief: C. Leon Partain, MD, PhD

CME Editor: Scott B. Reeder, MD, PhD

CME Committee: Scott Nagle, MD, PhD, Pratik Mukherjee, MD, PhD, Shreyas Vasanawala, MD, PhD, Bonnie Joe, MD, PhD, Tim Leiner, MD, PhD, Sabine Weckbach, MD, Frank Korosec, PhD

Authors: Catherine L. Hayter, MBBS, Stephanie L. Gold, BA, Hollis G. Potter, MD

This manuscript underwent peer review in line with the standards of editorial integrity and publication ethics maintained by *Journal of Magnetic Resonance Imaging*. The peer reviewers have no relevant financial relationships. The peer review process for *Journal of Magnetic Resonance Imaging* is double-blinded. As such, the identities of the reviewers are not disclosed in line with the standard accepted practices of medical journal peer review.

Conflicts of interest have been identified and resolved in accordance with Blackwell Futura Media Services's Policy on Activity Disclosure and Conflict of Interest. No relevant financial relationships exist for any individual in control of the content and therefore there were no conflicts to resolve.

INSTRUCTIONS ON RECEIVING CREDIT

For information on applicability and acceptance of CME credit for this activity, please consult your professional licensing board.

This activity is designed to be completed within an hour; physicians should claim only those credits that reflect the time actually spent in the activity. To successfully earn credit, participants must complete the activity during the valid credit period.

Follow these steps to earn credit:

- Log on to www.wileyhealthlearning.com
- Read the target audience, educational objectives, and activity disclosures.
- Read the article in print or online format.
- Reflect on the article.
- Access the CME Exam, and choose the best answer to each question.
- Complete the required evaluation component of the activity.

This activity will be available for CME credit for twelve months following its publication date. At that time, it will be reviewed and potentially updated and extended for an additional period.

[1]Department of Radiology and Imaging, Hospital for Special Surgery, New York, New York, USA.
[2] Weill Cornell Medical College of Cornell University, New York, New York, USA.
*Address reprint requests to: H.G.P., Department of Radiology and Imaging, Hospital for Special Surgery, 535 East 70th St., New York, NY 10021. E-mail: potterh@hss.edu
Received September 16, 2011; Accepted August 29, 2012.
DOI 10.1002/jmri.23845
View this article online at wileyonlinelibrary.com.

Magnetic resonance imaging (MRI) is particularly useful for imaging the wrist due to its superior soft tissue contrast and ability to detect subtle bone marrow changes and occult fractures. A high field (1.5T or greater) strength, dedicated wrist coil, and high in-plane and through-plane resolution must be utilized to successfully visualize the relatively thin cartilage of the wrist. MRI can be used to detect occult carpal bone fractures, identify complications following scaphoid fractures, and assess for avascular necrosis in the setting in Kienböck's and Preiser's disease. MRI is useful to identify secondary soft tissue and chondral pathology in impaction/impingement syndromes. The use of an intermediate-echo time fast spin echo sequence allows for accurate assessment of articular cartilage, allowing evaluation of chondral wear in the setting of primary osteoarthritis and posttraumatic degenerative arthrosis. MRI is the most sensitive imaging modality for the detection of early inflammatory arthropathies and can detect synovitis, bone marrow edema, and early erosions in the setting of negative radiographs.

Key Words: magnetic resonance imaging; wrist; cartilage; ulnar impaction; Kienböck's disease; arthritis
J. Magn. Reson. Imaging 2013;37:1005–1019.

THE COMPLEX OSSEOUS GEOMETRY of the wrist, combined with the thin articular cartilage, poses challenges for consistent diagnostic imaging. Due to its superior soft tissue contrast, direct multiplanar capabilities, and ability to detect subtle bone marrow changes, magnetic resonance imaging (MRI) is particularly useful for imaging the wrist.

This article outlines the technical aspects of performing high-resolution MRI of the wrist. The use of MRI in detecting osseous pathologies such as occult fractures, osteonecrosis, and abutment syndromes is discussed. The role of MRI in assessing articular cartilage defects and the MRI appearance of osteoarthritis and inflammatory arthropathies is reviewed.

TECHNICAL CONSIDERATIONS

Coils and Patient Positioning

High-quality MRI of the wrist is technically challenging, due to the high spatial resolution and signal-to-noise ratio (SNR) that are required to visualize the small structures of the wrist. Use of a high field strength magnet with a dedicated surface coil is essential to achieve adequate SNR (1). A small field of view (FOV; 8–10 cm) and thin (1–2 mm) contiguous sections are required for adequate assessment, as the cartilage of the wrist is thin and many of the intrinsic wrist ligaments are no more than 1–2 mm thick (2).

It is the authors' preference to image the wrist with the arm at the patient's side, the elbow in extension, and forearm in pronation. This position is comfortable and therefore reduces patient motion. It does, however, place the wrist off-isocenter of the magnet, which decreases SNR and makes frequency-selective fat suppression techniques more difficult. The alternative is to position the patient in the "superman position," with the patient prone, the arm above the head and the hand and forearm pronated. While this position has the advantage of placing the wrist closer to the magnet isocenter, it is less comfortable for the patient and increases the chance of patient motion. Elderly patients and patients with shoulder pain or breathing difficulties may be unable to tolerate this position. There is also an increased tendency for the wrist to drift into ulnar deviation in this position, which will affect normal sagittal alignment.

When positioning the patient in the wrist coil, care must be taken to avoid excessive radial or ulnar deviation of the wrist, as this will affect normal sagittal radiolunocapitate alignment. With ulnar deviation of the wrist, a pseudo-DISI (dorsal intercalated segmental instability) configuration may be seen on sagittal images, leading to potential erroneous diagnoses of carpal instability patterns (2). Wrist position and grip will also alter perceived ulnar variance. With the wrist in pronation, ulnar positive variance increases; therefore, care should be taken not to diagnose subtle isolated ulnar variance on MRI without radiographic correlation (3).

3T Imaging of the Wrist

3T imaging may be used for routine MRI of the wrist (4) and some studies have demonstrated improved diagnostic accuracy when imaging the wrist ligaments and the triangular fibrocartilage complex (TFCC) with 3T systems compared to 1.5T systems (5). Increasing the main magnetic field strength (B_0) from 1.5T to 3T doubles the SNR, allowing an increase in image resolution, which can be achieved by decreasing the slice thickness, decreasing the FOV, or increasing the matrix. The doubling of SNR at 3T also allows a decrease in acquisition time, or number of excitations (NEX), which directly reduces scan time.

There are, however, offsets to imaging at 3T. Due to the chemical shift difference between fat and water, imaging at 3T requires the use of a wider receiver bandwidth, which decreases SNR (4). T1 relaxation times are longer and T2 relaxation times are shorter at 3T, requiring alterations in pulse sequence parameters (6). Susceptibility artifact in the presence of metallic hardware or prior surgery is directly proportional to B_0 and therefore can present significant difficulty when imaging at 3T. Specific absorption rate (SAR) is also increased, although this is rarely of clinical importance in routine wrist imaging using standardized sequences (4).

Pulse Sequences and Suggested Protocols

Thin-slice coronal images serve as the mainstay for detecting ligament and cartilage pathology in the wrist. Traditional T1- and T2-weighted techniques are inadequate for the accurate assessment of articular cartilage. Therefore, a cartilage-sensitive sequence such as an intermediate-echo time fast spin echo sequence (FSE) or fat-suppressed 3D gradient echo sequence should be included as part of the standard imaging protocol (Fig. 1).

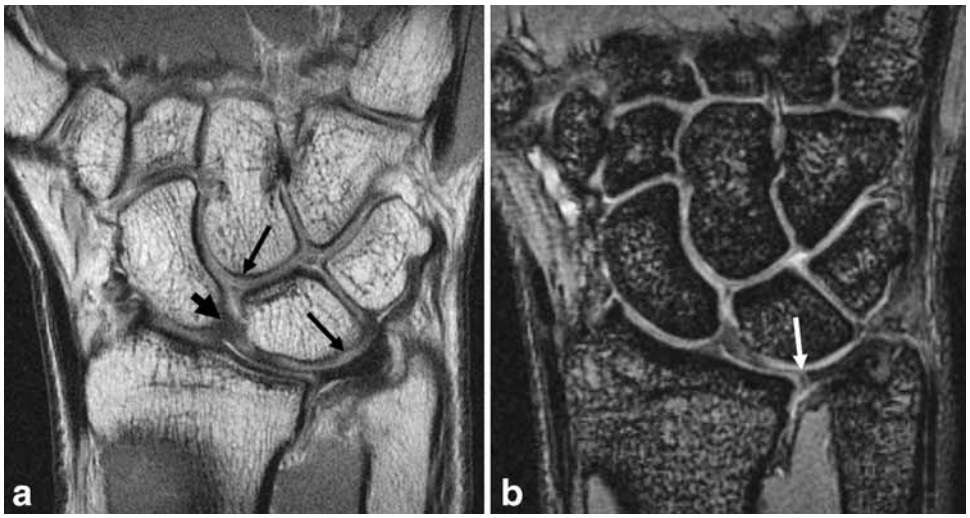

Figure 1. Coronal FSE **(a)** and gradient recalled **(b)** images of the right wrist in a 34-year-old man performed at 1.5T with the sequence parameters outlined in Table 1. With a high resolution technique the cartilage of the wrist is well demonstrated (thin black arrows). The interosseous scapholunate ligament is visualized (thick black arrow), as is the articular disc, which demonstrates a linear fissure through its central margin (white arrow).

Fat-suppressed 3D spoiled or T1-weighted gradient echo images have the advantage of producing thin (0.8–1 mm) contiguous slices (7). This technique, however, requires longer scan times and is limited by metal-induced susceptibility artifact, which may be a problem when imaging the postoperative patient. An intermediate echo time 2D FSE technique provides good contrast between the intermediate signal intensity articular cartilage, the high signal intensity synovial fluid, and the low signal intensity subchondral bone (8). Use of an FSE technique with a wide receiver bandwidth minimizes susceptibility artifact, allowing accurate assessment of articular cartilage in the presence of metallic hardware or debris. 3D-FSE-Cube is an alternative technique that acquires isotropic voxels which can be reformatted in any scan plane (9).

At our institution we therefore perform an intermediate-echo time 2D FSE sequence in three planes, to allow assessment of the articular cartilage and regional tendons. A T2*-weighted 3D coronal gradient recalled sequence is performed, providing thin (1 mm) slice coronal images that allow for detection of intrinsic ligament and articular disc pathology. In addition, a coronal inversion recovery sequence is performed to detect bone marrow edema in the setting of infection, occult fractures, or bone erosions as well as bone viability in the setting of avascular necrosis. An inversion recovery sequence is preferred over a frequency-selective fat-suppression technique, as this results in more uniform fat suppression when imaging off isocenter with the wrist at the patient's side (1).

A suggested protocol for imaging the wrist at 1.5T is provided in Table 1.

Table 1
Sample Protocol for MRI of the Wrist Using a 1.5T System

Timing parameters	Coronal IR	3D coronal GRE	Coronal FSE	Sagittal FSE	Axial FSE
TR (msec)	4,000	40	5,000	5,000	4,000
TE (msec)	17	20	24	24	24
TI (msec)	150	—	—	—	—
Flip angle	—	10	—	—	—
ETL	9	—	7–10	7–10	8–12
RBW (kHz)	31.25	15.63	31.25	31.25	31.25
FOV (cm)	9	8	8	9	8
Matrix	256 x 192	256 x 256	512 x 320	512 x 320	512 x 256–320
Slice thickness (mm)	2.5	1	2.3	2.5–3	3–4
Interslice gap (mm)	0	0	0	0	0
NEX	2	2	2	2	2
Frequency direction	Right to left	Right to left	Right to left	Anterior to posterior	Anterior to posterior

RBW, receiver bandwidth; ETL, echo train length; FOV, field of view; FSE, fast spin echo; GRE, gradient recalled acquisition; IR, inversion recovery; NEX, number of excitations; RBW, receiver bandwidth; TE, echo time; TI, inversion time; TR, repetition time.
The reported RBW is reported as a half bandwidth. To convert to BW per pixel, use the following formula: 2*(half-bandwidth)/(readout matrix). For 3T, the effective TE for FSE sequences is 28–30 msec and the FSE images may be obtained at 1 NEX. Receiver bandwidth for 3T should be ± 62.5 kHz.

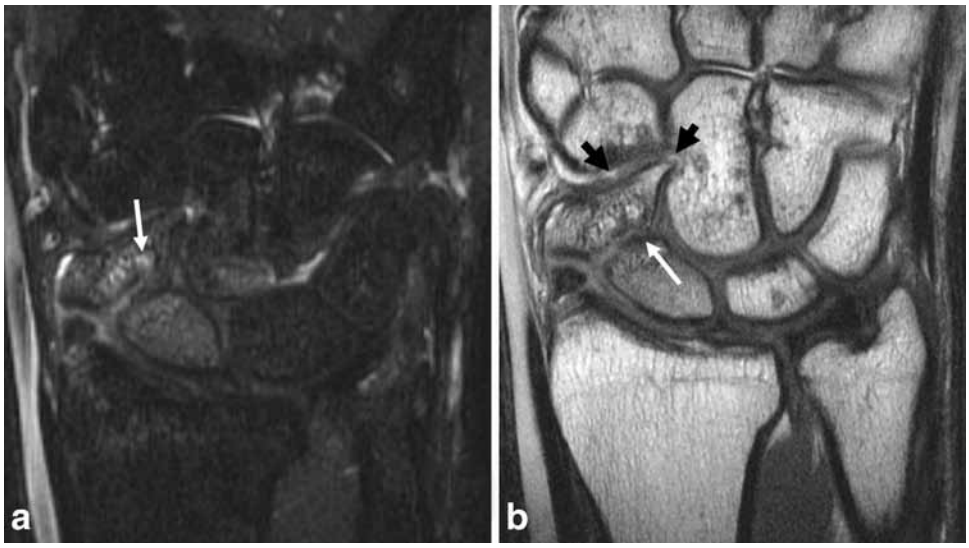

Figure 2. Coronal inversion recovery **(a)** and FSE **(b)** images in a 22-year-old man 2 years status postscaphoid fracture. There is evidence of nonunion with sclerosis and cystic change at the fracture margins (white arrows). A healed fracture is seen through the distal pole of the scaphoid with posttraumatic osteoarthritis of the scaphoid trapezium trapezoid joint (thick black arrow).

OSSEOUS ABNORMALITIES

Injuries to the wrist and hand are common among athletes, accounting for 3%–9% of all athletic injuries (10). MRI has been shown to be useful in the evaluation of wrist trauma with negative radiographs, particularly with regard to the detection of radiographically occult scaphoid fractures (11). MRI can detect avascular necrosis, which may occur as a complication of a scaphoid fracture or in the absence of a history of discrete trauma. MRI is also useful to detect secondary soft tissue and cartilage pathology in the setting of osseous abutment syndromes.

Scaphoid Fractures and Complications

The scaphoid is the most commonly fractured carpal bone; injuries to the scaphoid account for 60%–70% of all carpal bone injuries. Approximately one sixth of scaphoid fractures are radiographically occult at the time of injury (12,13). Traditional management in the presence of a clinically suspected scaphoid fracture with normal radiographs involves treatment with cast immobilization for 2 weeks, followed by repeat clinical examination and delayed radiographs (13). However, follow-up radiography has been shown to have a poor sensitivity, reliability, and negative predictive value (14). Additionally, since the true prevalence of fractures in this group is less than 10% (15), the majority of these patients are overtreated.

It is therefore increasingly common for MRI to be the next investigation in the work-up of patients with a clinically suspected scaphoid fracture and normal radiographs. MRI is highly accurate for confirming or excluding the diagnosis of scaphoid fracture (11) and has a 100% negative predictive value in the immature skeleton (16). MRI has been shown to be a cost-effective method for ruling out occult fractures and bone contusions, thereby avoiding unnecessary immobilization, follow-up appointments, and radiation exposure (17). MRI can detect additional soft tissue injuries and can diagnose injury to the intrinsic or extrinsic ligaments of the wrist, which can mimic a scaphoid fracture on clinical examination (18).

On MRI, an acute fracture is seen as a low signal intensity line extending across the bone with an adjacent marrow edema pattern. High spatial resolution will help to identify more subtle fracture lines. A bone contusion, which is sometimes referred to as a "bone bruise," represents an injury to the trabeculae without evidence of a discrete fracture (19). On MRI, a bone contusion manifests as a bone marrow edema pattern, without a discernable fracture line.

In the presence of an established scaphoid fracture, MRI is well suited to diagnosing complications such as nonunion and avascular necrosis (AVN). Approximately 12% of scaphoid fractures fail to heal and progress to nonunion, requiring internal fixation and bone grafting (16). The criterion for bony union on MRI is the presence of normal signal intensity marrow crossing the previous fracture line. The presence of a persistent fracture line with sclerosis at the fracture margins should raise the possibility of nonunion. Cystic change at the fracture margins is also suspicious for micro-motion in the setting of nonunion (16) (Fig. 2).

Nonunion of the scaphoid may progress to AVN, which has been reported to occur in 13%–50% of scaphoid fractures (20). The proximal pole of the scaphoid is prone to AVN due to the distal location of the main nutrient vessels and the retrograde pattern of the intraosseous blood supply (21). Fractures of the middle third of the scaphoid are associated with a 30% incidence of AVN, while fractures of the proximal fifth have a nearly 100% associated incidence of AVN (22). Viability of fracture fragments is a prerequisite for fracture union; therefore, the assessment of proximal pole vascularity is important to determine management in the setting of an established nonunion. In the setting of nonunion with a nonviable fracture fragment, a vascularized bone graft will be placed, rather than a standard nonvascularized bone graft (23).

MRI is the most sensitive noninvasive method to assess vascularity of the scaphoid in the setting of

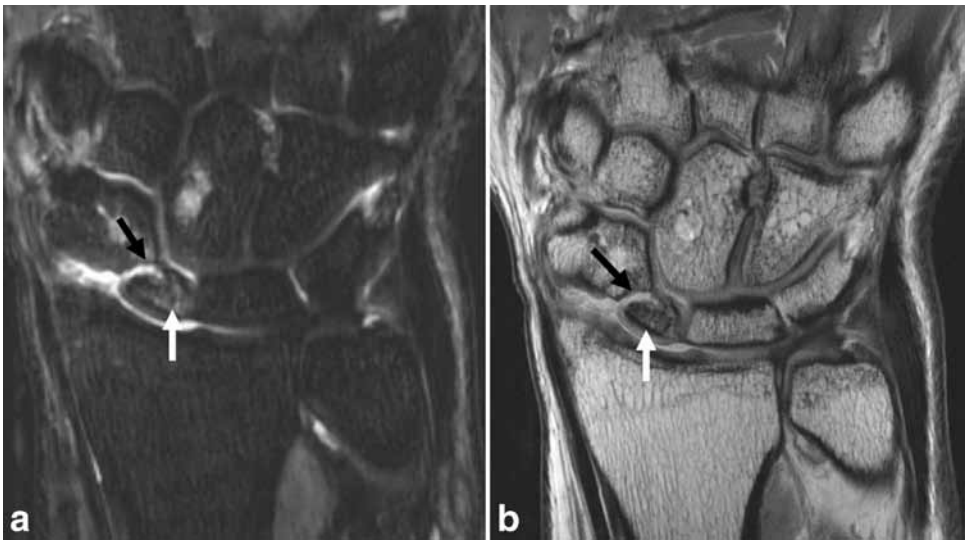

Figure 3. Coronal inversion recovery **(a)** and FSE **(b)** images in a 29-year-old man with an established nonunion of the scaphoid (black arrow). The proximal fragment is low signal intensity on FSE images but demonstrates a bone marrow edema pattern on the inversion recovery image (white arrow), suggesting that the proximal fragment is ischemic but there is no completely devitalized bone.

suspected AVN (Fig. 3). Low signal abnormality in the proximal pole of the scaphoid on T1-weighted sequences alone is nonspecific and may reflect necrosis, ischemia, or viable bone (24,25). However, the presence of low signal intensity on all pulse sequences indicates poor vascularity and is highly predictive of AVN (21,26). Some authors have reported that gadolinium-enhanced MRI is more accurate for the detection of proximal pole AVN (25); however, this result has been disputed by other studies (20,27). We therefore do not routinely perform gadolinium-enhanced imaging when assessing for posttraumatic AVN.

In the presence of metallic hardware, FSE images performed with a high receiver bandwidth, combined with STIR images, allow accurate assessment of proximal pole viability. MRI is also useful to assess for encroachment of cannulated screws on the radioscaphoid or scaphoid trapezium joints, as well as the integrity of the overlying cartilage (Fig. 4). When imaging the postoperative wrist, gradient echo techniques, which lack the 180° refocusing pulse found in FSE sequences, should be avoided. Inversion recovery sequences are preferred over frequency-selective fat suppression, as these sequences are less susceptible to local field inhomogeneities in the presence of metallic hardware. Additional prototype sequence may also be employed to further reduce susceptibility artifact (28).

Carpal Bone Fractures

Other radiographically occult wrist fractures may also be diagnosed on MRI and the utility of MRI in

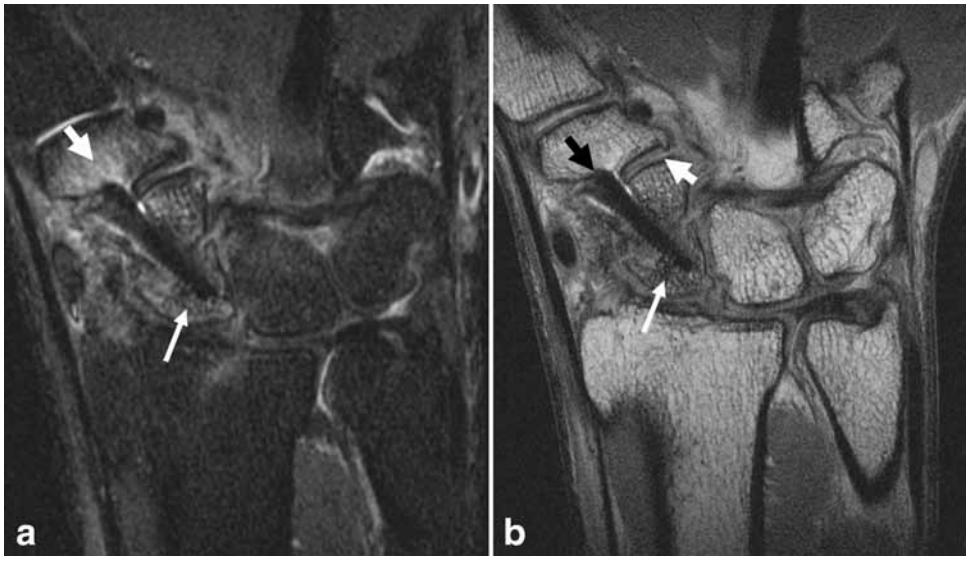

Figure 4. Coronal inversion recovery **(a)** and FSE **(b)** images in a 26-year-old woman 5 months status postinternal fixation of a scaphoid mid-waist fracture. There is ischemia of the proximal fracture fragment, without completely devitalized bone (thin white arrow). The screw penetrates through the distal pole of the scaphoid (thick black arrow), resulting in a bone marrow edema pattern in the trapezium and secondary degenerative arthrosis of the scaphoid trapezium joint (thick white arrows).

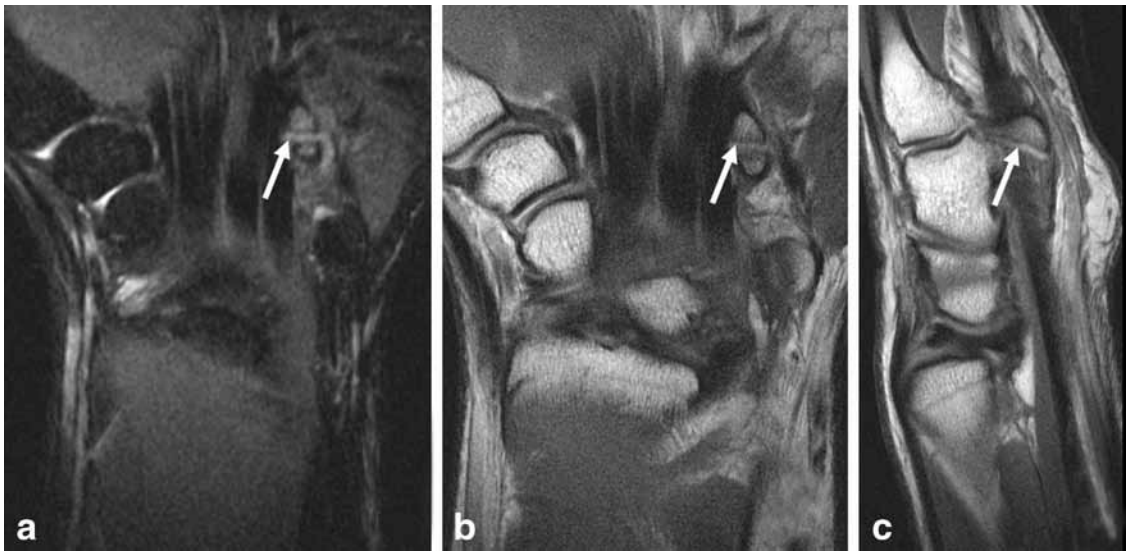

Figure 5. Coronal inversion recovery **(a)** and coronal **(b)** and sagittal **(c)** FSE images in a 20-year-old woman with ongoing pain 1 month status postwrist injury. Previous radiographs were negative. There is a nondisplaced fracture of the hook of the hamate with a mild reactive bone marrow edema pattern (white arrow).

diagnosing occult wrist fractures is well established. Many carpal fractures are difficult to diagnose radiographically, even with the use of specialized views.

Hamate fractures are uncommon, accounting for 1.7% of all carpal fractures, but are usually nondisplaced and difficult to diagnose radiographically. Most hamate fractures involve the hook of the hamate and typically result from baseball impaction, direct impact of the handle of a racket during racket sports (29), or by striking the ground with a golf club (30). Fractures of the body of the hamate are much more uncommon and may be caused by an axial force transmitted through the metacarpals or by a direct blow to the ulnar side of the wrist (29).

The radiographic assessment of the hamate is challenging since routine PA and lateral views of the wrist rarely demonstrate the fracture. Although additional views such as oblique lateral and carpal tunnel views may disclose a fracture and in the setting of negative radiographs, MRI is extremely useful to diagnose an occult fracture (31) (Fig. 5). Hook of hamate fractures can be associated with damage to the adjacent ulnar neurovascular bundle; MRI is able to accurately detect signal abnormality within the ulnar nerve in this setting. MR angiography can be used to detect pseudoaneurysm formation or occlusion in the setting of suspected ulnar artery damage.

Pisiform fractures may result from direct trauma or may be secondary to avulsion, when contraction of the flexor carpi ulnaris tendon occurs in the setting of forcible hyperextension of the wrist (32). Pisiform fractures are commonly associated with other injuries to the carpus or distal radius (33). MRI can detect occult pisiform fractures and assess the overlying cartilage for evidence of chondral shear. Associated bony and soft tissue injuries are also well depicted with MRI.

Stress Fractures and Gymnast's Wrist

Stress fractures, also known as fatigue fractures, occur when repetitive stress is applied to normal bone. Although stress fractures are more commonly seen in the weight-bearing parts of the skeleton, stress fractures have, on occasion, been described in the wrist. Scaphoid stress fractures have been reported in activities that involve repeated wrist dorsiflexion, such as shot putting and gymnastics (34). There have also been case reports of stress fractures involving the hook of the hamate in racket sports (35), the triquetrum in break-dancing (36), and the pisiform in volleyball (37). MRI of a stress reaction manifests as a bone marrow edema pattern with adjacent periosteal and soft tissue edema. If untreated, a stress reaction may progress to a stress fracture, which manifests as a low signal fracture line or cortical breach (30).

Chronic stress across the distal radial growth plate is a particular type of stress injury that has been almost exclusively described in young gymnasts (38). The condition is commonly bilateral. During gymnastics, the upper extremity is used for weight bearing, which results in compressive forces across the distal radial physis. In many cases, rotational forces are also involved, resulting in additional shear stress across the growth plate (39). Distal radial epiphysiolysis or "gymnast's wrist" is therefore thought to represent a Salter Harris 1 type microfracture, due to repetitive compressive forces of the distal radial growth plate (40).

Temporary ischemia across the zone of provisional calcification may result in a "pseudo-rickets" appearance on conventional radiographs, with metaphyseal irregularity and widening of the growth plate. MRI findings in "gymnast's wrist" include widening, increased signal, and irregularity of the distal radial

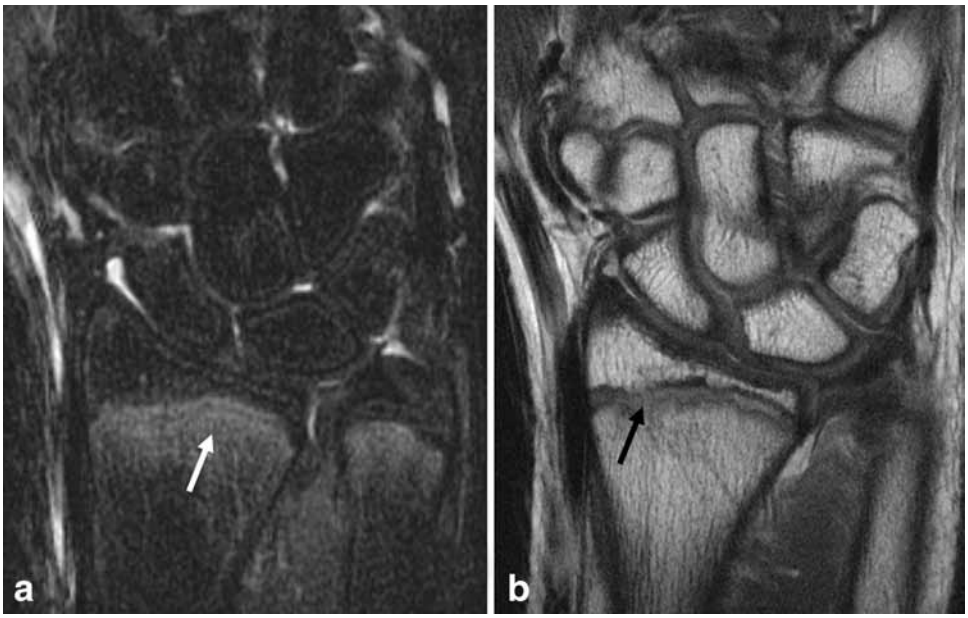

Figure 6. Coronal inversion recovery **(a)** and FSE **(b)** images in an 11-year-old girl demonstrates features of "gymnast's wrist." There is increased signal intensity at the distal radial metaphysis (white arrow) with widening and irregularity of the growth plate (black arrow).

growth plate (Fig. 6). Tongues of physeal cartilage may be seen extending into the metaphysis (39). In the setting of substantial injury to the distal radial physis, premature physeal closure may result, leading to a shortened radius (41).

Avascular Necrosis

Avascular necrosis may occur in the setting of trauma, such as following a scaphoid fracture, or may be idiopathic, in the setting of Kienböck's or Preiser's disease (42).

Kienböck's Disease

Kienböck's disease is a form of osteonecrosis that affects the lunate and is of uncertain etiology. It most commonly occurs in the dominant hand of male manual workers between the ages of 20 and 40 years (43). The condition is usually unilateral. Clinically, patients present with dorsal or ulnar side wrist pain, associated with a decreased range of movement and a decrease in grip strength (44). Although the cause of Kienböck's disease remains unknown, there is an association with negative ulnar variance, which has been observed to occur in 78% of patients with Kienböck's disease, compared with 23% of the normal population (45).

Kienböck's disease can be classified into four stages, which were initially described by Lichtman et al (46). In stage I disease, radiographs are normal but MRI demonstrates focal or diffuse signal abnormality within the lunate. In stage II, the lunate exhibits increased density on radiographs and appears as low signal intensity on T1-weighted images with patchy areas of high signal intensity on fluid-sensitive sequences. In stage III there is collapse of the lunate, allowing proximal migration of the capitate. Stage III may be subclassified into stage IIIA, where there is no carpal collapse and the scaphoid maintains a normal position; and stage IIIB, where there is diminished carpal height and fixed palmar flexion of the scaphoid. Stage IV is characterized by degenerative arthrosis of the radiocarpal joint in the setting of a collapsed necrotic lunate (47,48).

MRI is useful in the early stages of Kienböck's disease when radiographs may be normal. In established Kienböck's disease, MRI is helpful to detect subchondral collapse and the integrity of the cartilage over the proximal and mid carpal rows, which may alter surgical management (Fig. 7).

It is important to note that there are other conditions which may result in a bone marrow edema pattern within the lunate; therefore, increased signal intensity within the lunate should not always be ascribed to Kienböck's disease. Intraosseous ganglion cysts are relatively common in the carpal bones and often occur along ligamentous attachments; they are therefore frequently seen within the lunate adjacent to the attachment of the interosseous scapholunate and lunotriquetral ligaments. The high signal cysts, which may on occasion elicit a surrounding stress reaction, should not be misinterpreted as Kienböck's disease (2). Ulnolunate impaction syndrome may also cause a bone marrow edema pattern in the lunate, which may mimic Kienböck's disease. However, in contrast to Kienböck's disease, where the signal abnormality begins in the proximal radial aspect of the lunate, ulnolunate impaction syndrome will affect the proximal ulnar aspect of the lunate and is associated with positive ulnar variance and abnormalities of the TFCC (2,3).

Preiser's Disease

Preiser's disease refers to osteonecrosis of the scaphoid in the absence of a prior scaphoid fracture (Fig. 8). Preiser's disease was initially thought to be idiopathic. It is now believed to be linked to defective patterns of vascularity of the proximal pole of the

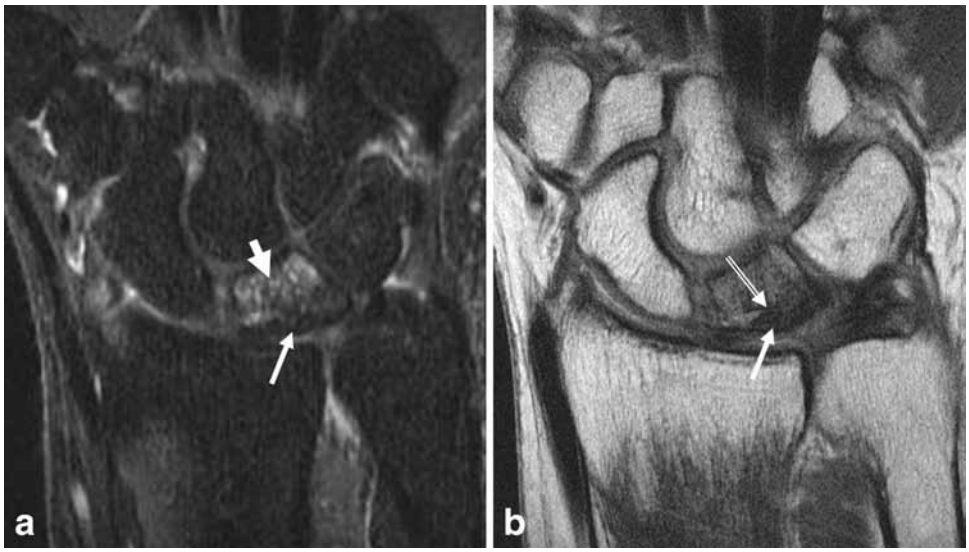

Figure 7. Coronal inversion recovery **(a)** and FSE **(b)** images in a 69-year-old man. There is a bone marrow edema pattern in the lunate due to Kienböck's disease (thick arrow). The proximal ulnar margin of the lunate is hypointense on all pulse sequences (thin arrow) with a subchondral fracture (double arrow), indicative of completely devitalized bone.

scaphoid and can be seen in association with repetitive microtrauma or as a complication of drug therapy (16).

MRI is the modality of choice to diagnose Preiser's disease. Two distinct patterns of Preiser's disease have been described on MRI (49). Type 1 disease is characterized by signal abnormality that affects the entire scaphoid. These patients have a propensity for progression towards degenerative arthrosis. Type II disease is characterized by signal abnormality in 50% or less of the scaphoid, and are associated with a better prognosis.

Impaction/Impingement Syndromes

A number of impaction and impingement syndromes have been described. Although these conditions are usually diagnosed with clinical assessment and plain radiographs, MRI is helpful to confirm the diagnosis as well as assess for associated chondral wear, bone marrow edema, and associated soft tissue injuries (50).

Ulnolunate Abutment Syndrome

Ulnolunate abutment syndrome, also known as ulnar impaction syndrome, is a degenerative condition of the ulnar side of the wrist which occurs in the setting of positive ulnar variance. Positive ulnar variance may be congenital or due to malunion of a distal radial fracture or prior radial head resection. The result is that excessive load is imparted to the ulnar carpus, TFCC, and ulnar head. Patients present with ulnar-sided wrist pain which is exacerbated by maneuvers that increase ulnar variance, such as forearm pronation, ulnar deviation, and power grip (51).

Impaction between the distal ulna and ulnar carpus leads to a continuum of pathologic changes, usually commencing with a degenerative tear of the TFCC, followed by cartilage wear over the lunate, triquetrum, and distal ulna. Degenerative tears of the

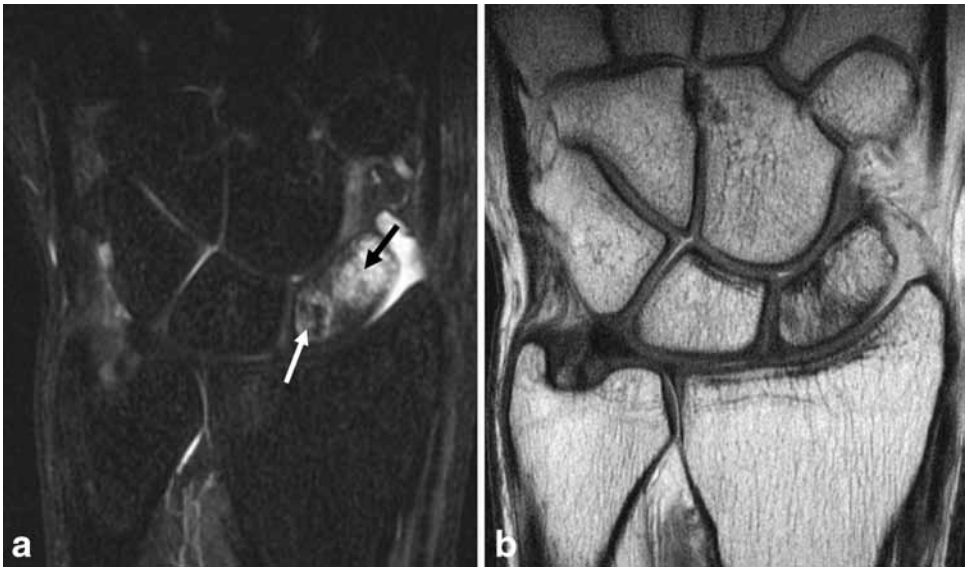

Figure 8. Coronal inversion recovery **(a)** and FSE **(b)** images in a 39-year-old man demonstrate an intense bone marrow edema pattern in the scaphoid (black arrow) with evidence of avascular necrosis of the proximal pole (white arrow). No fracture is visible and the patient denied a history of discrete trauma. The findings are indicative of Preiser's disease.

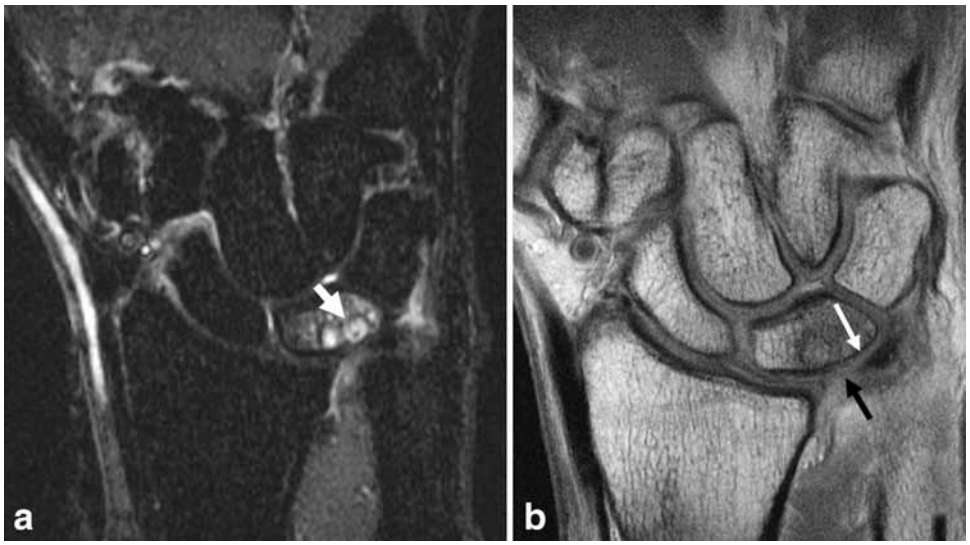

Figure 9. Coronal inversion recovery **(a)** and FSE **(b)** images in a 56-year-old woman demonstrate a bone marrow edema pattern in the lunate with subchondral cyst formation at the ulnar proximal margin (thick white arrow). There is a degenerative central defect of the articular disc (black arrow). Hyperintense cartilage is seen over the proximal ulnar margin of the lunate (thin white arrow). Radiographs confirmed positive ulnar variance. The features are indicative of ulnolunate abutment syndrome.

interosseous lunotriquetral ligament may occur. Finally, degenerative arthrosis of the ulnocarpal and distal radioulnar joints may result (52).

MRI demonstrates increased signal intensity in the distal ulna and the ulnar aspect of the lunate (53). Subchondral cyst formation and sclerosis may occur. MRI allows assessment of the TFCC for tears, as well as the integrity of the overlying cartilage of the lunate, triquetrum, and distal ulna (54) (Fig. 9). The choice of treatment for ulnolunate impaction will depend on the cause of abutment and the integrity of the cartilage over the proximal carpal row and distal radioulnar joint; therefore, these chondral surfaces should be closely scrutinized on MR images.

Ulnar Styloid Impingement

Ulnar styloid impingement is due to an excessively long ulnar styloid process or a nonunited styloid process fracture, which impacts on the triquetrum (55). This may result in cartilage wear over the proximal triquetrum and can lead to eventual lunotriquetral joint instability.

Radiographs may demonstrate an excessively long ulnar styloid (greater than 6 mm), a curved ulnar styloid, or a nonunited styloid process fracture. MRI is useful to demonstrate secondary changes of ulnar styloid impingement, such as cartilage defects over the proximal triquetrum as well as bone marrow edema, subchondral cysts, and sclerosis in the triquetrum or ulnar styloid (50) (Fig. 10). Treatment for styloid impingement involves resection of all but the proximal 2 mm of the ulnar styloid, thus preserving the integrity of the TFCC attachments (55).

Ulnar Impingement Syndrome

Ulnar impingement syndrome occurs in association with negative ulnar variance, which may be congenital or due to previous trauma or surgery (56). The shortened ulnar impinges on the distal radius and can result in a painful pseudarthrosis with the distal radius. Patients present with ulnar-sided wrist pain, which is exaggerated by forearm pronation and supination.

Radiographs demonstrate a shortened ulna, which articulates proximal to the sigmoid notch of the radius, and may demonstrate scalloping, sclerosis, and hypertrophy at the site of impingement (54,56). MRI is useful in the setting of suspected ulnar impingement syndrome to demonstrate associated bone marrow edema, subchondral marrow changes, and early sclerosis.

Hamatolunate Impaction

The presence of a hamate-lunate facet, also known as a type II lunate, is an anatomic variant with a reported incidence of 44%–77% (57). While the majority of the patients are asymptomatic, the presence of the additional facet is thought to predispose to impingement of the hamate by the lunate when the wrist is in ulnar deviation (58). A type II lunate is associated with a higher prevalence of cartilage wear over the proximal pole of the hamate (59,60). In one study, arthrosis of the proximal pole of the hamate was reported in 38% of cadavers with a type II lunate, compared with 1.8% of those with a type I lunate (59).

A type II lunate is usually diagnosed on conventional radiographs. MRI is useful in this setting to demonstrate secondary cartilage wear over the proximal pole of the hamate as well as subchondral sclerosis and associated bone marrow edema.

CARTILAGE IMAGING

The hyaline cartilage of the radiocarpal and intercarpal joints is relatively thin, proving a challenge for

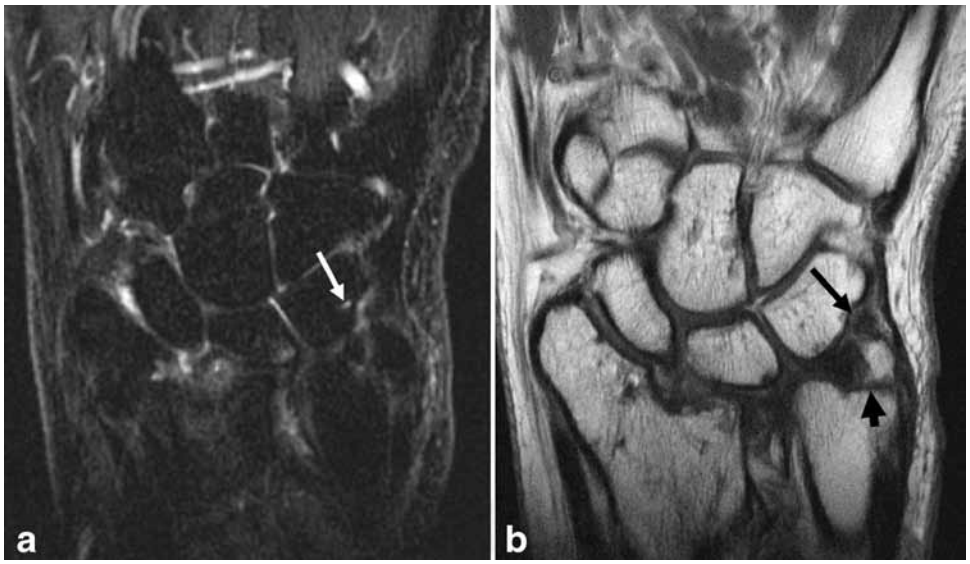

Figure 10. Coronal inversion recovery **(a)** and FSE **(b)** images in a 61-year-old woman with a history of remote distal radial fracture. There is an un-united fracture of the ulnar styloid (thick black arrow) with hypertrophy of the fracture fragment. There is scarring in the prestyloid recess with partial thickness cartilage wear over the proximal triquetrum (black arrow) and early subchondral cystic change (thin white arrow), indicative of ulnar styloid impingement.

visualization on MRI (61). Although accurate assessment of the articular cartilage of the wrist is difficult, it is important for decision making in reconstructive wrist surgery. There are a large number of wrist salvage procedures available and the integrity of regional cartilage is crucial to decide between limited procedures and total wrist arthrodesis (62).

There is controversy in the literature surrounding the diagnostic accuracy of MRI for the assessment of wrist cartilage (5,59,63–65). Haime et al (64) reported sensitivities of 18%–41% in the detection of focal cartilage lesions in the proximal carpal row, with specificities of 75%–93%. In contrast, Bordalo-Rodrigues et al (63) reported 1.5T MRI to be accurate for the detection of lunate chondromalacia, as correlated with subsequent arthroscopy.

There is also uncertainty about whether imaging at 3T increases the diagnostic capability of cartilage assessment. In a cadaveric study, Saupe et al (5) compared sensitivities for cartilage lesions on 1.5T versus 3T using an intermediate-weighted FSE sequence and 3D GRE sequence. They reported sensitivities and specificities of 43%–52% and 82%–89% at 1.5T, compared to 49%–52% and 82% at 3T. Highest sensitivities were observed in the proximal carpal row (67%–71%) and lower sensitivities were observed in the distal carpal row (14%–24%). The differences did not reach statistical significance; however, it is important to note that a dedicated wrist coil was not used for 3T imaging in this study (5).

In our experience, when MRI is performed with the use of thin contiguous slices and a high-resolution matrix, cartilage lesions of the wrist are well demonstrated and correlate well with the results of surgical inspection. Future directions toward imaging of wrist cartilage will involve techniques such as T2 mapping and T1-rho, which allow detection of alterations in collagen orientation (66) and proteolgycan content (67,68), respectively. Although not commonly performed in clinical practice, these quantitative techniques have been shown to be feasible in the wrist and can be performed in clinically acceptable scan times (69).

SLAC/SNAC Wrist

Scapholunate advanced collapse (SLAC) and scaphoid nonunion advanced collapse (SNAC) are degenerative conditions of the wrist which result from abnormal carpal alignment. In SLAC wrist, abnormal alignment occurs due to a tear of the interosseous scapholunate ligament, which results in dorsal intercalated segment instability (DISI) with dorsiflexion of the lunate (70). In SNAC wrist, abnormal alignment is a result of a scaphoid fracture complicated by nonunion. Degenerative changes occur at the capitolunate joint and progress to involve the radioscaphoid joint.

MRI can evaluate intrinsic ligament disruption, as well as the integrity of regional cartilage in the setting of chronic scapholunate ligament insufficiency. In the setting of an SLAC/SNAC wrist MRI is useful to evaluate the cartilage over the radioscaphoid, radiolunate, and capitolunate joints (Figs. 11, 12).

Surgical options for SLAC wrist include proximal row carpectomy, four corner fusion, and total wrist arthrodesis. Determining the integrity of regional cartilage is of crucial importance to the surgeon when deciding between these procedures. For example, in patients with stage 2 SLAC wrist the cartilage over the proximal pole of the capitate and lunate fossa of the radius remain intact. This allows direct painless articulation of the capitate and radius after excision of the scaphoid, lunate, and triquetrum, also known as a "proximal row carpectomy." In stage 3 SLAC wrist, however, there is cartilage loss over the proximal pole of the capitate and midcarpal joints, eliminating this surgical option. Surgical management in the setting of

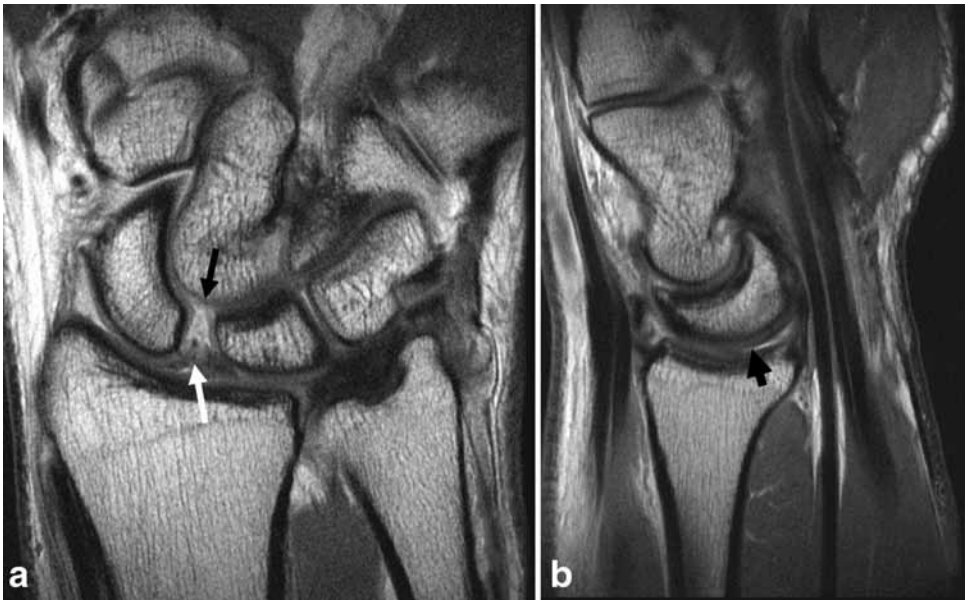

Figure 11. Coronal **(a)** and sagittal **(b)** FSE images in a 46-year-old man demonstrate disruption of the interosseous scapholunate ligament (white arrow) with widening of the scapholunate interval and dorsal tilt of the lunate (thick black arrow). There is partial thickness cartilage wear over the proximal pole of the capitate (thin black arrow), indicative of an early SLAC wrist. The cartilage over the radioscaphoid and radiolunate joints is preserved.

stage 3 SLAC wrist will usually require excision of the degenerative midcarpal joint and surgical fusion of the lunate, triquetrum, capitate, and hamate, also known as a "four corner fusion" (71).

Osteoarthritis

In contrast to the fingers, primary osteoarthritis of the wrist is uncommon. Radiocarpal osteoarthritis usually occurs secondary to prior ligament injury (SLAC wrist), fracture (SNAC wrist), or avascular necrosis and accounts for 55% of cases of degenerative arthrosis of the wrist (72).

Trapezio-metacarpal (basilar joint of the thumb) arthritis is relatively common, affecting 8% of the population over 55 years of age. It is almost always bilateral and most commonly occurs in perimenopausal women (72). Osteoarthritis of the scaphoid-trapezium trapezoid (STT) joint accounts for 20% of cases of wrist arthrosis and is most commonly associated with basilar joint arthritis (Fig. 13). Isolated severe STT joint osteoarthritis is unusual and is highly suggestive of a crystal-related arthropathy such as calcium pyrophosphate deposition (CPPD) disease. The pisotriquetral joint is another relatively common site of osteoarthritis of the wrist and is often overlooked on imaging studies. The pisiform-triquetral joint is well visualized on

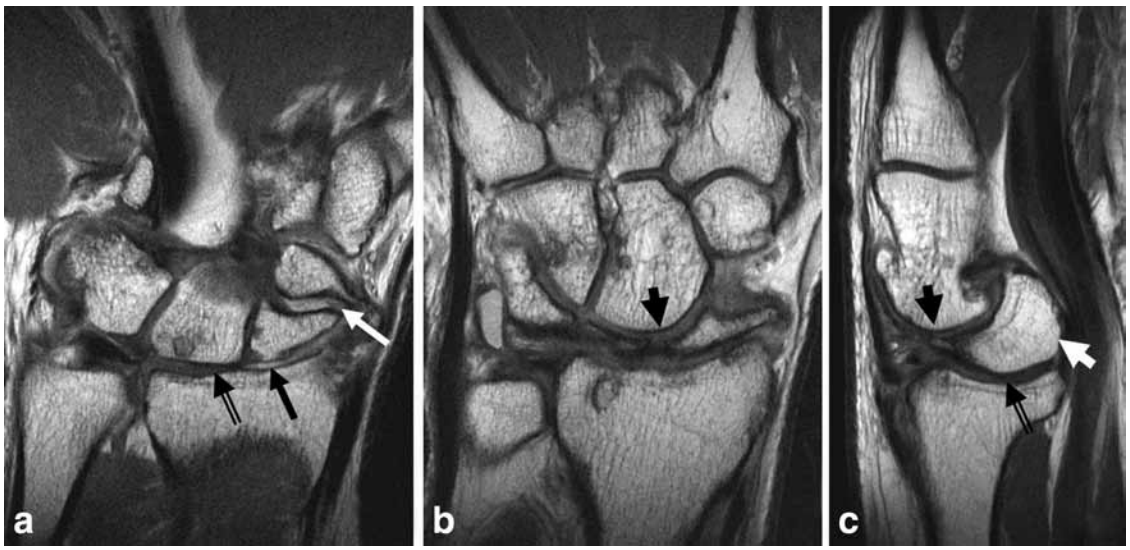

Figure 12. Coronal **(a,b)** and sagittal **(c)** FSE images in a 31-year-old man demonstrate features of an SNAC wrist. There is nonunion of a scaphoid waist fracture with a pseudarthrosis at the fracture site (thin white arrow). There is dorsal tilt of the lunate (thick white arrow) and proximal migration of the capitate (thick black arrow). Full thickness cartilage wear is seen over the radioscaphoid joint (thin black arrow) with partial thickness cartilage wear over the radiolunate joint (double black arrow).

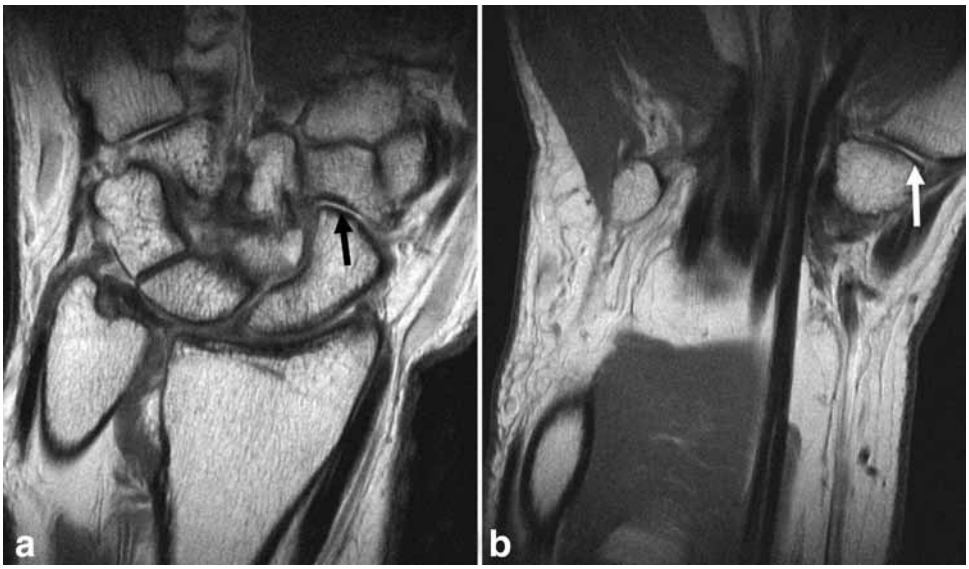

Figure 13. Coronal **(a)** and sagittal **(b)** FSE images in a 55-year-old man demonstrate osteoarthritis of the scaphoid trapezium trapezoid joint with full thickness cartilage loss and subchondral sclerosis (black arrow). There is osteoarthritis of the basilar joint of the thumb with exposed bone (white arrow).

sagittal and axial MR images and should be carefully scrutinized in all patients with ulnar-sided wrist pain (50).

Inflammatory Arthropathies

Rheumatoid Arthritis

Rheumatoid arthritis is a common disease that affects up to 1% of the population. It is characterized by an inflammatory synovitis which progresses to articular cartilage loss, bony erosions, and joint destruction. Synovitis begins as early as 2 years after disease onset (73,74); however, most patients in the early stages of the disease present with normal radiographic findings.

The availability of disease-modifying antirheumatic drugs (DMARDs) and biologic agents has led to the need to accurately identify patients with early inflammatory arthritis who are at high risk of erosive disease so that they can be treated aggressively. MRI is the most sensitive means of identifying rheumatoid arthritis at its earliest stages (75,76).

Marrow edema is a common finding in rheumatoid arthritis, affecting 64% of patients in the early stage of the disease (77). Bone marrow edema has been shown to be predictive of a future site of erosion and is associated with a 6-fold increased risk of erosion within 1 year. Bone marrow edema is the strongest independent reversible MRI precursor of erosions (78).

In later stages of rheumatoid arthritis, MRI can identify bony erosions, synovitis, and tenosynovitis (Fig. 14). These findings are common on MRI, despite the presence of normal radiographs. Erosions most commonly occur in the triquetrum, capitate, scaphoid, and radial aspects of the second and third MCP joints (79). Synovitis may progress to bulky

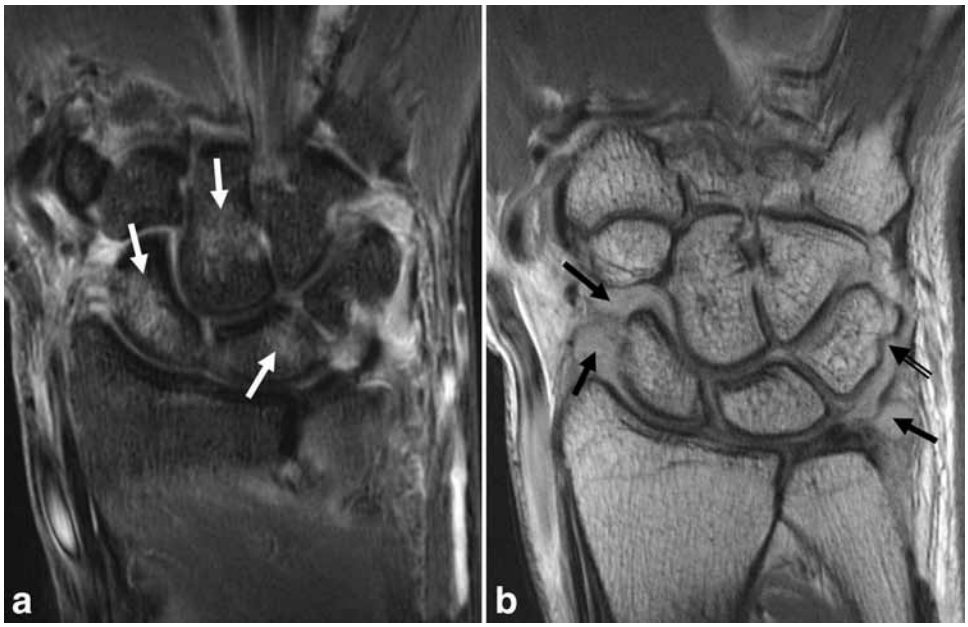

Figure 14. Coronal inversion recovery **(a)** and FSE **(b)** images in a 45-year-old woman demonstrate a pancarpal inflammatory synovitis (black arrows) with a patchy bone marrow edema pattern in multiple carpal bones (white arrows) and an erosion over the ulnar margin of the triquetrum (double black arrows). The findings are indicative of an inflammatory arthropathy. The corresponding radiographs showed no abnormality.

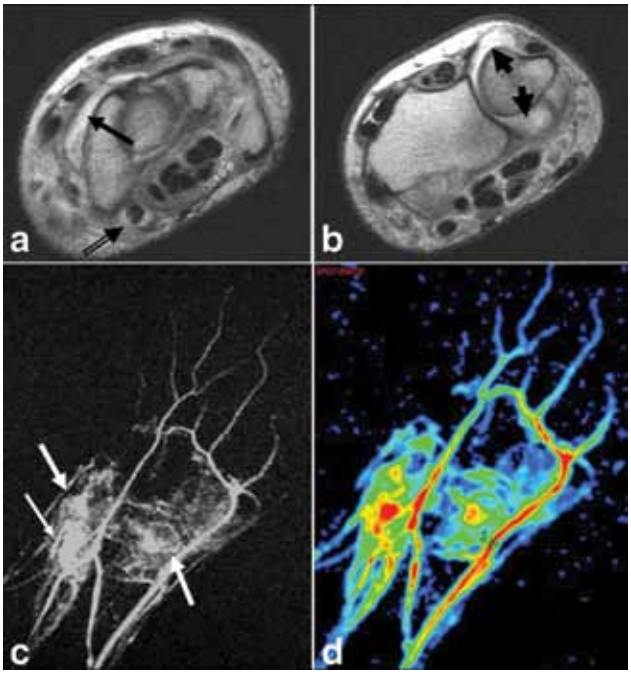

Figure 15. Axial **(a,b)** FSE images in a 54 year-old woman with rheumatoid arthritis demonstrate an inflammatory synovitis of the radiocarpal (black arrow) and distal radioulnar joint (thick black arrow). There is a tenosynovitis of the flexor carpi radialis (double black arrow). Corresponding MR angiography **(c,d)** demonstrates neovascularization at the level of the midcarpal (thick white arrows) and distal radioulnar (thin white arrow) joints.

pannus formation, which can result in ligament disruption and nerve compression. These complications are well depicted on MRI.

The use of gadolinium-enhanced MRI may help to differentiate between an effusion and inflamed synovium or pannus (80). Synovial enhancement occurs rapidly (between 1–2 minutes) following intravenous gadolinium administration. After 15–20 minutes, gadolinium infuses into the synovial fluid and equilibrium occurs (81). Therefore, if intravenous gadolinium is administered, imaging within the first few minutes following injection will result in the highest level of differentiation between inflamed synovium versus effusion (82).

The use of MR angiography has also been proposed as a noninvasive biomarker to identify abnormal vasculature in patients with early inflammatory arthritis (83). Synovial angiogenesis is one of the earliest markers of inflammatory arthritis (84). MR angiography can provide direct visualization of pathologic synovial neovascularization and the number of vessels on MR angiography shows a strong correlation with synovitis, bone marrow edema, and bone erosions (83) (Fig. 15). Dynamic MR angiography is performed with a fast-repeated series of 3D spoiled gradient-echo images. Repeated sequences of about 20 seconds each are obtained over the first 4 minutes following gadolinium injection, using a thin slice coronal 3D T1 fat-saturated technique. While currently useful as a research tool, dynamic contrast-enhanced MRI is seldom performed in clinical practice due to the additional time to acquire images and additional postprocessing that is required (85).

Other Arthropathies

A wide number of other arthropathies may present in the wrist, including seronegative spondyloarthropathies, amyloid arthropathy, gout, pigmented villonodular synovitis, and septic arthritis.

The seronegative spondyloarthropathies include ankylosing spondylitis, psoriatic arthritis, reactive arthritis, and enteropathic arthritis. These are differentiated from rheumatoid arthritis by their predilection to involve the axial skeleton as well as the presence of enthesopathies. However, due to the overlap in imaging findings, spondyloarthropathies cannot be clearly differentiated from rheumatoid arthritis on MRI of the wrist alone (86).

CONCLUSION

High-resolution noncontrast MRI allows reproducible, accurate assessment of the cartilage and osseous structures of the wrist. MRI is useful to diagnose occult fractures in the setting of negative radiographs and assess for complications such as nonunion and avascular necrosis following scaphoid fracture. MRI is useful to diagnose common impingement syndromes and to assess for cartilage wear in the setting of a SLAC/SNAC wrist, which will directly alter surgical management. MRI can detect early inflammatory arthritis, identifying patients who may benefit from aggressive treatment to prevent the development of future erosive disease.

DISCLOSURES/CONFLICT OF INTEREST

The Hospital for Special Surgery receives research support from General Electric Healthcare.

REFERENCES

1. Sofka CM, Potter HG. Magnetic resonance imaging of the wrist. Semin Musculoskelet Radiol 2001;5:217–226.
2. Zanetti M, Saupe N, Nagy L. Role of MR imaging in chronic wrist pain. Eur Radiol 2007;17:927–938.
3. Malone WJ, Snowden R, Alvi F, Klena JC. Pitfalls of wrist MR imaging. Magn Reson Imaging Clin N Am 2010;18:643–662.
4. Saupe N. 3-Tesla high-resolution MR imaging of the wrist. Semin Musculoskelet Radiol 2009;13:29–38.
5. Saupe N, Prussmann KP, Luechinger R, Bosiger P, Marincek B, Weishaupt D. MR imaging of the wrist: comparison between 1.5- and 3-T MR imaging—preliminary experience. Radiology 2005; 234:256–264.
6. Cunningham PM, Law M, Schweitzer ME. High-field MRI. Orthop Clin North Am 2006;37:321–329.
7. Eckstein F, Schnier M, Haubner M, et al. Accuracy of cartilage volume and thickness measurements with magnetic resonance imaging. Clin Orthop Relat Res 1998:137–148.
8. Potter HG, Linklater JM, Allen AA, Hannafin JA, Haas SB. Magnetic resonance imaging of articular cartilage in the knee. An evaluation with use of fast-spin-echo imaging. J Bone Joint Surg Am 1998;80:1276–1284.
9. Stevens KJ, Wallace CG, Chen W, Rosenberg JK, Gold GE. Imaging of the wrist at 1.5 Tesla using isotropic three-dimensional fast spin echo cube. J Magn Reson Imaging 2011;33:908–915.

10. Rettig AC. Athletic injuries of the wrist and hand. Part I: Traumatic injuries of the wrist. Am J Sports Med 2003;31:1038–1048.
11. Yin ZG, Zhang JB, Kan SL, Wang XG. Diagnosing suspected scaphoid fractures: a systematic review and meta-analysis. Clin Orthop Relat Res 2010;468:723–734.
12. Hunter JC, Escobedo EM, Wilson AJ, Hanel DP, Zink-Brody GC, Mann FA. MR imaging of clinically suspected scaphoid fractures. AJR Am J Roentgenol 1997;168:1287–1293.
13. Steinmann SP, Adams JE. Scaphoid fractures and nonunions: diagnosis and treatment. J Orthop Sci 2006;11:424–431.
14. Low G, Raby N. Can follow-up radiography for acute scaphoid fracture still be considered a valid investigation? Clin Radiol 2005;60:1106–1110.
15. Adey L, Souer JS, Lozano-Calderon S, Palmer W, Lee SG, Ring D. Computed tomography of suspected scaphoid fractures. J Hand Surg Am 2007;32:61–66.
16. Karantanas A, Dailiana Z, Malizos K. The role of MR imaging in scaphoid disorders. Eur Radiol 2007;17:2860–2871.
17. Dorsay TA, Major NM, Helms CA. Cost-effectiveness of immediate MR imaging versus traditional follow-up for revealing radiographically occult scaphoid fractures. AJR Am J Roentgenol 2001;177:1257–1263.
18. Fowler C, Sullivan B, Williams LA, McCarthy G, Savage R, Palmer A. A comparison of bone scintigraphy and MRI in the early diagnosis of the occult scaphoid waist fracture. Skeletal Radiol 1998;27:683–687.
19. Rangger C, Kathrein A, Freund MC, Klestil T, Kreczy A. Bone bruise of the knee: histology and cryosections in 5 cases. Acta Orthop Scand 1998;69:291–294.
20. Donati OF, Zanetti M, Nagy L, Bode B, Schweizer A, Pfirrmann CW. Is dynamic gadolinium enhancement needed in MR imaging for the preoperative assessment of scaphoidal viability in patients with scaphoid nonunion? Radiology 2011;260:808–816.
21. Trumble TE. Avascular necrosis after scaphoid fracture: a correlation of magnetic resonance imaging and histology. J Hand Surg Am 1990;15:557–564.
22. Inoue G, Sakuma M. The natural history of scaphoid non-union. Radiographical and clinical analysis in 102 cases. Arch Orthop Trauma Surg 1996;115:1–4.
23. Kawamura K, Chung KC. Treatment of scaphoid fractures and nonunions. J Hand Surg Am 2008;33:988–997.
24. Desser TS, McCarthy S, Trumble T. Scaphoid fractures and Kienbock's disease of the lunate: MR imaging with histopathologic correlation. Magn Reson Imaging 1990;8:357–361.
25. Cerezal L, Abascal F, Canga A, Garcia-Valtuille R, Bustamante M, del Pinal F. Usefulness of gadolinium-enhanced MR imaging in the evaluation of the vascularity of scaphoid nonunions. AJR Am J Roentgenol 2000;174:141–149.
26. Perlik PC, Guilford WB. Magnetic resonance imaging to assess vascularity of scaphoid nonunions. J Hand Surg Am 1991;16:479–484.
27. Singh AK, Davis TR, Dawson JS, Oni JA, Downing ND. Gadolinium enhanced MR assessment of proximal fragment vascularity in nonunions after scaphoid fracture: does it predict the outcome of reconstructive surgery? J Hand Surg Br 2004;29:444–448.
28. Hargreaves BA, Worters PW, Pauly KB, Pauly JM, Koch KM, Gold GE. Metal-induced artifacts in MRI. AJR Am J Roentgenol 2011;197:547–555.
29. Papp S. Carpal bone fractures. Orthop Clin North Am 2007;38:251–260, vii.
30. Lisle DA, Shepherd GJ, Cowderoy GA, O'Connell PT. MR imaging of traumatic and overuse injuries of the wrist and hand in athletes. Magn Reson Imaging Clin N Am 2009;17:639–654.
31. Watanabe A, Souza F, Vezeridis PS, Blazar P, Yoshioka H. Ulnar-sided wrist pain. II. Clinical imaging and treatment. Skeletal Radiol 2010;39:837–857.
32. Fleege MA, Jebson PJ, Renfrew DL, Steyers CM Jr, el-Khoury GY. Pisiform fractures. Skeletal Radiol 1991;20:169–172.
33. Kaewlai R, Avery LL, Asrani AV, Abujudeh HH, Sacknoff R, Novelline RA. Multidetector CT of carpal injuries: anatomy, fractures, and fracture-dislocations. Radiographics 2008;28:1771–1784.
34. Hanks GA, Kalenak A, Bowman LS, Sebastianelli WJ. Stress fractures of the carpal scaphoid. A report of four cases. J Bone Joint Surg Am 1989;71:938–941.
35. Guha AR, Marynissen H. Stress fracture of the hook of the hamate. Br J Sports Med 2002;36:224–225.
36. Lohman M, Kivisaari L, Partio EK. Stress reaction in the carpal bones caused by breakdancing. Emerg Radiol 2003;10:102–104.
37. Blum AG, Zabel JP, Kohlmann R, et al. Pathologic conditions of the hypothenar eminence: evaluation with multidetector CT and MR imaging. Radiographics 2006;26:1021–1044.
38. Carter SR, Aldridge MJ. Stress injury of the distal radial growth plate. J Bone Joint Surg Br 1988;70:834–836.
39. Anderson MW. Imaging of upper extremity stress fractures in the athlete. Clin Sports Med 2006;25:489–504.
40. Carter SR, Aldridge MJ, Fitzgerald R, Davies AM. Stress changes of the wrist in adolescent gymnasts. Br J Radiol 1988;61:109–112.
41. Davis KW. Imaging pediatric sports injuries: upper extremity. Radiol Clin North Am 2010;48:1199–1211.
42. Botte MJ, Pacelli LL, Gelberman RH. Vascularity and osteonecrosis of the wrist. Orthop Clin North Am 2004;35:405–421, xi.
43. Schuind F, Eslami S, Ledoux P. Kienbock's disease. J Bone Joint Surg Br 2008;90:133–139.
44. Hooper G. Kienbock's disease. J Hand Surg Br 1992;17:3–4.
45. Gelberman RH, Salamon PB, Jurist JM, Posch JL. Ulnar variance in Kienbock's disease. J Bone Joint Surg Am 1975;57:674–676.
46. Lichtman DM, Alexander AH, Mack GR, Gunther SF. Kienbock's disease-update on silicone replacement arthroplasty. J Hand Surg Am 1982;7:343–347.
47. Hashizume H, Asahara H, Nishida K, Inoue H, Konishiike T. Histopathology of Kienbock's disease. Correlation with magnetic resonance and other imaging techniques. J Hand Surg Br 1996;21:89–93.
48. Imaeda T, Nakamura R, Miura T, Makino N. Magnetic resonance imaging in Kienbock's disease. J Hand Surg Br 1992;17:12–19.
49. Kalainov DM, Cohen MS, Hendrix RW, Sweet S, Culp RW, Osterman AL. Preiser's disease: identification of two patterns. J Hand Surg Am 2003;28:767–778.
50. Coggins CA. Imaging of ulnar-sided wrist pain. Clin Sports Med 2006;25:505–526.
51. Friedman SL, Palmer AK. The ulnar impaction syndrome. Hand Clin 1991;7:295–310.
52. Palmer AK. Triangular fibrocartilage complex lesions: a classification. J Hand Surg Am 1989;14:594–606.
53. Escobedo EM, Bergman AG, Hunter JC. MR imaging of ulnar impaction. Skeletal Radiol 1995;24:85–90.
54. Cerezal L, del Pinal F, Abascal F, Garcia-Valtuille R, Pereda T, Canga A. Imaging findings in ulnar-sided wrist impaction syndromes. Radiographics 2002;22:105–121.
55. Topper SM, Wood MB, Ruby LK. Ulnar styloid impaction syndrome. J Hand Surg Am 1997;22:699–704.
56. Bell MJ, Hill RJ, McMurtry RY. Ulnar impingement syndrome. J Bone Joint Surg Br 1985;67:126–129.
57. Viegas SF, Patterson RM, Hokanson JA, Davis J. Wrist anatomy: incidence, distribution, and correlation of anatomic variations, tears, and arthrosis. J Hand Surg Am 1993;18:463–475.
58. Thurston AJ, Stanley JK. Hamato-lunate impingement: an uncommon cause of ulnar-sided wrist pain. Arthroscopy 2000;16:540–544.
59. Pfirrmann CW, Theumann NH, Chung CB, Trudell DJ, Resnick D. The hamatolunate facet: characterization and association with cartilage lesions-magnetic resonance arthrography and anatomic correlation in cadaveric wrists. Skeletal Radiol 2002;31:451–456.
60. Viegas SF, Wagner K, Patterson R, Peterson P. Medial (hamate) facet of the lunate. J Hand Surg Am 1990;15:564–571.
61. Peterfy CG, van Dijke CF, Lu Y, et al. Quantification of the volume of articular cartilage in the metacarpophalangeal joints of the hand: accuracy and precision of three-dimensional MR imaging. AJR Am J Roentgenol 1995;165:371–375.
62. Nagy L. Salvage of post-traumatic arthritis following distal radius fracture. Hand Clin 2005;21:489–498.
63. Bordalo-Rodrigues M, Schweitzer M, Bergin D, Culp R, Barakat MS. Lunate chondromalacia: evaluation of routine MRI sequences. AJR Am J Roentgenol 2005;184:1464–1469.
64. Haims AH, Moore AE, Schweitzer ME, et al. MRI in the diagnosis of cartilage injury in the wrist. AJR Am J Roentgenol 2004;182:1267–1270.
65. Mutimer J, Green J, Field J. Comparison of MRI and wrist arthroscopy for assessment of wrist cartilage. J Hand Surg Eur Vol 2008;33:380–382.

66. Mosher TJ, Dardzinski BJ. Cartilage MRI T2 relaxation time mapping: overview and applications. Semin Musculoskelet Radiol 2004;8:355–368.
67. Wheaton AJ, Casey FL, Gougoutas AJ, et al. Correlation of T1rho with fixed charge density in cartilage. J Magn Reson Imaging 2004;20:519–525.
68. Duvvuri U, Reddy R, Patel SD, Kaufman JH, Kneeland JB, Leigh JS. T1rho-relaxation in articular cartilage: effects of enzymatic degradation. Magn Reson Med 1997;38:863–867.
69. Akella SV, Regatte RR, Borthakur A, Kneeland JB, Leigh JS, Reddy R. T1rho MR imaging of the human wrist in vivo. Acad Radiol 2003;10:614–619.
70. Timins ME, Jahnke JP, Krah SF, Erickson SJ, Carrera GF. MR imaging of the major carpal stabilizing ligaments: normal anatomy and clinical examples. Radiographics 1995;15:575–587.
71. Cohen MS, Kozin SH. Degenerative arthritis of the wrist: proximal row carpectomy versus scaphoid excision and four-corner arthrodesis. J Hand Surg Am 2001;26:94–104.
72. Feydy A, Pluot E, Guerini H, Drape JL. Osteoarthritis of the wrist and hand, and spine. Radiol Clin North Am 2009;47:723–759.
73. Brook A, Corbett M. Radiographic changes in early rheumatoid disease. Ann Rheum Dis 1977;36:71–73.
74. Fuchs HA, Kaye JJ, Callahan LF, Nance EP, Pincus T. Evidence of significant radiographic damage in rheumatoid arthritis within the first 2 years of disease. J Rheumatol 1989;16:585–591.
75. Sugimoto H, Takeda A, Masuyama J, Furuse M. Early-stage rheumatoid arthritis: diagnostic accuracy of MR imaging. Radiology 1996;198:185–192.
76. McQueen FM, Stewart N, Crabbe J, et al. Magnetic resonance imaging of the wrist in early rheumatoid arthritis reveals a high prevalence of erosions at four months after symptom onset. Ann Rheum Dis 1998;57:350–356.
77. McQueen FM, Benton N, Crabbe J, et al. What is the fate of erosions in early rheumatoid arthritis? Tracking individual lesions using x rays and magnetic resonance imaging over the first two years of disease. Ann Rheum Dis 2001;60:859–868.
78. McQueen FM, Stewart N, Crabbe J, et al. Magnetic resonance imaging of the wrist in early rheumatoid arthritis reveals progression of erosions despite clinical improvement. Ann Rheum Dis 1999;58:156–163.
79. Pierre-Jerome C, Bekkelund SI, Mellgren SI, Torbergsen T, Husby G, Nordstrom R. The rheumatoid wrist: bilateral MR analysis of the distribution of rheumatoid lesions in axial plan in a female population. Clin Rheumatol 1997;16:80–86.
80. Cimmino MA, Innocenti S, Livrone F, Magnaguagno F, Silvestri E, Garlaschi G. Dynamic gadolinium-enhanced magnetic resonance imaging of the wrist in patients with rheumatoid arthritis can discriminate active from inactive disease. Arthritis Rheum 2003;48:1207–1213.
81. Drape JL, Thelen P, Gay-Depassier P, Silbermann O, Benacerraf R. Intraarticular diffusion of Gd-DOTA after intravenous injection in the knee: MR imaging evaluation. Radiology 1993;188:227–234.
82. Jbara M, Patnana M, Kazmi F, Beltran J. MR imaging: arthropathies and infectious conditions of the elbow, wrist, and hand. Magn Reson Imaging Clin N Am 2004;12:361–379.
83. Vasanth LC, Foo LF, Potter HG, et al. Using magnetic resonance angiography to measure abnormal synovial blood vessels in early inflammatory arthritis: a new imaging biomarker? J Rheumatol 2010;37:1129–1135.
84. Gaffney K, Cookson J, Blades S, Coumbe A, Blake D. Quantitative assessment of the rheumatoid synovial microvascular bed by gadolinium-DTPA enhanced magnetic resonance imaging. Ann Rheum Dis 1998;57:152–157.
85. Cyteval C. Doppler ultrasonography and dynamic magnetic resonance imaging for assessment of synovitis in the hand and wrist of patients with rheumatoid arthritis. Semin Musculoskelet Radiol 2009;13:66–73.
86. Jbara M, Patnana M, Kazmi F, Beltran J. MR imaging: Arthropathies and infectious conditions of the elbow, wrist, and hand. Radiol Clin North Am 2006;44:625–642.

Quantitative MRI of Articular Cartilage and Its Clinical Applications

Xiaojuan Li, Ph.D., and Sharmila Majumdar, Ph.D.*

Reprinted from the ISMRM Journal of Magnetic Resonance Imaging: Volume 38: Pages: 991-1008, © 2013 from Wiley Periodicals, Inc.

This article is accredited as a journal-based CME activity. If you wish to receive credit for this activity, please refer to the website: www.wileyhealthlearning.com

ACCREDITATION AND DESIGNATION STATEMENT

Blackwell Futura Media Services designates this journal-based CME activity for a maximum of 1 *AMA PRA Category 1 Credit*™. Physicians should only claim credit commensurate with the extent of their participation in the activity.

Blackwell Futura Media Services is accredited by the Accreditation Council for Continuing Medical Education to provide continuing medical education for physicians.

EDUCATIONAL OBJECTIVES

Review the basic principles and clinical applications of major quantitative MRI techniques as a non-invasive tool for evaluating cartilage degeneration during osteoarthritis (OA), including techniques that grade and quantify morphologic changes as well as the techniques that quantify changes in the extracellular matrix.

ACTIVITY DISCLOSURES

No commercial support has been accepted related to the development or publication of this activity.

Faculty Disclosures:

Editor-in-Chief: Mark E. Schweitzer, MD, discloses DSMB work for Paradigm Spine, and consultation for MMI.

CME Editor: Scott B. Reeder, MD, PhD has no conflicts of interest to disclose.

CME Committee: Pratik Mukherjee, MD, PhD, Shreyas Vasanawala, MD, PhD, Bonnie Joe, MD, PhD, Tim Leiner, MD, PhD, Sabine Weckbach, MD, and Frank Korosec, PhD have no conflicts of interest to disclose. Scott K. Nagle, MD, PhD discloses a personal shareholder investment in GE. Mustafa R. Bashir, MD discloses research support from Bracco Diagnostics and Siemens Healthcare, and consultant honorarium from Bayer Pharmaceuticals.

Authors: Xiaojuan Li, PhD, and Sharmila Majumdar, PhD have nothing to disclose.

This manuscript underwent peer review in line with the standards of editorial integrity and publication ethics maintained by *Journal of Magnetic Resonance Imaging*. The peer reviewers have no relevant financial relationships. The peer review process for *Journal of Magnetic Resonance Imaging* is double-blinded. As such, the identities of the reviewers are not disclosed in line with the standard accepted practices of medical journal peer review.

Conflicts of interest have been identified and resolved in accordance with Blackwell Futura Media Services's Policy on Activity Disclosure and Conflict of Interest. No relevant financial relationships exist for any individual in control of the content and therefore there were no conflicts to resolve.

INSTRUCTIONS ON RECEIVING CREDIT

For information on applicability and acceptance of CME credit for this activity, please consult your professional licensing board.

This activity is designed to be completed within an hour; physicians should claim only those credits that reflect the time actually spent in the activity. To successfully earn credit, participants must complete the activity during the valid credit period.

Follow these steps to earn credit:

- Log on to www.wileyhealthlearning.com
- Read the target audience, educational objectives, and activity disclosures.
- Read the article in print or online format.
- Reflect on the article.
- Access the CME Exam, and choose the best answer to each question.
- Complete the required evaluation component of the activity.

This activity will be available for CME credit for twelve months following its publication date. At that time, it will be reviewed and potentially updated and extended for an additional period.

Musculoskeletal Quantitative Imaging Research Group, Department of Radiology and Biomedical Imaging, University of California, San Francisco, California, USA.

Contract grant sponsor: National Institutes of Health; Contract grant number: K25 AR053633; Contract grant number: R01 AR46905; Contract grant number: R01 AG17762; Contract grant number: U01 AR055079; Contract grant number: R21 AR056773; Contract grant number: P50 AR060752; Contract grant sponsor: the Aircast Foundation; Contract grant sponsor: Pfizer Inc; Contract grant sponsor: GlaxoSmithKline Inc; Contract grant sponsor: GE Healthcare.

*Address reprint requests to: S.M., QB3 Building, 2nd Floor, Suite 203, 1700 - 4th Street, San Francisco, CA 94158. E-mail: sharmila.majumdar@ucsf.edu

Received August 28, 2012; Accepted June 21, 2013.

DOI 10.1002/jmri.24313
View this article online at wileyonlinelibrary.com.

Cartilage is one of the most essential tissues for healthy joint function and is compromised in degenerative and traumatic joint diseases. There have been tremendous advances during the past decade using quantitative MRI techniques as a noninvasive tool for evaluating cartilage, with a focus on assessing cartilage degeneration during osteoarthritis (OA). In this review, after a brief overview of cartilage composition and degeneration, we discuss techniques that grade and quantify morphologic changes as well as the techniques that quantify changes in the extracellular matrix. The basic principles, in vivo applications, advantages, and challenges for each technique are discussed. Recent studies using the OA Initiative (OAI) data are also summarized. Quantitative MRI provides noninvasive measures of cartilage degeneration at the earliest stages of joint degeneration, which is essential for efforts toward prevention and early intervention in OA.

Key Words: osteoarthritis; cartilage; quantitative MRI
J. Magn. Reson. Imaging 2013;38:991–1008.

CARTILAGE COMPOSITION AND DEGENERATION

Hyaline cartilage consists of a low density of chondrocytes and a large extracellular matrix (ECM) (1). The ECM is composed primarily of water (~75% of cartilage by weight), and a cross-linked matrix with proteoglycans (PG) and type-II collagen fibers. The glycosaminoglycans (GAG) on PGs is highly negatively charged. A key function of these aggregates is to provide a stable environment of high fixed-charge density (FCD), essential for imbibing and retaining water in the tissue by the high osmotic swelling pressure created. The distribution and orientation of collagen in cartilage demonstrates anatomical zones at microscopy. The collagen fibers are oriented parallel to the articular surface in the superficial zone (10–20%), arcade like in the transitional zone (40–60%), and perpendicular in the radial zone (30–40%). The superficial zone can be further divided into two subzones: the lamina splenden, the more superficial layer with dense small fibrils and little polysaccharide and no cells; and the cellular layer with flattened chondrocytes and collagen fibers tangentially to the articular surface (http://www.wheelessonline.com/ortho/articular_cartilage). Below radial zone is a thin layer of calcified cartilage, separated by the tidemark. Although the etiopathogenesis of OA is not fully understood, it is believed that OA results from an imbalance between predominantly chondrocyte-controlled anabolic and catabolic processes, and is characterized by progressive degradation of the components of cartilage ECM (2). Changes at early stages of OA include hydration, PG loss, thinning and disruption of collagen, although it has been suggested neither the content nor the type of collagen is altered at early stages (1). Changes in late stages include dehydration, resulting in extensive fibrillation and loss of the cartilage and eventually denudation of the subchondral bone. Figure 1 illustrates the different stages of cartilage degeneration.

MORPHOLOGICAL CHANGES IN CARTILAGE IN OSTEOARTHRITIS

MR provides excellent soft tissue contrast and clinical evaluation of articular cartilage is normally based on proton density or intermediate-weighted fast spin-echo images. Both fat suppressed and nonfat suppressed images have been used. Fat-suppressed images provide better contrast between cartilage and surrounding tissues, while nonfat suppressed images permits higher spatial resolution without the loss of signal to noise afforded by routine fat suppression. Normally, a wider receiver bandwidth will be used in nonfat suppressed imaging to reduce chemical shift artifact at the cartilage–subcondral bone interface. Morphological grading of the cartilage to semi-quantify cartilage changes in OA have also been developed. The Whole Organ Magnetic Resonance Imaging Score (WORMS) of the knee in OA was proposed by Peterfy et al (3) and is one that characterizes multiple features in cartilage, meniscus, ligaments, bone marrow, all believed to be relevant to the pathophysiology of OA. Figure 2 shows representative MR images with corresponding WORMS scores. The Boston-Leeds OA Knee Score or the BLOKS score (4) focuses on bone marrow edema-like lesions and has been related to pain in OA.

Apart from the grading systems, high resolution typically fat-suppressed MR images have also been used to quantify cartilage thickness and volume. Apart from compartmental analysis (i.e., medial versus lateral compartment), subregional analysis of cartilage volume and thickness has been undertaken especially by Eckstein et al (5). Pulse sequences that are used to obtain images for cartilage volume estimation have high signal-to-noise ratio, high contrast-to-noise ratio, and high resolution as the cartilage thickness of a few mm warrants that the image resolution be as high as possible. Three-dimensional (3D) spoiled gradient echo images (SPGR) and several variants on these sequences such as dual echo steady state (DESS) images with different methods of fat suppression as well as newly developed 3D fast spin-echo images have been used for the assessment of cartilage morphology.

The steps involved in assessing cartilage volume and thickness include the segmentation of the cartilage. Several different image processing approaches have been proposed for this purpose. Stammberger and colleagues (6) applied a quadratic B-spline to guide the segmentation. An internal energy term controlled the rigidity of the contour, an external energy term attracted the contour to the cartilage edges, and a coupling force enforced smooth changes from one slice to another. In another 2D approach, Lynch et al (7) combined expert knowledge with cubic splines and image processing algorithms reporting better reproducibility and less user interaction than region growing techniques. Grau et al (8) extended the watershed

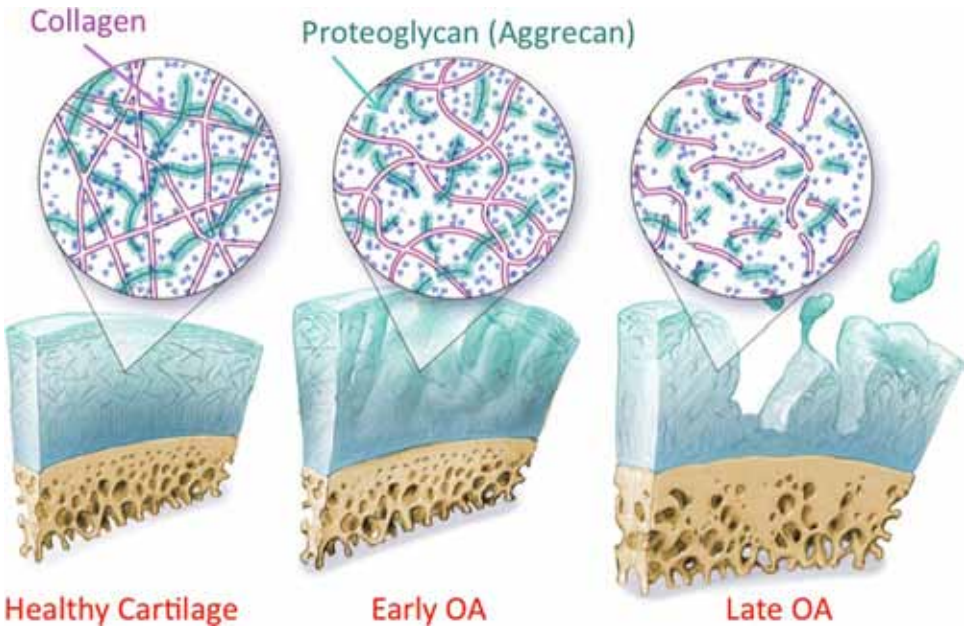

Figure 1. Articular cartilage degeneration during osteoarthritis (OA). Changes at early stages of OA include hydration, loss of proteoglycan, thinning and disruption of collagen. Changes in late stages include further loss of proteoglycan and collagen, dehydration, extensive fibrillation and cartilage thinning, and eventually denudation of the subchondral bone. [Color figure can be viewed in the online issue, which is available at wileyonlinelibrary.com.]

technique to examining difference in class probability of neighboring pixels. Pakin et al (9) used a region growing method with prior knowledge. Warfield and colleagues (10) developed an adaptive, template moderated, spatially varying statistical classification method, which consisted of an iterative technique between classification and template registration. Manual editing is often required in the context of semi-automated cartilage segmentation. After segmentation, the simplest morphological measure to compute is the sum of the total number of voxels representing cartilage, followed by corresponding scaling according to the voxel dimensions. The most common approach to compute cartilage thickness is based on 2D or 3D minimum Euclidean distances (11). For each point on the bone–cartilage interface or articular surface, the

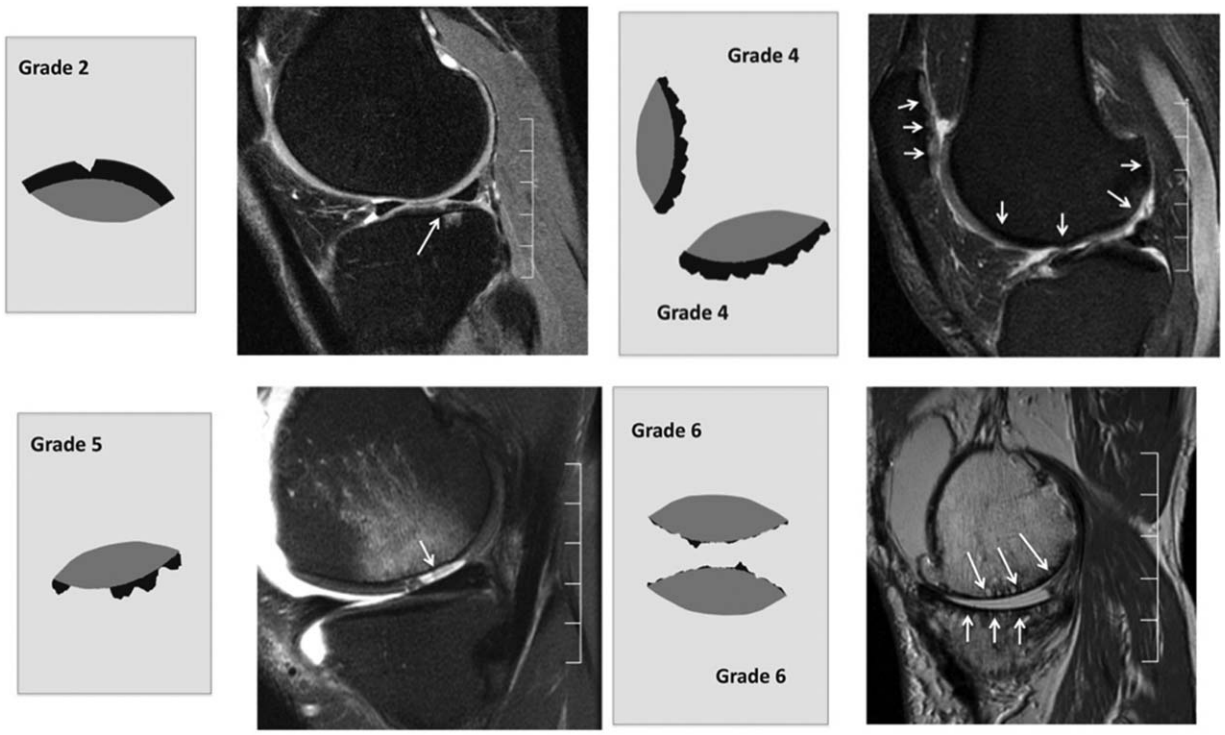

Figure 2. Representative MR images with different stages of cartilage lesions and the corresponding WORMS scores.

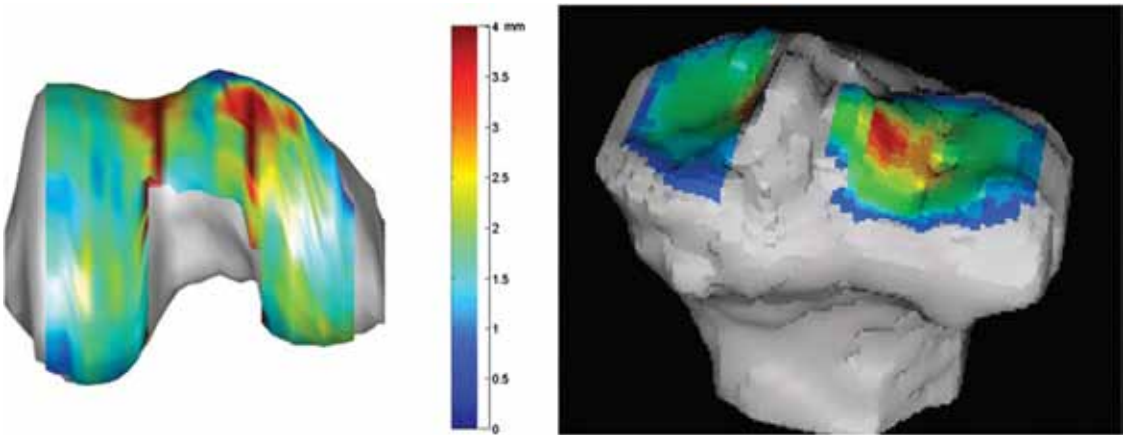

Figure 3. Cartilage thickness maps of the knee cartilage overlaying over the femur (left) and tibia (right) respectively.

closest point on the opposite surface is computed. Another 3D approach consists on computing normal vectors on one surface (articular or bone-cartilage interface), and finding the intersection of the vectors on the opposite surface (12). The average of the minimum distances or length of the vectors, respectively, is reported as the average cartilage thickness. Figure 3 shows a thickness map of the knee cartilage.

To obtain a measure of the spatial distribution of change (between time points) in cartilage volume and thickness, image registration is required. For this purpose, some investigators have used the bone–cartilage interface (13), whereas others have used the total bone shape (14). Once shapes have been aligned, matching of cartilage thickness patterns can be performed at a local level. Because there is an increasing interest in performing regional comparisons of cartilage properties at specific anatomic locations between different populations for a better understanding of OA, techniques have also been developed for this purpose (11,15). For intersubject comparisons, shapes have to be registered before any comparison, but in this case, scale factors as well as nonlinear differences between shapes have to be considered. The bone shape, and not only the interface, has recently been proposed for this type of matching (11). Figure 4 shows an intrasubject longitudinal example of cartilage thickness matching using the technique described by Carballido-Gamio and colleagues, which can also be applied for intersubject comparisons of cartilage properties (11).

Quantitative Morphology in the OAI

The OA Initiative, OAI (http://oai.epi-ucsf.org/datarelease/StudyOverview.asp), is a multi-center, longitudinal, prospective observational study of knee OA. The aim of the OAI is to develop a public domain research resource to facilitate the scientific evaluation of biomarkers for OA as potential surrogate endpoints for disease onset and progression. The OAI data includes clinical evaluation data, imaging (x-ray and 3 Tesla MR), and a biospecimen repository from 4796 men and women ages 45–79 years. The participants include those who are at high risk for developing, symptomatic knee OA. Using the MR data from these studies investigators have determined that the MR sequences used to estimate the cartilage thickness and volume have adequate reproducibility. Rates of change for cartilage morphological measures in different regions have been proposed as a function of radiographic disease extent, existence of pain, and predictor of knee replacement, which has been recently reviewed by Eckstein et al (16).

QUANTITATIVE MRI FOR CARTILAGE MATRIX COMPOSITION

As discussed previously, cartilage degeneration starts with changes in hydration and the macromolecular structures, specifically PG and collagen network, within the matrix. Techniques that are sensitive and specific to these changes are ideal for early detection of cartilage degeneration. Water content in cartilage has been quantified by using proton density images after corrections of T_1 and T_2 relaxation values, which however has limited sensitivity of detecting early cartilage degeneration due to the relatively small changes of water contents in osteoarthritic cartilage (up to 9%) (17). Current efforts have been made more toward measuring the changes associated with marcomolecular changes, PG and collagen, within the matrix. However, both PG and collagen protons sustain very short T_2 relaxation time due to their macromolecular structures, and it is difficult to measure them directly with MRI, except for using ex vivo high field NMR techniques. As a result, current MRI techniques are primarily focused on sensitizing the measurement of water proton signals to the macromolecular contents and structures in the matrix based on energy and magnetization exchange between bulk-water protons and protons associated with macromolecules. We classified the quantitative MRI methods for cartilage matrix biochemistry into four categories: (i) methods based on relaxometry including T_1 (with and without presence of contrast agent), T_2 and $T_{1\rho}$ relaxation time quantification; (ii) methods based on diffusion measurement; (iii) methods

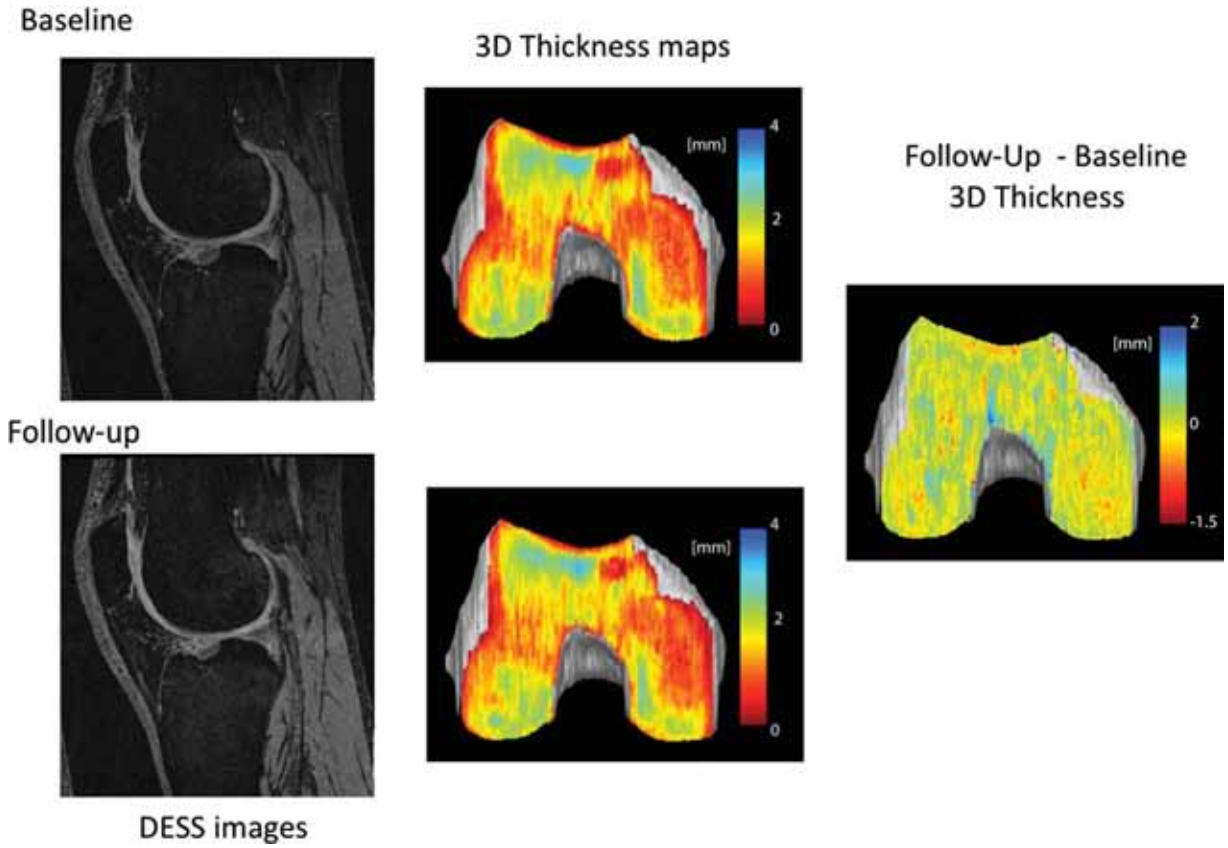

Figure 4. An example of intrasubject longitudinal cartilage thickness matching using the technique described by Carballido-Gamio et al (11). DESS: dual echo steady state.

based on magnetization transfer measurement including conventional magnetization transfer and chemical exchange saturation transfer (CEST); and (iv) a nonproton method, sodium imaging.

Postcontrast T_1 Relaxation Time by Delayed Gadolinium-Enhanced Proton MRI of Cartilage

Basic Principles

As T_1 reflects activities with relaxation correlation time in the range of $1/(\gamma B_0)$, native T_1 measurement is normally not sensitive to cartilage matrix changes due to the slow motion of the restricted protons in the matrix. However, delayed gadolinium (Gd)-enhanced proton MRI of cartilage (dGEMRIC) has been developed to quantify PG content in cartilage by quantifying T_1 with the presence of the contrast agent (18,19). It is based on the fact that PG, or the associated GAG, has abundant negatively charged carboxyl and sulfate groups. In the study of dGEMRIC, contrast agent of gadolinium diethylene triamine pentaacetic acid, or Gd-DTPA^{2-} (Magnevist; Berlex Laboratories, Wayne, NJ), is injected intravenously (or intra-articularly) and distributed in the cartilage by diffusion. The diffusion time depends on the cartilage thickness and is approximately two hours in femoral weight-bearing

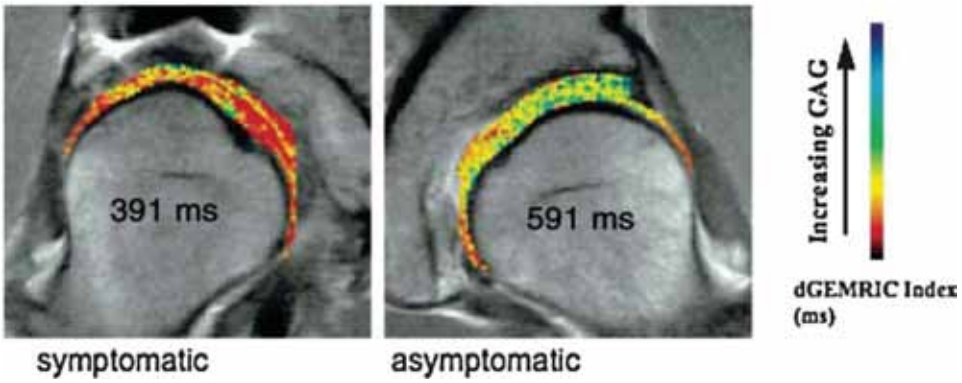

Figure 5. dGEMRIC images of the hips of a patient with unilateral hip dysplasia. The symptomatic hip has a much lower dGEMRIC index. Numbers in the images refer to the average dGEMRIC index for the region shown in color. (Figure reprinted from reference (29), with permission).

cartilage. Because Gd-DTPA^{2-} is negatively charged, it will be distributed in a relatively low concentration in areas that are rich in GAG (normal cartilage), and in higher concentrations in regions with depleted GAG (degenerated cartilage). Gd-DTPA^{2-} has a concentration-dependent effect on the MR parameter T_1. Therefore, T_1-weighted images in the presence of Gd-DTPA^{2-} reflect the Gd-DTPA^{2-} concentration, and hence tissue GAG concentration. By calculating T_1 relaxation time, the concentration of GAG can be quantified based on a modified electrochemical equilibrium theory, assuming the Gd-DTPA^{2-} is equilibrated in the tissue (18).

dGEMRIC measures have been validated using biochemical and histologic measurements of GAG concentration in cartilage with ex vivo studies, as reviewed by Gray et al (19). The in vivo validation of dGEMRIC techniques, however, was not straightforward especially for the conversion from T_1 quantification to GAG concentration, therefore the direct T_1 measures of "dGEMRIC index" was normally reported for clinical studies (19). Loss of GAG will result in a decreased T1, and a decreased "dGEMRIC index".

In Vivo Applications

The sequences for in vivo T_1 quantification in dGEMRIC studies include the most commonly used two-dimensional (2D) inversion recovery fast spin-echo (IR-FSE) sequences due to its widespread availability of the sequence and desirable contrast properties (cartilage versus fluid), 3D acquisitions based on IR-spoiled gradient echo (IR-SPGR) for better coverage, and fast 3D methods based on Look-Locker or based on spoiled GRE images with two optimized flip angles. Good correlations were reported between measures from the 3D methods and the gold-standard 2D IR-FSE technique. The reproducibility of the 3D-variable flip angle method (RMS-CV: 9.3–15.2%) was reported to be inferior compared with 2D-IR FSE and 3D Look Locker methods (RMS-CV: 5.8–8.4%) (20). In particular, the investigators suggested that positioning of the analyzed images is crucial to generate reliable repeatability results. The recommended clinical protocol was summarized by Burstein et al (21).

Decreased dGEMRIC index was observed in compartments with radiography joint space narrowing compared with other compartments (22). In obese subjects, knee dGEMRIC index was associated with age, clinical knee OA, abnormal tibiofemoral alignment, and quadriceps strength (23). Subjects with medial meniscectomy (1–6 years before imaging) showed significantly lower dGEMRIC Index of the medial compartment after surgery (24). In subjects with acute anterior cruciate ligament (ACL) injuries, significantly decreased dGEMRIC index was observed in ACL-injured knees compared with either contralateral knees or knees from healthy control subjects (25,26), suggesting that dGEMRIC index may be indicative of potential early degeneration in knees with risk of developing posttraumatic OA.

In the hip, lower dGEMRIC index was reported in subjects with femoroacetabular impingement (FAI) with different patterns of subregional variation between subjects with cam and pincer FAI (27), and was correlated with the magnitude of the deformity and pain (28). In subjects with hip dysplasia, a developmental malformation of the hip associated with early OA, Kim et al reported that dGEMRIC significantly correlated with severity of dysplasia and pain (29), Figure 5.

Advantages and Challenges

Previous studies support the dGEMRIC index as a clinically relevant measure of cartilage integrity, with specific measures related to GAG concentration. However, one should be aware that especially for in vivo studies, bias may be introduced during conversion from dGEMRIC measures to GAG concentration due to factors such as the possibility of altered contrast agent relaxivity under different tissue conditions and other factors such as the transport of contrast agent into cartilage with a variable blood concentration that might affect the equilibrating concentration of Gd(DTPA) $^{2-}$ in vivo (19). Other challenges that hinder dGEMRIC from widespread clinical application including necessity of contrast agent injection, and long delay of MR scan after Gd injection.

T_2 Relaxation Time

Basic Principles

T_2 relaxation time, or the spin-spin relaxation time, reflects the ability of free water proton molecules to move and to exchange energy inside the cartilaginous matrix. It has been shown that in normal cartilage this transverse (T_2) relaxation is dominated by the anisotropic motion of water molecules in a fibrous collagen network. Damage to collagen-PG matrix and increase of water content in degenerating cartilage may increase T_2 relaxation times.

T_2 quantification is normally performed by fitting T_2-weighted images acquired with different TEs to mono- or multi-exponential decay curve. Pai et al compared the T_2 mapping techniques in phantoms and in vivo based on five different sequences with regard to SNR, reproducibility and quantification: spin-echo (SE), fast spin-echo (FSE), multi-echo SE (MESE), magnetization prepared 2D spiral, and magnetization prepared 3D SPGR (30). Variation of T_2 quantification was observed, Figure 6, which may due to different sensitivity of each sequences to system imperfections including stimulated echoes, off resonance signals and eddy currents. Different fitting methods will also introduce bias to T_2 quantification. Caution needs to be exercised when comparing results from different studies and when designing a multi-center study.

In vitro studies have reported that T_2 correlated with water content but poorly with PG depletion in enzymatically degraded articular cartilage (31). Using high field microscopic MRI (μMRI), Xia et al showed that T_2 spatial variation is dominated by the ultra-structure of collagen fibrils, and thus angular dependency of T_2 with respect to the external magnetic field B_0 can

provide specific information about the collagen structure (32). T_2 variation was also correlated with polarized light microscopy (33). This angular dependency of T_2 results in the "magic angle" effect and the commonly seen laminar appearance in cartilage imaging. Multi-exponential T_2 relaxation components were identified by Reiter et al using intact and enzyme-digested bovine nasal cartilage (34). Using bovine nasal cartilage, it was demonstrated that the multicomponent properties may depend on the orientation of collagen fibers with respect to B_0. At the magic angle (55°), T_2 (and $T_{1\rho}$) was a single component rather than multiple components (35). This multiexponential approach has the potential to improve specificity of cartilage matrix evaluation using T_2 relaxation parameters.

In Vivo Applications

In vivo T_2 values have been shown to vary from the subchondral bone to the cartilage surface (36,37). With the exception of the lamina splendens, T_2 decreased from the superficial layer to the deep layer. Cartilage T_2 has been correlated with age (38), but not with gender (39). Elevated T_2 relaxation times were observed in OA cartilage, and were associated with the severity of disease categorized with radiography (40). In one study examining T_2 in patellar cartilage, however, no differences of T_2 values were found across the stages of OA based on radiographic KL scores ($P = 0.25$) (41). The same study reported increased T_2 was associated with increased BMI, suggesting BMI is a significant factor for increasing T_2. Increase of T_2 (and $T_{1\rho}$) was also correlated with decreased trabecular bone structure in OA knees, highlighting the interplay between cartilage and bone structure in OA (42,43).

T_2 quantification has been used as noninvasive measures to quantify and monitor the change in biochemical and biomechanical properties of cartilage after physical activity or exercise. Mosher et al reported that cartilage T_2 values decreased after running, along with a decrease in cartilage thickness (44), suggesting the decrease of water contents and changes of collagen network after high impact activity such as running. A more recent study showed the greatest decrease of T_2 and $T_{1\rho}$ after running occurred in the superficial layer of medial femoro-tibial and patella-femoral cartilage (45), suggesting greater load sharing by these areas during running. Further studies in subjects with OA would be interesting to examine the loading pattern and cartilage response to running in degenerative joints.

T2 quantification has been also applied in evaluating early cartilage matrix changes after acute injuries, such as acute anterior cruciate (ACL) tears. In a very recent longitudinal study, Potter et al reported that T2 values were elevated during follow-ups (up to 11 years after injury) in the lateral side and patella after isolated ACL tears (T2 values in the medial side were not available), indicating accelerated cartilage degradation in such joints (46). The T2 elevation was observed in regions that were not covered by the initial bone marrow edema-like lesions, suggesting the injury initiated a rather global disturbing of cartilage homeostasis within the whole joint.

In vivo T_2 quantification using a multi-slice multi-echo spin-echo (MESE) sequence has been included in the OA Initiative. Data from the monthly quality assurance procedure over a 3-year period showed

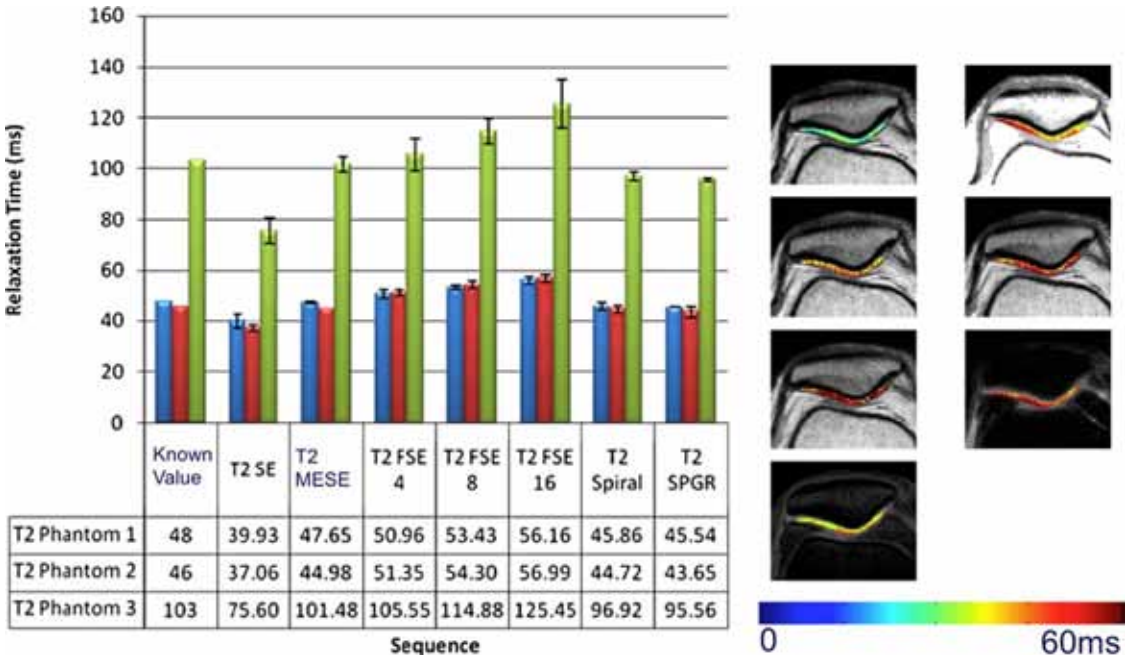

Figure 6. Variation of T_2 quantification was observed using different sequences in phantoms (left) and in vivo knees (right) (30). SE: spin-echo; FSE-4: fast spin-echo (FSE) with echo train length (ETL) as 4; FSE-8: FSE with ETL as 8; FSE-16: FSE with ETL as 16; MESE: multi-echo spin-echo; SGPR: spoiled gradient echo acquisition. [Color figure can be viewed in the online issue, which is available at wileyonlinelibrary.com.]

excellent longitudinal reproducibility (RMS CV < 5%) except for one site (47). Cartilage T_2 values have been correlated to physical activity levels (determined by Physical Activity Scale for the Elderly), in particular knee bending activities, in OAI cohort (48). Light exercisers had lower T_2 values compared with both sedentary and moderate/strenuous exercisers in subjects with risk factors for knee OA (n = 128), Figure 7, suggesting that there could be a "U" shape of the effect of exercise to cartilage biochemistry—either too little or too much will be detrimental, but the optimized appropriate level of exercise for each individual may be affected by many factors including BMI, genetic profile, biomechanical characteristics such as alignment and kinematics. Nonetheless, as exercise is a modified factor, exploring the relationship of different type and level of exercise to cartilage biochemistry as quantified by advanced MRI can be clinically valuable to allow intervention and training to prevent and slow down cartilage degeneration.

Using OAI data, a 2-year longitudinal analysis of OAI normal cohort showed a significant increase in T_2 was in the tibiofemoral cartilage while no changes in the patellofemoral cartilage (49). A greater increase in cartilage T_2 was found to correlate with an increase in the progression of cartilage abnormalities (graded with WORMS). More recently, Joseph et al reported, in OAI subjects with risk factors for OA (n = 289), the baseline mean and heterogeneity of cartilage T_2 were significantly ($P < 0.05$) associated with morphologic joint degeneration in the cartilage, meniscus and bone marrow over 3 years (50). These studies suggested that characterizing and monitoring the cartilage matrix integrity with T_2 measurements might enable identification of individuals at risk for the development of early OA before irreversible cartilage loss occurs.

Advantages and Challenges

Cartilage T_2 quantification is a promising marker for cartilage matrix biochemistry and has been applied in the large multicenter studies of OA with the effort of the OAI. T_2 changes are dominated by the hydration and collagen fibers and may not be sensitive to subtle changes of PG loss. Caution is also needed during data interpretation due to the magic angle effect of T_2. In addition, due to the layer variation of cartilage T_2 as discussed earlier, laminar analysis is recommended to be used for analyzing either OA or cartilage repair data. It should be noted that sampling quantitative data in the superficial zone or lamina splendens is technically challenging, and normally two layers (with equal thickness) were used for in vivo T2 laminar analysis due to the limited resolution of in vivo T2 mapping.

$T_{1\rho}$ Relaxation Time Quantification

Basic Principles

The $T_{1\rho}$ parameter is defined as the time constant describing the spin-lattice relaxation in the rotating frame. It probes the slow motion interactions between motion-restricted water molecules and their local macromolecular environment. The macromolecules in articular cartilage ECM restrict the motion of water molecules. Changes to the ECM, such as PG loss, therefore, can be reflected in measurements of $T_{1\rho}$. The $T_{1\rho}$ is normally measured by the spin-lock (SL) technique, which enabled study of relaxation at very low field without sacrificing the SNR afforded by higher field strengths. In an SL experiment, spins are flipped into the transverse plane along one axis, immediately followed by a SL pulse applied along the same axis. A SL pulse is an on-resonance, continuous wave radiofrequency (RF) pulse, normally long-duration and low-energy. Because the magnetization and RF field are along the same direction, the magnetization is "spin-locked", provided the locking condition is satisfied, i.e., the B_1 of locking pulses is much stronger than the local magnetic fields generated by, for example, magnetic moments of nuclei. The spins will relax with a time constant $T_{1\rho}$ along B_1 of locking pulses in the transverse plane. The amplitude of the

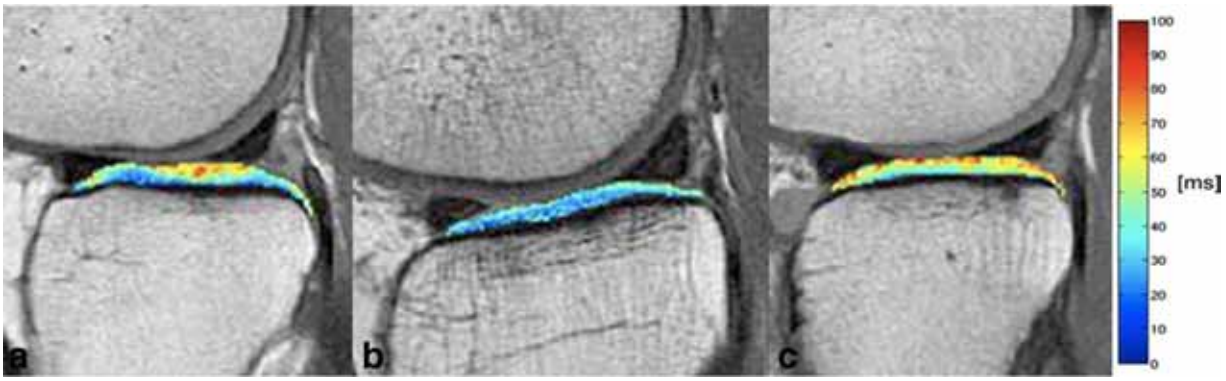

Figure 7. T_2 maps of a sedentary subject (**a**), a light exerciser (**b**), and a moderate/strenuous exerciser (**c**) from the OAI cohort with risk factors for knee OA. In subjects with risk factors for knee OA from OAI cohort, light exercisers had lower T_2 values compared with both sedentary and moderate/strenuous exercisers (48), suggesting that there could be a "U" shape of the effect of exercise to cartilage biochemistry. [Color figure can be viewed in the online issue, which is available at wileyonlinelibrary.com.]

SL pulse is commonly referenced in terms of the nutation frequency ($f = \gamma B_1$). The normal range of SL frequency is a few hundred hertz to a few kilohertz. $T_{1\rho}$ relaxation phenomena are sensitive to physicochemical processes with inverse correlation times on the order of the nutation frequency of the SL pulse. $T_{1\rho}$ increases as the strength of the SL field increases, a phenomenon termed $T_{1\rho}$ dispersion. $T_{1\rho}$ dispersions may also have tissue specificity.

The $T_{1\rho}$-weighted imaging sequences are composed of two parts: magnetization preparation with $T_{1\rho}$ weighting using spin-lock pulse cluster, and a following 2D (based on spiral, or fast spin-echo, or echo planar imaging) or 3D (based on gradient echo or 3D fast spin echo) data acquisition. Compared with 2D acquisition, 3D sequences have the advantage of higher image resolution, especially in the slice direction. Among 3D sequences, the method using transient signals immediately after $T_{1\rho}$ preparation either based on SPGR acquisition (51) (magnetization-prepared angle-modulated partitioned *k*-space spoiled gradient echo snapshots, MAPSS) or based on balanced GRE acquisition (52) are more SNR efficient and less SAR intensive compared with the method based on the steady state GRE acquisition (53). These sequences have been implemented at both 1.5 Tesla (T) and 3T on scanners from different manufactures. Several modifications in the SL pulse cluster and phase cycling were performed to improve the robustness of spin locking to B_0 and B_1 inhomogeneity (54,55).

In vitro studies have showed that the elevation of $T_{1\rho}$ relaxation time was correlated with PG loss in both bovine (31) and human cartilage (56), and with histological grading (56). In $T_{1\rho}$ quantification experiments, the spin-lock techniques reduce dipolar interactions and, therefore, reduce the dependence of the relaxation time constant on collagen fiber orientation. This enables more sensitive and specific detection of changes in PG content using $T_{1\rho}$ quantification, although $T_{1\rho}$ changes in cartilage may be affected by hydration and collagen structure as well. The reduced dipolar interaction also results in less "magic angle effect" in $T_{1\rho}$ imaging as compared to T_2 imaging. Less laminar appearance was observed in $T_{1\rho}$-weighted images compared with T_2-weighted images (57). Previous specimen studies reported that $T_{1\rho}$ values at the magic angle (54.7°) were significantly higher than at other angles, but the difference was smaller than the difference in T_2 values at the same angles (56). The difference was decreased with increased $T_{1\rho}$ spin-lock frequencies and was diminished when $T_{1\rho}$ spin-lock frequency was equal to or higher than 2 KHz (57).

Previous studies suggested that proton exchange between NH and OH groups of GAG and bulk water contribute significantly to the $T_{1\rho}$ relaxation (58), while another study suggested that the contribution of scalar relaxation caused by proton exchange is only relevant at high fields such as 7T (59). Other evidence of a proton exchange pathway is the PH dependency of $T_{1\rho}$ values in the ischemic rat brain tissues (60). Further investigations are needed to better understand this relaxation mechanism in cartilage.

In Vivo Applications

In vivo $T_{1\rho}$ reproducibility (scan-rescan studies at a single center) was reported to range from 1.7–8.7% (51). A recent multicenter study reported reproducibility CVs for both T_2 (4–14%) and $T_{1\rho}$ (7–19%) (61). Future studies are warranted to evaluate multi-site multi-vendor variation of $T_{1\rho}$ and T_2 quantification with a clinical trial setup. In vivo studies suggested $T_{1\rho}$ is moderately age-dependent (62). Increased cartilage $T_{1\rho}$ values was observed in OA subjects compared with controls (40,42,53,62), in asymptomatic active healthy subjects with focal cartilage abnormalities compared with those without lesions (62), in subjects with meniscal tears compared with those without tears (63), and in regions overlying bone marrow edema-like lesions (BMEL) compared with surrounding cartilage in OA and acutely-injured knees (64). Furthermore, elevated $T_{1\rho}$ was observed in subcompartments in OA subjects where no obvious morphologic changes were observed, suggesting the capability of $T_{1\rho}$ in detecting very early biochemical changes within the cartilage matrix (40).

Similar as T_2, $T_{1\rho}$ values decreased from the superficial zone (excluding the lamina splendens) to the deep zone of cartilage (37). Although the trend of $T_{1\rho}$ and T_2 values are similar, $T_{1\rho}$ shows a larger dynamic range and less laminar appearance was observed in $T_{1\rho}$-weighted images compared with T_2-weighted images due to reduced dipolar interaction during $T_{1\rho}$ relaxation (57). In human subjects, the pixel-by-pixel correlation between $T_{1\rho}$ and T_2 was reported to have a large range in both controls and OA patients ($R^2 = 0.522 \pm 0.183$, ranging from 0.221 to 0.763 in OA patients versus $R^2 = 0.624 \pm 0.060$, ranging from 0.547 to 0.726 in controls) (37). Figure 8 shows $T_{1\rho}$ and T_2 maps from a control subject, a subject with mild OA, and a subject with severe OA. The differences between the $T_{1\rho}$ and T_2 maps are evident. These results suggested $T_{1\rho}$ and T_2 show different spatial distribution and may provide complementary information regarding cartilage degeneration in OA. Combining these two parameters may further improve our capability to diagnose early cartilage degeneration and injury.

In addition to patients with OA, $T_{1\rho}$ quantification techniques have been applied to patients with acutely injured knees, who have a high risk of developing OA later in life. In patients with acute ACL tears, significantly increased $T_{1\rho}$ values were found at baseline (after injury but before ACL reconstruction) in cartilage overlying bone marrow edema-like lesions (BMEL) when compared with surrounding cartilage at the lateral tibia (64). Follow-up exams at 1-year after ACL-reconstruction of these ACL injured knees (65) showed that (i) in lateral sides, despite the resolution of BMEL, cartilage overlying the baseline BMEL still show significantly higher $T_{1\rho}$ compared to controls, suggesting potential irreversible damage of cartilage in these regions; (ii) in medial sides, $T_{1\rho}$ values in medial tibial and medial femoral condyles, especially the contact area (the contact area during supine unloaded MRI), show significant elevation at as early as 1-year after ACL reconstruction compared with

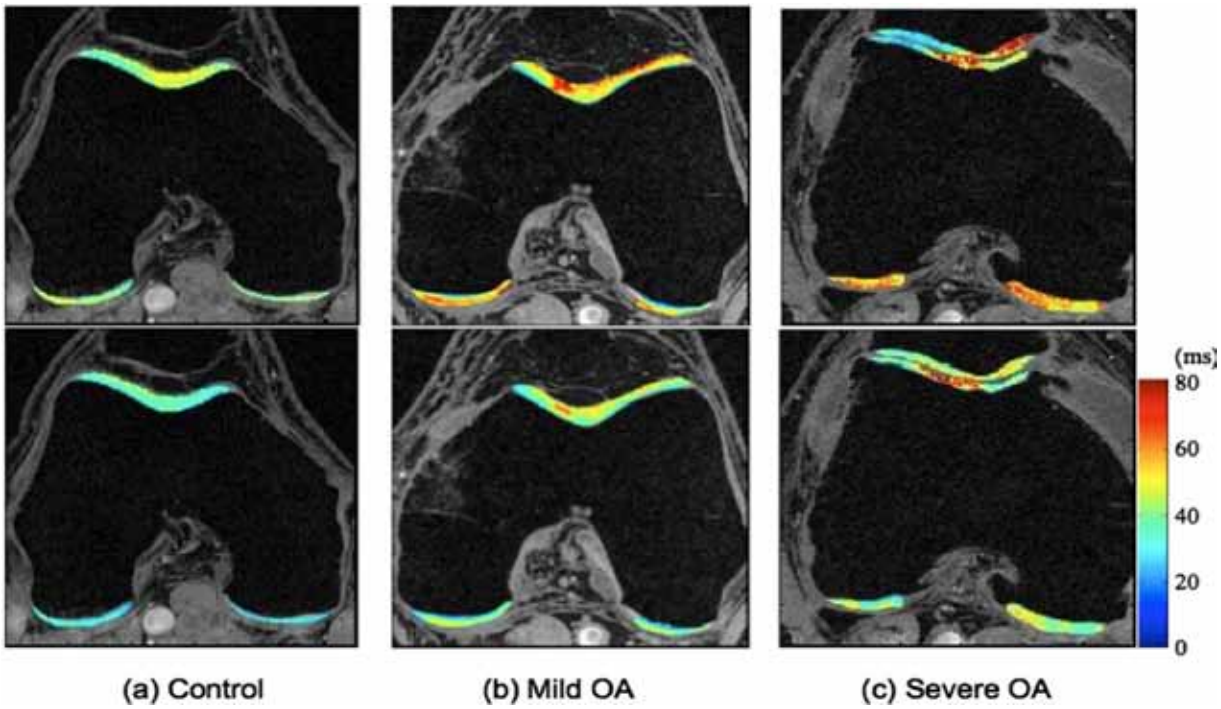

Figure 8. $T_{1\rho}$ and T_2 maps of a healthy control (**a**), a subject with mild OA (**b**), and a subject with severe OA (**c**). Significant elevation of $T_{1\rho}$ and T_2 values were observed in subjects with OA. $T_{1\rho}$ and T_2 elevation had different spatial distribution and may provide complementary information associated with cartilage degeneration. [Color figure can be viewed in the online issue, which is available at wileyonlinelibrary.com.]

healthy controls, probably due to abnormal kinematics even after ACL reconstruction, Figure 9. T_2 also showed increasing trend in these regions of cartilage, however it did not reach statistical significance. The authors speculated that $T_{1\rho}$ is more sensitive than T_2 in detecting cartilage damages and potential early degeneration in ACL-injured knees (65). It should be noted that at the spin-lock frequencies that are commonly used for in vivo studies (400–500 Hz), $T_{1\rho}$ quantification also showed orientation dependency as discussed earlier. Therefore, $T_{1\rho}$ values of subregions along the femoral condyles cannot be compared directly. Rather, the values should be compared with match-regions in control knees. To increase the spin-lock frequency will decrease the orientation dependency, but the highest spin-lock frequency will be limited by the energy deposited to the tissue as evaluated by specific absorption rate (SAR) or by the maximum B1 allowed by the hardware.

Advantages and Challenges

$T_{1\rho}$ quantification in cartilage can provide valuable information related with biochemical changes in cartilage matrix. In particular, compared with more established T_2 relaxation time, $T_{1\rho}$ provides a larger dynamic range and a more sensitive detection of PG loss at early stages of cartilage degeneration. Similar as T_2 quantification, $T_{1\rho}$ quantification requires no contrast agent injection and no special hardware, therefore has great potential to be used in clinical applications or trials. Technical challenges of $T_{1\rho}$ quantification include high energy deposited to tissue (high SAR), especially at high and ultra high field strength.

Magnetization Transfer (MT) and Chemical Exchange-Dependent Saturation Transfer (CEST) MRI

MR imaging techniques based on magnetization transfer (MT) are sensitive to marcomolecular changes in tissues by exploring the exchange of magnetization between the pool of semisolid macromolecule associated protons and the pool of more free or liquid protons associated with bulk water (66). During MT experiments, the macromolecule-bounded protons are preferentially saturated with selective off-resonance RF pulses. The exchange of magnetization that transfers macromolecular saturation to the liquid proton pool produces an observable decrease in the longitudinal magnetization of the liquid spins. The magnetization exchange can occur by means of dipolar coupling or by means of chemical exchange. The most common parameter to quantify the amount of MT is by calculating the MT ratio (MTR) of the signal intensity before and after saturation.

The magnetization transfer effect in cartilage has been attributed primarily to collagen (67), while studies showed that changes in PG concentration and tissue structure also contribute to changes in MT ratio in cartilage (68). It is worthy of noting that, although MTR provides valuable information regarding tissue composition, MTR is not an intrinsic MR property of tissue. This parameter is reflective of a complex combination of the sequence, tissue relaxation and MT

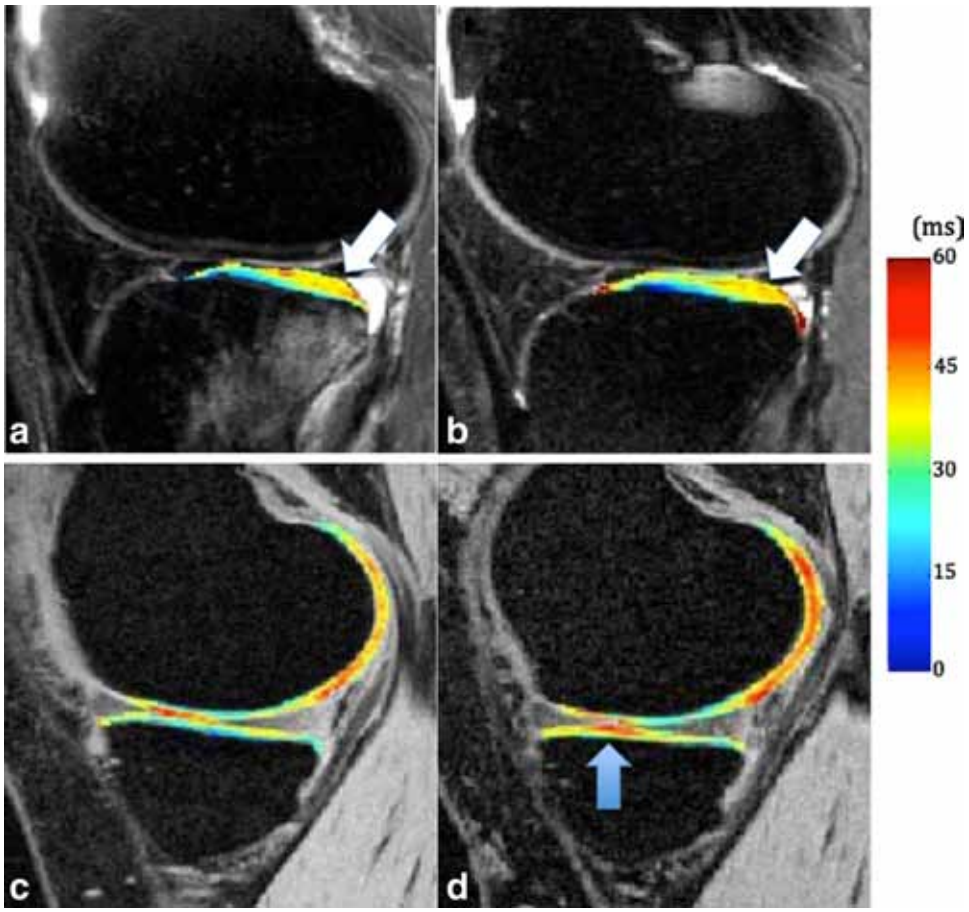

Figure 9. $T_{1\rho}$ maps of the lateral side (**a, b**) and medial side (**c,d**) of an ACL-injured knee at baseline (**a, c**) and 1-year follow-up (**b, d**) (65). $T_{1\rho}$ values in lateral-posterior tibial cartilage (the region overlying bone bruises, white arrows) were elevated significantly in ACL-injured knees at baseline and remained high at 1-year follow-up, despite resolution of bone bruise in lateral tibia. $T_{1\rho}$ values in the contacting area of medial femoral condyle and medial tibia (blue arrow) were significantly elevated in ACL-injured knees at 1-year follow-up. [Color figure can be viewed in the online issue, which is available at wileyonlinelibrary.com.]

parameters. In an effort to decouple the contribution of each of these parameters, quantitative magnetization transfer (qMT) techniques have been proposed (69,70). These methods derive the fraction of exchanging protons that are bound to macromolecules and the exchange rate between the bound and free pool based on the two-compartment model. A recent study applied qMT techniques in bovine cartilage and revealed that in the top layer of cartilage, the bound pool fraction was moderately correlated with PG content while the cross-relaxation rate and the longitudinal relaxation time were moderately correlated with collagen (71). More studies in the future are warranted to examine the feasibility and validity of qMT in assessing matrix composition of healthy and degenerated cartilage.

Chemical exchange-dependent saturation transfer (CEST) imaging is a relatively new MRI contrast approach (72). In CEST experiments, exogenous or endogenous compounds containing either exchangeable protons or exchangeable molecules are selectively saturated and after transfer of this saturation upon chemical exchange to the bulk water, detected indirectly through the water signal with enhanced sensitivity. In CEST MRI, transfer of magnetization is studied in mobile compounds instead of semisolids in contrast to conventional MT.

To account for direct saturation of water and background magnetization transfer that is related to mechanism other than chemical exchange, such as nuclear overhauser effect (NOE) in cartilage (73), two images are normally acquired in CEST experiments. One with a saturation pulse applied at the resonance frequency of interest ($-\delta$), and the other acquired with an equal frequency offset but applied on the other side of the bulk water peak (δ). The CEST effect was then quantified as the difference of these two images (73).

In cartilage, CEST exploits the exchangeable protons, including NH, OH, and NH_2 proton groups, on the GAG side chains of PG (73,74), and was termed as gagCEST. Ling et al showed that $-$OH at $\delta = -1.0$ ppm, where δ is the frequency offset relative to the water, among other labile protons, can be used to monitor GAG concentration in cartilage in vivo (73). gagCEST revealed difference in GAG concentration between trypsin PG-depleted cartilage versus controls, and low GAG concentration in vivo with focal cartilage lesion (73), Figure 10. At 7T, a strong correlation ($r = 0.701$) was found between ratios of signal intensity from native cartilage to signal intensity from repair

tissue obtained with gagCEST (asymmetries in gagCEST z-spectra summed over all offsets from 0 to 1.3 ppm) or ^{23}Na imaging (74), which suggested the specificity of gagCEST for detecting GAG concentration.

gagCEST is a promising new method of evaluating cartilage matrix composition, with high specificity to GAG concentration and no need of contrast agent injection. However, the sensitivity to multiple factors, including pH changes, changes in hydration and collagen that may also change the exchange rate of −OH protons, and to pulse sequence parameters complicates the interpretation of gagCEST and comparison studies between laboratories. In addition, the field inhomogeneity, susceptibility-induced artifacts and motion may confound the results from gagCEST experiments. Furthermore, at 3T, the slow-to-intermediate exchange condition, $\Delta\omega > k$ (where $\Delta\omega$ is the chemical shift of the solute spin relative to bulk water proton, and k is the exchange rate of solute spin), which is needed to efficiently observe CEST effect, is not fulfilled for −OH protons with exchange site at 1 ppm. The CEST effect is expected to increase at ultra high field strength such as 7T. The advantage includes the larger frequency separation for better adherence to the slow-exchange condition and reduced interference of direct water saturation, and the limitation includes the increase in power deposition.

Diffusion Imaging

Diffusion MRI measures Brownian motion of water molecules in tissues, which provides a noninvasive method for evaluating microscopic cellular structures of the tissue. Diffusion-weighted images provide a new contrast qualitatively related to tissue properties. Diffusion tensor imaging (DTI) where diffusion weighted images are acquired in multiple directions can provide quantitative information, including the mean diffusivity (MD) or apparent diffusion coefficient (ADC), indicating the degree of water diffusion, and the fractional anisotropy (FA), indicating the anisotropy of water diffusion in different orientations.

Ex vivo studies have documented promising results that MRI diffusion parameters may be sensitive to both the PG content and the collagen architecture within cartilage matrix, and therefore can be promising indicators of early degeneration of the tissue (75–77). Zonal variation was observed where ADC continuously decreased and FA increased from the articular surface to the bone-cartilage interface (77). The collagen fiber architecture has been shown to be the primary source of the anisotropy of diffusion (75,76). The primary eigenvector of the diffusion tensor (i.e., the eigenvector associated with the largest eigenvalue) has been shown to correlate with the orientation of the collagen fibrils using polarized light microscopy (PLM) (76) and scanning electron microscopy (77). Loss of PG caused significant increases of mean diffusivity and minimal changes in FA, while collagen depletion led to changes of ADC, fractional anisotropy (FA), and primary eigenvector (75).

Despite promising results from ex vivo studies, in vivo quantification of diffusion coefficients in cartilage are rather limited due to the short T_2 and consequently low SNR in cartilage, as well as spatial distortions arising from the sensitivity of the EPI trajectory to B_0 field inhomogeneity (therefore, the commonly used EPI based diffusion sequences are not optimal for cartilage imaging). Very recently, Staroswiecki et al proposed a method for in vivo simultaneous quantification of cartilage T_2 and apparent diffusion coefficients by modifying the spoiler gradient area and flip angle of the double echo steady state (DESS) sequence (78). Data acquired in phantoms and in vivo healthy knees at 3T showed good agreement with quantification using standard spin-echo sequences (78). Raya et al performed in vivo DTI of cartilage at 7T using line-scan techniques (79). The test–retest reproducibility was 8.1% for mean ADC and 9.7% for FA. Mean ADC and FA differed significantly ($P < 0.01$) between the OA and healthy populations, while T_2 did not in their study cohort (79), Figure 11. These studies demonstrated the feasibility of performing in vivo diffusion imaging in cartilage.

Diffusion MRI, in particular DTI, has the advantage that multi-components of the cartilage matrix including PG concentration and collagen network orientation and fraction can be quantified from one sequence. The major challenges for in vivo diffusion MRI of cartilage include the low SNR due to the short T_2 relaxation time of the tissue, requirement of high resolution due to small dimension of cartilage and the sensitivity of diffusion MRI to motion, and long acquisition time. Further studies are warranted to evaluate the reliability and reproducibility of in vivo diffusion parameter quantification and to evaluate its capability in diagnosing and monitoring cartilage degeneration.

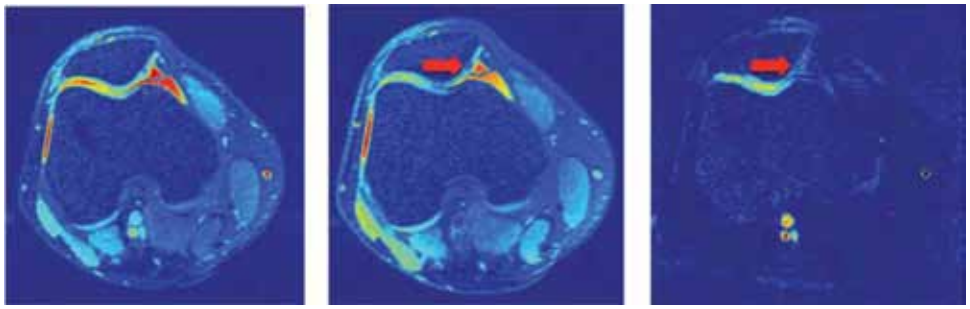

Figure 10. The gagCEST images of a human patella in vivo with irradiation at $\delta = -1.0$ ppm (left), $\delta = +1.0$ ppm (middle), and the difference image (right), displaying a clear demarcation of a cartilage lesion and GAG loss on the medial facet (indicated by arrows) (Figure reprinted from reference (73), with permission).

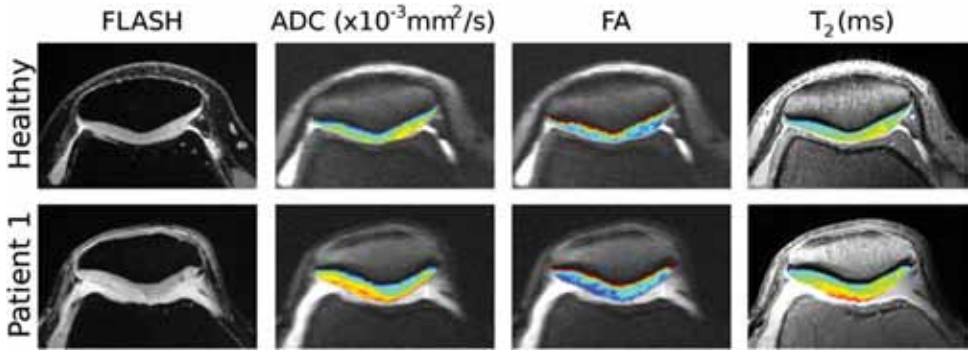

Figure 11. High-spatial-resolution morphologic MR images and MR imaging parameter maps (ADC, FA, and T2) in healthy volunteer (top row: 31-year-old man, right knee) and a subject with OA (bottom row: 60-year-old woman, Kellgren-Lawrence grade of 3) (Figure reprinted from reference (79), with permission).

Sodium Imaging

In addition to the proton MRI methods, sodium (^{23}Na) MRI has also been developed to evaluate cartilage matrix composition, in particular PG concentration, which was reviewed in detail by Borthakur et al (80). As discussed earlier, the GAG side chains of the PG are negatively charged, which concentrates cations including Na+ and K+ in the cartilaginous interstitial fluid. Based on the ideal Donnan theory, the fixed charge density (FCD), which is correlated with GAG concentration, can be estimated based on sodium content (81,82). Therefore, sodium can serve as an attractive natural endogenous contrast for PG evaluation.

Compared with proton MRI, sodium MRI, however, suffers from inherent low SNR due to (i) low concentrations in vivo (300 mM of ^{23}Na versus 50 M of ^{1}H in healthy cartilage); (ii) a four times lower gyromagnetic ratio (11.262 MHz/T of ^{23}Na versus 42.575 MHz/T for ^{1}H); and (iii) the ultra-short T_2 and T_2* relaxation times (short T_2 and T_2* component less than 2 ms, and long T_2 and T_2* component less than 15 ms). Thus, it is highly challenging to acquire in vivo sodium MR images with adequate SNR and spatial resolution under a clinically reasonable scan time. Higher static magnetic field strengths, dedicated coils and optimal pulse sequences are essential for in vivo sodium MRI.

The 3D gradient echo sequences have demonstrated the feasibility of sodium MRI of the human knee in vivo (80). However, these approaches are suboptimal as they required long TE values of 2–6.4 ms. Three dimensional projection imaging permits extremely short TE and has been implemented for sodium knee imaging either with twisted projection imaging (TPI, TE = 0.4 ms) (80), straight radial projections (TE = 0.16 ms) (83), or 3D cones (TE = 0.6 ms) (84). Nonselective hard RF pulses are also essential to achieve short TE in these 3D projection sequences. Using these techniques, normally at 3T and/or 7T, images can be acquired approximately within 15–30 min with a reasonable SNR and spatial resolution, Figure 12 (SNR 30 with nominal resolution 3.4 mm^3, scan time 14 min using a quadrature ^{23}Na coil at 7T (83); SNR~7 at 3T using a sodium-only coil and SNR~17 at 7T using a dual-tuned sodium/proton surface coil. Both 3T and 3 T measures had TE = 0.6 ms, nominal resolution 2 mm^3, scan time 26 min) (84).

In addition to the above efforts to reduce the TE to the lowest limit allowed by hardware, a recent study suggested an optimization of sodium SNR under SAR constraints with a shorter "steady-state" TR and smaller flip angles to take advantage of short sodium T_1 (~24 ms at 4T) (85). This shorter TR allowed more data averaging (although it meanwhile increased the TE due to SAR limit), which resulted in an approximately 30% SNR increase compared with "fully relaxed" parameters. At 4.7T, using this projection acquisition in the steady state (PASS) sequence, sodium images (TR/TE = 30/0.185 ms), with SNR 8–10 were acquired within 9 min (85).

Sodium content in cartilage measured by NMR and MRI was highly correlated with measures from inductively coupled plasma emission spectroscopy (ICP) (81) and standard dimethylmethylene blue PG assays (82), respectively. Using relaxation normalized calibration phantoms, sodium absolute concentration and then FCD were quantified. In trypsin-digested bovine cartilage, with over 20% PG depletion, sodium image signal change correlated significantly with the observed PG loss (80). Improved methods were suggested later to correct for B_1 inhomogeneity, as well as for T_1 and T_2* weighting during sodium quantification, and showed the feasibility of using sodium MRI to distinguish early degenerated cartilage using in vivo data from controls in vivo at 4.7T with a surface coil (80). At 7T, sodium concentrations were reduced significantly in OA subjects (n = 3) compared with controls (n = 5) by approximately 30–60%, depending on the degree of cartilage degeneration (83).

The major advantage of sodium MR imaging of cartilage is its high specificity to PG content without the need for any exogenous contrast. Moreover, the low sodium content (<50 mmol/L) of surrounding structures in the joint enables visualization of the cartilage with very high tissue contrast. However, sodium MRI is primarily limited by special hardware requirements and by inherently low sensitivity at the standard clinical field strength of 1.5T. With the increasing availability of scanners with high field strength (3T or higher), it may find more general applications.

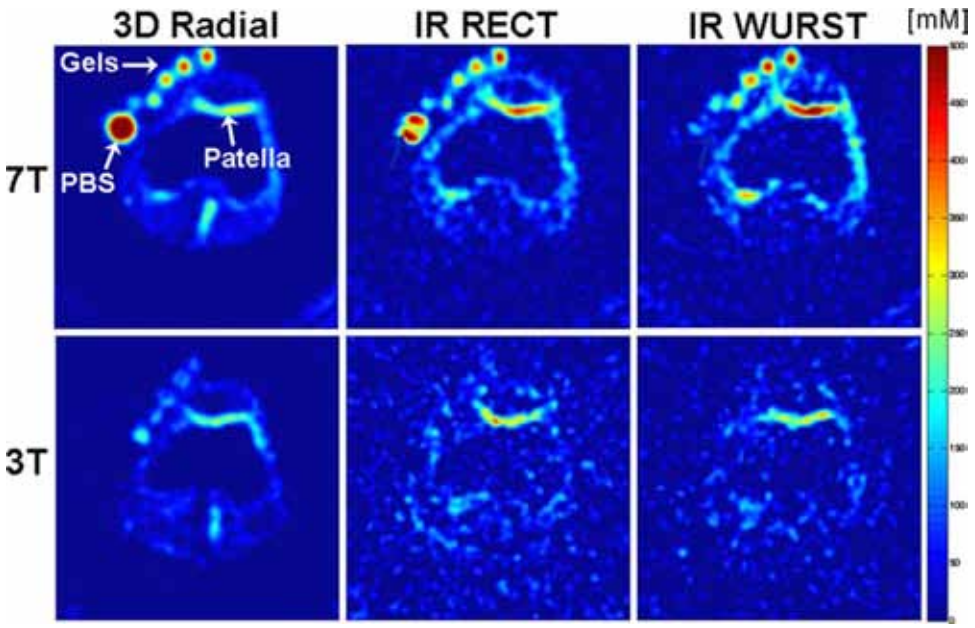

Figure 12. In vivo sodium imaging at 7T and 3T, respectively. 3T: 15,000 projections, RF 80°/0.5 ms, TR 80 ms, 2 mm isotropic resolution, time of acquisition (TA) 20 min; 7T: 10,000 projections, RF 90°/0.5 ms, TR 100 ms, 2 mm isotropic resolution, TA 17 min. IR RECT: 3D radial with the rectangular inversion; IR WURST: 3D radial with the adiabatic Wide-band Uniform Rate and Smooth Truncation (WURST) inversion pulse ("IR WURST" experiment). Images Courtesy of Dr. Ravinder Regatte. [Color figure can be viewed in the online issue, which is available at wileyonlinelibrary.com.]

Ultra Short Echo Imaging Methods

Sequences that acquire data with ultra-short or negligible time between excitation and data acquisition are designed to image tissue components with very short T_2 of a few milliseconds or less (86), which are otherwise "invisible" with conventional MR sequences. In addition to cortical bone and tendons, the ultra-short echo (UTE) methods have been applied to cartilage, menisci and vertebral disc, as reviewed by Bae et al (87). In cartilage, with the exception of the laminar splendens, the T_2 relaxation times decrease from the superficial zone to the deep zone as discussed previously. In the calcified zone close to the bone-cartilage interface, the T_2 relaxation times can be 10 ms or less. Changes within these regions may be important in early detection of cartilage degeneration.

The typical UTE sequences apply half excitation pulses, and data are acquired on the gradient ramp to keep a minimal TE, normally from a few microseconds (μs) to less than 100 μs. The data acquisition was developed with both 2D and 3D implementation, including 2D radial, twisted radial or spiral acquisition, and 3D projection reconstruction (3D PR), twisted projection imaging (TPI) and hybrid methods such as acquisition-weighted stack of spirals (87). Multiple techniques for long-T_2 component suppression in UTE were proposed to improve the contrast and visualization of short T_2 component, including dual echo acquisition with echo or scaled echo subtraction, methods based on RF pulses that selectively saturate or null long T_2-component for saturation and their modifications (86,88).

More recently, UTE sequences have been used for quantifying T_2* by Williams et al (89) and $T_{1\rho}$ by Du et al (90) in cartilage and other MSK tissues with short T_2 such as Achilles tendon and meniscus. The root-mean-square average coefficients of variation (RMSA-CV) of in vivo UTE-T_2* measures in cartilage was reported to be 8%, 6%, 16% for full-thickness, superficial and deep cMFC ROIs, corresponding to absolute errors (SD) of 1.2, 1.5, 1.5 ms, respectively (89). These sequences also have potential to quantify the relaxation times and the fractions of short and long water components in cartilage and other tissues.

REPAIR AND REGENERATION

MR methods especially those characterizing changes in the extra-cellular matrix play an important role in assessing cartilage repair (91). Microfracture is a frequently used technique for the repair of articular cartilage lesions of the knee, which is performed by inducing multiple penetrating injuries into the subchondral bone. Pluripotent mesenchymal progenitor cells migrate into the injury area, which subsequently form reparative fibrocartilage. Such generated fibrocartilage typically lacks stratification of hyaline cartilage matrix structure. In contrast, other techniques, including mosaicplasty, autologous chondrocyte transplantation (ACT) or matrix-associated autologous chondrocyte transplantation (MACT) are expected to generate more hyaline cartilage with stratification of matrix structure.

Marlovits et al developed a Magnetic Resonance Observation of Cartilage Repair Tissue (MOCART) classification system that defined nine variables to describe the morphology and signal intensity of the repair tissue compared with the adjacent native

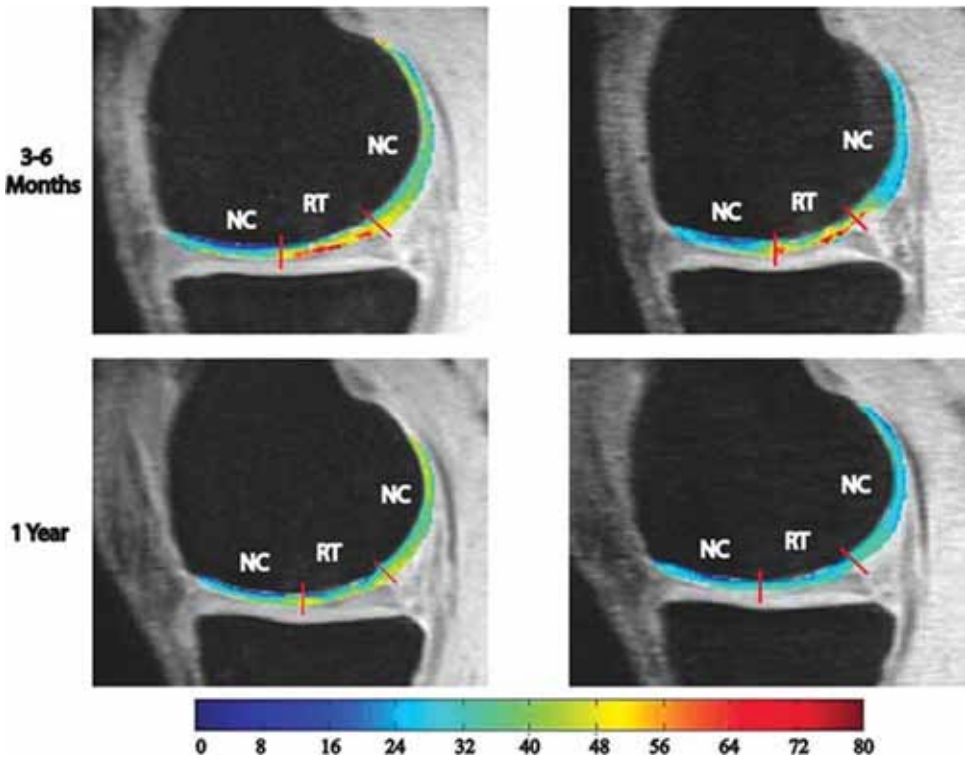

Figure 13. Representative $T_{1\rho}$ (left) and T_2 (right) maps 3–6 months and 1-year after microfracture (96). RT: repaired tissue; NC: normal cartilage. [Color figure can be viewed in the online issue, which is available at wileyonlinelibrary.com.]

cartilage. Excellent interobserver reproducibility of MOCART grading was reported and the gradings were correlated to clinical outcomes evaluated by visual analog score (VAS) and the knee injury and osteoarthritis outcome score (KOOS) in a 2-year longitudinal study (92).

In a prospective 2-year study in symptomatic patients with isolated full-thickness articular cartilage defects treated with the microfracture technique outcomes, clinical rating and MRI was combined. MRI showed good repair-tissue fill in the defect in 13 patients (54%), moderate fill in 7 (29%), and poor fill in 4 patients (17%) and correlated with the knee function scores (93). A multi-modal approach using T_2, diffusion weighted imaging and grading of MR images has been used for assessing postoperative cartilage. While grading did not show differences between the two repair techniques, microfracture therapy and MACT, T_2-mapping showed lower T_2 values after microfracture, and diffusion weighted imaging between healthy cartilage and cartilage repair tissue in both procedures (94). Mamisch et al (95) prospectively used T_2 cartilage maps to study the effect of unloading during the MR scan in the postoperative follow-up of patients after MACT of the knee joint. They demonstrated that T_2 values change with the time of unloading during the MR scan, and this difference was more pronounced in repair tissue. The difference between the repair and control tissue was also greater after longer unloading times, suggesting that assessment of cartilage repair is affected by the timing of the image acquisition relative to unloading the joint. A combined $T_{1\rho}$ and T_2 study examining repaired and the surrounding cartilage has demonstrated differences in cartilage after microfracture and mosaicplasty 3–6 months and after a year (96), Figure 13.

Articular cartilage has very limited intrinsic regenerative capacity, making cell-based therapy a possible approach for cartilage repair. Tissue engineered collagen matrix seeded with autogenous chondrocytes designed for the repair of hyaline articular cartilage have also been proposed and early studies combining MR grading and quantitative T_2 mapping have been used to assess the impact of such repair (97). In addition to fill efficacy the layered appearance or partial stratification of T_2 as a result of collagen orientation was detected in this study for 2 patients at 12 months and 4 patients at 24 months. Cell tracking can be a major step toward unraveling and improving the repair process of some of these therapies. Micrometer sized (MPIOs) and superparamagnetic iron oxides (SPIO) for labeling bone marrow-derived mesenchymal stem cells regarding effectivity, cell viability, long-term metabolic cell activity, chondrogenic differentiation has been studied (98,99). MPIO labeling results in efficient contrast uptake and signal loss that can be visualized and quantitatively characterized by means of MRI. SPGR imaging of implanted cells results in ex vivo detection within native tissue, and $T_{1\rho}$ imaging is unaffected by the presence of labeled cells immediately following implantation. MPIO labeling does not affect quantitative GAG production during chondrogenesis, but iron aggregation hinders extracellular matrix visualization (98). Similarly, SPIO labeling was effective and did not impair any of the

studied safety aspects, and injected and implanted SPIO-labeled cells can be accurately be visualized by MRI in a clinically relevant sized joint (100).

CONCLUSIONS

Quantitative MRI can provide noninvasive measurement of cartilage morphology as well as early changes within the matrix, which should be used concurrently for evaluating cartilage degeneration during OA. In particular, measures that detect early changes in the matrix may provide novel imaging markers for cartilage degeneration at early and potentially reversible stages. The most value of these advanced measures probably lies in evaluating subjects who are at early stages of the disease, and have a high risk of fast progression, such as those with obesity or with acute injuries. Such imaging markers will provide critical evaluation and monitoring for early intervention and prevention of the disease of OA. The quantitative MRI can be also effective in augmenting the longitudinal assessment of cohorts at risk for premature osteoarthritis, such as developmental dysplasia of the hip, femoroacetabular impingement, and patellofemoral dysmorphism.

While univariate analysis of each MR parameters discussed in this study demonstrated promising results, combing them using advanced statistical analysis method will provide multparametric evaluation and integrate information related with different aspects of the cartilage matrix, which has the potential to further improve our capability to distinguish degenerated cartilage from controls, as well as to monitor subtle changes after interventions.

Current advanced MRI methods for quantifying matrix changes normally require a long acquisition time and have a limited spatial resolution. Further technique development to increase the spatial resolution, the signal-to-noise ratio, and to reduce the acquisition time will facilitate translating these techniques into clinical applications.

Another critical issue for applying these advanced MRI techniques in clinical trial or studies is the standardization of the acquisition and postprocessing techniques. As discussed earlier, quantification variation can be caused by different scanner models, different sequence types and different postprocessing methodologies. The efforts of having standardized imaging and image processing protocols need to be synthesized between academic and industrial communities. More longitudinal and multicenter large-scale studies are warranted to evaluate the reliability (repeatability), validity, sensitivity, and specificity of advanced MRI measures as biomarkers for evaluating cartilage degeneration in OA.

REFERENCES

1. Dijkgraaf LC, de Bont LG, Boering G, Liem RS. The structure, biochemistry, and metabolism of osteoarthritic cartilage: a review of the literature. J Oral Maxillofac Surg 1995;53:1182–1192.
2. Goldring M, Goldring S. Osteoarthritis. J Cell Physiol 2007;213: 626–634.
3. Peterfy CG, Guermazi A, Zaim S, et al. Whole-Organ Magnetic Resonance Imaging Score (WORMS) of the knee in osteoarthritis. Osteoarthritis Cartilage 2004;12:177–190.
4. Hunter DJ, Lo GH, Gale D, Grainger AJ, Guermazi A, Conaghan PG. The reliability of a new scoring system for knee osteoarthritis MRI and the validity of bone marrow lesion assessment: BLOKS (Boston Leeds Osteoarthritis Knee Score). Ann Rheum Dis 2008; 67:206–211.
5. Eckstein F, Adam C, Sittek H, et al. Non-invasive determination of cartilage thickness throughout joint surfaces using magnetic resonance imaging. J Biomech 1997;30:285–289.
6. Stammberger T, Eckstein F, Michaelis M, Englmeier KH, Reiser M. Interobserver reproducibility of quantitative cartilage measurements: comparison of B-spline snakes and manual segmentation. Magn Reson Imaging 1999;17:1033–1042.
7. Lynch JA, Zaim S, Zhao J, Stork A, Peterfy CG, Genant HK, editors. Cartilage segmentation of 3D MRI scans of the osteoarthritic knee combining user knowledge and active contours. SPIE, Medical Imaging; 2000; San Diego, CA.
8. Grau V, Mewes AU, Alcaniz M, Kikinis R, Warfield SK. Improved watershed transform for medical image segmentation using prior information. IEEE Trans Med Imaging 2004;23:447–458.
9. Pakin SK, Tamez-Pena JG, Totterman S, Parker KJ, editors. Segmentation, surface extraction, and thickness computation of articular cartilage. SPIE, Medical Imaging; 2002; San Diego, CA.
10. Warfield SK, Kaus M, Jolesz FA, Kikinis R. Adaptive, template moderated, spatially varying statistical classification. Med Image Anal 2000;4:43–55.
11. Carballido-Gamio J, Bauer JS, Stahl R, et al. Inter-subject comparison of MRI knee cartilage thickness. Med Image Anal 2008; 12:120–135.
12. Ateshian GA, Soslowsky LJ, Mow VC. Quantitation of articular surface topography and cartilage thickness in knee joints using stereophotogrammetry. J Biomech 1991;24:761–776.
13. Pelletier JP, Raynauld JP, Berthiaume MJ, et al. Risk factors associated with the loss of cartilage volume on weight-bearing areas in knee osteoarthritis patients assessed by quantitative magnetic resonance imaging: a longitudinal study. Arthritis Res Ther 2007;9:R74.
14. Carballido-Gamio J, Link T, Majumdar S. New techniques for cartilage magnetic resonance imaging relaxation time analysis: texture analysis of flattened cartilage and localized intra- and inter-subject comparisons. Magn Reson Med 2008;59:1472–1477.
15. Cohen ZA, Mow VC, Henry JH, Levine WN, Ateshian GA. Templates of the cartilage layers of the patellofemoral joint and their use in the assessment of osteoarthritic cartilage damage. Osteoarthritis Cartilage 2003;11:569–579.
16. Eckstein F, Wirth W, Nevitt MC. Recent advances in osteoarthritis imaging-the Osteoarthritis Initiative. Nat Rev Rheumatol 2012;8: 622–630.
17. Mankin HJ, Thrasher AZ. Water content and binding in normal and osteoarthritic human cartilage. J Bone Joint Surg Am 1975; 57:76–80.
18. Bashir A, Gray ML, Burstein D. Gd-DTPA2- as a measure of cartilage degradation. Magn Reson Med 1996;36:665–673.
19. Gray ML, Burstein D, Kim YJ, Maroudas A. 2007 Elizabeth Winston Lanier Award Winner. Magnetic resonance imaging of cartilage glycosaminoglycan: basic principles, imaging technique, and clinical applications. J Orthop Res 2008;26:281–291.
20. Siversson C, Tiderius CJ, Neuman P, Dahlberg L, Svensson J. Repeatability of T1-quantification in dGEMRIC for three different acquisition techniques: two-dimensional inversion recovery, three-dimensional look locker, and three-dimensional variable flip angle. J Magn Reson Imaging 2010;31:1203–1209.
21. Burstein D, Velyvis J, Scott KT, et al. Protocol issues for delayed Gd(DTPA)(2-)-enhanced MRI (dGEMRIC) for clinical evaluation of articular cartilage. Magn Reson Med 2001;45:36–41.
22. Williams A, Sharma L, McKenzie CA, Prasad PV, Burstein D. Delayed gadolinium-enhanced magnetic resonance imaging of cartilage in knee osteoarthritis: findings at different radiographic stages of disease and relationship to malalignment. Arthritis Rheum 2005;52:3528–3535.
23. Anandacoomarasamy A, Giuffre BM, Leibman S, et al. Delayed gadolinium-enhanced magnetic resonance imaging of cartilage:

clinical associations in obese adults. J Rheumatol 2009;36:1056–1062.
24. Ericsson YB, Tjornstrand J, Tiderius CJ, Dahlberg LE. Relationship between cartilage glycosaminoglycan content (assessed with dGEMRIC) and OA risk factors in meniscectomized patients. Osteoarthritis Cartilage 2009;17:565–570.
25. Tiderius CJ, Olsson LE, Nyquist F, Dahlberg L. Cartilage glycosaminoglycan loss in the acute phase after an anterior cruciate ligament injury: delayed gadolinium-enhanced magnetic resonance imaging of cartilage and synovial fluid analysis. Arthritis Rheum 2005;52:120–127.
26. Fleming BC, Oksendahl HL, Mehan WA, et al. Delayed Gadolinium-Enhanced MR Imaging of Cartilage (dGEMRIC) following ACL injury. Osteoarthritis Cartilage 2010;18:662–667.
27. Mamisch TC, Kain MS, Bittersohl B, et al. Delayed gadolinium-enhanced magnetic resonance imaging of cartilage (dGEMRIC) in Femoacetabular impingement. J Orthop Res 2011;29:1305–1311.
28. Jessel RH, Zilkens C, Tiderius C, Dudda M, Mamisch TC, Kim YJ. Assessment of osteoarthritis in hips with femoroacetabular impingement using delayed gadolinium enhanced MRI of cartilage. J Magn Reson Imaging 2009;30:1110–1115.
29. Kim YJ, Jaramillo D, Millis MB, Gray ML, Burstein D. Assessment of early osteoarthritis in hip dysplasia with delayed gadolinium-enhanced magnetic resonance imaging of cartilage. J Bone Joint Surg Am 2003;85:1987–1992.
30. Pai A, Li X, Majumdar S. A comparative study at 3 T of sequence dependence of T2 quantitation in the knee. Magn Reson Imaging 2008;26:1215–1220.
31. Regatte RR, Akella SV, Borthakur A, Kneeland JB, Reddy R. Proteoglycan depletion-induced changes in transverse relaxation maps of cartilage: comparison of T2 and T1rho. Acad Radiol 2002;9:1388–1394.
32. Xia Y. Relaxation anisotropy in cartilage by NMR microscopy (muMRI) at 14-microm resolution. Magn Reson Med 1998;39:941–949.
33. Nieminen MT, Rieppo J, Toyras J, et al. T2 relaxation reveals spatial collagen architecture in articular cartilage: a comparative quantitative MRI and polarized light microscopic study. Magn Reson Med 2001;46:487–493.
34. Reiter DA, Roque RA, Lin PC, Doty SB, Pleshko N, Spencer RG. Improved specificity of cartilage matrix evaluation using multiexponential transverse relaxation analysis applied to pathomimetically degraded cartilage. NMR Biomed 2011;24:1286–1294.
35. Wang N, Xia Y. Dependencies of multi-component T2 and T1rho relaxation on the anisotropy of collagen fibrils in bovine nasal cartilage. J Magn Reson 2011;212:124–132.
36. Dardzinski BJ, Mosher TJ, Li S, Van Slyke MA, Smith MB. Spatial variation of T2 in human articular cartilage. Radiology 1997;205:546–550.
37. Li X, Pai A, Blumenkrantz G, et al. Spatial distribution and relationship of T1rho and T2 relaxation times in knee cartilage with osteoarthritis. Magn Reson Med 2009;61:1310–1318.
38. Mosher T, Liu Y, Yang Q, et al. Age dependency of cartilage magnetic resonance imaging T2 relaxation times in asymptomatic women. Arthritis Rheum 2004;50:2820–2828.
39. Mosher TJ, Collins CM, Smith HE, et al. Effect of gender on in vivo cartilage magnetic resonance imaging T2 mapping. J Magn Reson Imaging 2004;19:323–328.
40. Li X, Ma C, Link T, et al. In vivo T1rho and T2 mapping of articular cartilage in osteoarthritis of the knee using 3 Tesla MRI. Osteoarthritis and Cartilage 2007;15:789–797.
41. Koff MF, Amrami KK, Kaufman KR. Clinical evaluation of T2 values of patellar cartilage in patients with osteoarthritis. Osteoarthritis Cartilage 2007;15:198–204.
42. Bolbos R, Zuo J, Banerjee S, et al. Relationship between trabecular bone structure and articular cartilage morphology and relaxation times in early OA of the knee joint using parallel MRI at 3 T. Osteoarthritis Cartilage 2008;16:1150–1159.
43. Lammentausta E, Kiviranta P, Toyras J, et al. Quantitative MRI of parallel changes of articular cartilage and underlying trabecular bone in degeneration. Osteoarthritis Cartilage 2007;15:1149–1157.
44. Mosher TJ, Liu Y, Torok CM. Functional cartilage MRI T2 mapping: evaluating the effect of age and training on knee cartilage response to running. Osteoarthritis Cartilage 2010;18:358–364.
45. Subburaj K, Kumar D, Souza RB, et al. The Acute Effect of Running on Knee Articular Cartilage and Meniscus Magnetic Resonance Relaxation Times in Young Healthy Adults. Am J Sports Med 2012;9:2134–2141.
46. Potter HG, Jain SK, Ma Y, Black BR, Fung S, Lyman S. Cartilage injury after acute, isolated anterior cruciate ligament tear: immediate and longitudinal effect with clinical/MRI follow-up. Am J Sports Med 2012;40:276–285.
47. Schneider E, NessAiver M, White D, et al. The osteoarthritis initiative (OAI) magnetic resonance imaging quality assurance methods and results. Osteoarthritis Cartilage 2008;16:994–1004.
48. Hovis KK, Stehling C, Souza RB, et al. Physical activity is associated with magnetic resonance imaging-based knee cartilage T2 measurements in asymptomatic subjects with and those without osteoarthritis risk factors. Arthritis Rheum 2011;63:2248–2256.
49. Pan J, Pialat JB, Joseph T, et al. Knee cartilage T2 characteristics and evolution in relation to morphologic abnormalities detected at 3-T MR imaging: a longitudinal study of the normal control cohort from the osteoarthritis initiative. Radiology 2011;261:507–515.
50. Joseph GB, Baum T, Alizai H, et al. Baseline mean and heterogeneity of MR cartilage T(2) are associated with morphologic degeneration of cartilage, meniscus, and bone marrow over 3 years - data from the Osteoarthritis Initiative. Osteoarthritis Cartilage 2012;20:727–735.
51. Li X, Han E, Busse R, Majumdar S. In vivo T1rho mapping in cartilage using 3D magnetization-prepared angle-modulated partitioned k-space spoiled gradient echo snapshots (3D MAPSS). Magn Reson Med 2008;59:298–307.
52. Witschey W, Borthakur A, Elliott M, et al. T1rho-prepared balanced gradient echo for rapid 3D T1rho MRI. J Magn Reson Imaging 2008;28:744–754.
53. Regatte RR, Akella SV, Wheaton AJ, et al. 3D-T1rho-relaxation mapping of articular cartilage: in vivo assessment of early degenerative changes in symptomatic osteoarthritic subjects. Acad Radiol 2004;11:741–749.
54. Charagundla SR, Borthakur A, Leigh JS, Reddy R. Artifacts in T(1rho)-weighted imaging: correction with a self-compensating spin-locking pulse. J Magn Reson 2003;162:113–121.
55. Chen W, Takahashi A, Han E. Quantitative T(1)(rho) imaging using phase cycling for B0 and B1 field inhomogeneity compensation. Magn Reson Imaging 2011;29:608–619.
56. Li X, Cheng J, Lin K, et al. Quantitative MRI using T1rho and T2 in human osteoarthritic cartilage specimens: correlation with biochemical measurements and histology. Magn Reson Imaging 2011;29:324–334.
57. Akella SV, Regatte RR, Wheaton AJ, Borthakur A, Reddy R. Reduction of residual dipolar interaction in cartilage by spin-lock technique. Magn Reson Med 2004;52:1103–1109.
58. Duvvuri U, Goldberg AD, Kranz JK, et al. Water magnetic relaxation dispersion in biological systems: the contribution of proton exchange and implications for the noninvasive detection of cartilage degradation. Proc Natl Acad Sci U S A 2001;98:12479–12484.
59. Mlynarik V, Szomolanyi P, Toffanin R, Vittur F, Trattnig S. Transverse relaxation mechanisms in articular cartilage. J Magn Reson 2004;169:300–307.
60. Kettunen M, Grohn O, Silvennoinen M, Penttonen M, Kauppinen R. Effects of intracellular pH, blood, and tissue oxygen tension on T1rho relaxation in rat brain. Magn Reson Med 2002;48:470–477.
61. Mosher TJ, Zhang Z, Reddy R, et al. Knee articular cartilage damage in osteoarthritis: analysis of MR image biomarker reproducibility in ACRIN-PA 4001 multicenter trial. Radiology 2011;258:832–842.
62. Stahl R, Luke A, Li X, et al. T1rho, T2 and focal knee cartilage abnormalities in physically active and sedentary healthy subjects versus early OA patients--a 3.0-Tesla MRI study. Eur Radiol 2009;19:132–143.
63. Zarins ZA, Bolbos RI, Pialat JB, et al. Cartilage and meniscus assessment using T1rho and T2 measurements in healthy subjects and patients with osteoarthritis. Osteoarthritis Cartilage 2010;18:1408–1416.
64. Li X, Ma C, Bolbos R, et al. Quantitative assessment of bone marrow edema pattern and overlying cartilage in knees with

osteoarthritis and anterior cruciate ligament tear using MR imaging and spectroscopic imaging. J Magn Reson Imaging 2008;28: 453–461.
65. Li X, Kuo D, Theologis A, et al. Cartilage in anterior cruciate ligament-reconstructed knees: MR imaging T1{rho} and T2--initial experience with 1-year follow-up. Radiology 2011;258:505–514.
66. Henkelman RM, Stanisz GJ, Graham SJ. Magnetization transfer in MRI: a review. NMR Biomed 2001;14:57–64.
67. Kim DK, Ceckler TL, Hascall VC, Calabro A, Balaban RS. Analysis of water-macromolecule proton magnetization transfer in articular cartilage. Magn Reson Med 1993;29:211–215.
68. Gray ML, Burstein D, Lesperance LM, Gehrke L. Magnetization transfer in cartilage and its constituent macromolecules. Magn Reson Med 1995;34:319–325.
69. Henkelman RM, Huang X, Xiang QS, Stanisz GJ, Swanson SD, Bronskill MJ. Quantitative interpretation of magnetization transfer. Magn Reson Med 1993;29:759–766.
70. Sled JG, Pike GB. Quantitative imaging of magnetization transfer exchange and relaxation properties in vivo using MRI. Magn Reson Med 2001;46:923–931.
71. Stikov N, Keenan KE, Pauly JM, Smith RL, Dougherty RF, Gold GE. Cross-relaxation imaging of human articular cartilage. Magn Reson Med 2011;66:725–734.
72. van Zijl PC, Yadav NN. Chemical exchange saturation transfer (CEST): what is in a name and what isn't? Magn Reson Med 2011;65:927–948.
73. Ling W, Regatte RR, Navon G, Jerschow A. Assessment of glycosaminoglycan concentration in vivo by chemical exchange-dependent saturation transfer (gagCEST). Proc Natl Acad Sci U S A 2008;105:2266–2270.
74. Schmitt B, Zbyn S, Stelzeneder D, et al. Cartilage quality assessment by using glycosaminoglycan chemical exchange saturation transfer and (23)Na MR imaging at 7 T. Radiology 2011;260:257–264.
75. Deng X, Farley M, Nieminen MT, Gray M, Burstein D. Diffusion tensor imaging of native and degenerated human articular cartilage. Magn Reson Imaging 2007;25:168–171.
76. de Visser SK, Bowden JC, Wentrup-Byrne E, et al. Anisotropy of collagen fibre alignment in bovine cartilage: comparison of polarised light microscopy and spatially resolved diffusion-tensor measurements. Osteoarthritis Cartilage 2008;16:689–697.
77. Raya JG, Arnoldi AP, Weber DL, et al. Ultra-high field diffusion tensor imaging of articular cartilage correlated with histology and scanning electron microscopy. MAGMA 2011;24:247–258.
78. Staroswiecki E, Granlund KL, Alley MT, Gold GE, Hargreaves BA. Simultaneous estimation of T(2) and apparent diffusion coefficient in human articular cartilage in vivo with a modified three-dimensional double echo steady state (DESS) sequence at 3 T. Magn Reson Med 2012;67:1086–1096.
79. Raya JG, Horng A, Dietrich O, et al. Articular cartilage: in vivo diffusion-tensor imaging. Radiology 2012;262:550–559.
80. Borthakur A, Mellon E, Niyogi S, Witschey W, Kneeland J, Reddy R. Sodium and T1rho MRI for molecular and diagnostic imaging of articular cartilage. NMR Biomed 2006;19:781–821.
81. Lesperance LM, Gray ML, Burstein D. Determination of fixed charge density in cartilage using nuclear magnetic resonance. J Orthop Res 1992;10:1–13.
82. Shapiro EM, Borthakur A, Gougoutas A, Reddy R. 23Na MRI accurately measures fixed charge density in articular cartilage. Magn Reson Med 2002;47:284–291.
83. Wang L, Wu Y, Chang G, et al. Rapid isotropic 3D-sodium MRI of the knee joint in vivo at 7T. J Magn Reson Imaging 2009;30:606–614.
84. Staroswiecki E, Bangerter NK, Gurney PT, Grafendorfer T, Gold GE, Hargreaves BA. In vivo sodium imaging of human patellar cartilage with a 3D cones sequence at 3 T and 7 T. J Magn Reson Imaging 2010;32:446–451.
85. Watts A, Stobbe RW, Beaulieu C. Signal-to-noise optimization for sodium MRI of the human knee at 4.7 Tesla using steady state. Magn Reson Med 2011;66:697–705.
86. Gatehouse PD, Bydder GM. Magnetic resonance imaging of short T2 components in tissue. Clin Radiol 2003;58:1–19.
87. Bae WC, Du J, Bydder GM, Chung CB. Conventional and ultrashort time-to-echo magnetic resonance imaging of articular cartilage, meniscus, and intervertebral disk. Top Magn Reson Imaging 2010;21:275–289.
88. Du J, Takahashi AM, Bae WC, Chung CB, Bydder GM. Dual inversion recovery, ultrashort echo time (DIR UTE) imaging: creating high contrast for short-T(2) species. Magn Reson Med 2010; 63:447–455.
89. Williams A, Qian Y, Chu CR. UTE-T2 * mapping of human articular cartilage in vivo: a repeatability assessment. Osteoarthritis Cartilage 2011;19:84–88.
90. Du J, Carl M, Diaz E, et al. Ultrashort TE T1rho (UTE T1rho) imaging of the Achilles tendon and meniscus. Magn Reson Med 2010;64:834–842.
91. Trattnig S, Winalski CS, Marlovits S, Jurvelin JS, Welsch G, Potter HG. Magnetic resonance imaging of cartilage repair: a review. Cartilage 2011;2:5–26.
92. Marlovits S, Singer P, Zeller P, Mandl I, Haller J, Trattnig S. Magnetic resonance observation of cartilage repair tissue (MOCART) for the evaluation of autologous chondrocyte transplantation: determination of interobserver variability and correlation to clinical outcome after 2 years. Eur J Radiol 2006;57:16–23.
93. Mithoefer K, Williams RJ III, Warren RF, et al. Chondral resurfacing of articular cartilage defects in the knee with the microfracture technique. Surgical technique. J Bone Joint Surg Am 2006; 88(Suppl 1 Pt 2):294–304.
94. Welsch GH, Trattnig S, Domayer S, Marlovits S, White LM, Mamisch TC. Multimodal approach in the use of clinical scoring, morphological MRI and biochemical T2-mapping and diffusion-weighted imaging in their ability to assess differences between cartilage repair tissue after microfracture therapy and matrix-associated autologous chondrocyte transplantation: a pilot study. Osteoarthritis Cartilage 2009;17:1219–1227.
95. Mamisch TC, Trattnig S, Quirbach S, Marlovits S, White LM, Welsch GH. Quantitative T2 mapping of knee cartilage: differentiation of healthy control cartilage and cartilage repair tissue in the knee with unloading--initial results. Radiology 2010;254:818–826.
96. Holtzman DJ, Theologis AA, Carballido-Gamio J, Majumdar S, Li X, Benjamin C. T(1rho) and T(2) quantitative magnetic resonance imaging analysis of cartilage regeneration following microfracture and mosaicplasty cartilage resurfacing procedures. J Magn Reson Imaging 2010;32:914–923.
97. Crawford DC, Heveran CM, Cannon WD Jr, Foo LF, Potter HG. An autologous cartilage tissue implant NeoCart for treatment of grade III chondral injury to the distal femur: prospective clinical safety trial at 2 years. Am J Sports Med 2009;37:1334–1343.
98. Saldanha KJ, Doan RP, Ainslie KM, Desai TA, Majumdar S. Micrometer-sized iron oxide particle labeling of mesenchymal stem cells for magnetic resonance imaging-based monitoring of cartilage tissue engineering. Magn Reson Imaging 2011;29:40–49.
99. Majumdar S, Li X, Blumenkrantz G, et al. MR imaging and early cartilage degeneration and strategies for monitoring regeneration. J Musculoskelet Neuronal Interact 2006;6:382–384.
100. van Buul GM, Kotek G, Wielopolski PA, et al. Clinically translatable cell tracking and quantification by MRI in cartilage repair using superparamagnetic iron oxides. PLoS One 2011;6: e17001.

MRI of Knee Ligament Injury and Reconstruction

Nadja A. Farshad-Amacker, M.D. and Hollis G. Potter, M.D.*

Reprinted from the ISMRM Journal of Magnetic Resonance Imaging: Volume 38: Pages: 757-773, © 2013 from Wiley Periodicals, Inc.

This article is accredited as a journal-based CME activity. If you wish to receive credit for this activity, please refer to the website: www.wileyhealthlearning.com

ACCREDITATION AND DESIGNATION STATEMENT

Blackwell Futura Media Services designates this journal-based CME activity for a maximum of 1 *AMA PRA Category 1 Credit*™. Physicians should only claim credit commensurate with the extent of their participation in the activity.

Blackwell Futura Media Services is accredited by the Accreditation Council for Continuing Medical Education to provide continuing medical education for physicians.

EDUCATIONAL OBJECTIVES

Upon completion of this educational activity, participants will be better able to define appropriate indications for MRI in the evaluation of patients with suspected pulmonary embolism, potential aortic dissection, or myocardial ischemia; and summarize the evidence supporting the use of MRI in the evaluation of patients with suspected pulmonary embolism, potential aortic dissection, or myocardial ischemia.

ACTIVITY DISCLOSURES

No commercial support has been accepted related to the development or publication of this activity.

Faculty Disclosures:

Editor-in-Chief: C. Leon Partain, MD, PhD has no conflicts of interest to disclose.

CME Editor: Scott B. Reeder, MD, PhD has no conflicts of interest to disclose.

CME Committee: Pratik Mukherjee, MD, PhD, Shreyas Vasanawala, MD, PhD, Bonnie Joe, MD, PhD, Tim Leiner, MD, PhD, Sabine Weckbach, MD, and Frank Korosec, PhD have no conflicts of interest to disclose. Scott K. Nagle, MD, PhD discloses a personal shareholder investment in GE. Mustafa R. Bashir, MD discloses research support from Bracco Diagnostics and Siemens Healthcare, and consultant honorarium from Bayer Pharmaceuticals.

Authors: Nadja A. Farshad-Amacker, MD, Hollis G. Potter, MD, have nothing to disclose. Scott K. Nagle, MD, PhD, discloses a personal shareholder investment in GE.

This manuscript underwent peer review in line with the standards of editorial integrity and publication ethics maintained by *Journal of Magnetic Resonance Imaging*. The peer reviewers have no relevant financial relationships. The peer review process for *Journal of Magnetic Resonance Imaging* is double-blinded. As such, the identities of the reviewers are not disclosed in line with the standard accepted practices of medical journal peer review.

Conflicts of interest have been identified and resolved in accordance with Blackwell Futura Media Services's Policy on Activity Disclosure and Conflict of Interest. No relevant financial relationships exist for any individual in control of the content and therefore there were no conflicts to resolve.

INSTRUCTIONS ON RECEIVING CREDIT

For information on applicability and acceptance of CME credit for this activity, please consult your professional licensing board.

This activity is designed to be completed within an hour; physicians should claim only those credits that reflect the time actually spent in the activity. To successfully earn credit, participants must complete the activity during the valid credit period.

Follow these steps to earn credit:

- Log on to www.wileyhealthlearning.com
- Read the target audience, educational objectives, and activity disclosures.
- Read the article in print or online format.
- Reflect on the article.
- Access the CME Exam, and choose the best answer to each question.
- Complete the required evaluation component of the activity.

This activity will be available for CME credit for twelve months following its publication date. At that time, it will be reviewed and potentially updated and extended for an additional period.

The MRI Research Laboratory, Department of Radiology and Imaging, Hospital for Special Surgery, New York, New York, USA.

*Address reprint requests to: H.G.P., MRI Department, Hospital for Special Surgery, 535 East 70th Street, New York, NY 10021. E-mail: potterh@hss.edu

Received December 14, 2012; Accepted June 19, 2013.

DOI 10.1002/jmri.24311

View this article online at wileyonlinelibrary.com.

Knee ligament instability may lead to meniscal and chondral damage, resulting in early osteoarthritis. Due to its superior soft tissue contrast and avoidance of harmful ionizing radiation, MRI has become the most important imaging modality for early recognition of structural defects of the knee joint. This review aims to the understanding of MRI appearances of knee ligament structures associated with knee instability, and to review the common patterns of altered knee mechanics that lead to ligament failure. Normal anatomy of the knee ligaments, pathologic conditions, and postsurgical appearances of the anterior cruciate ligament, posterior cruciate ligament, medial collateral ligament, and posterolateral corner are described.

Keywords: MRI; ligament; instability; knee; anterior cruciate liagment; posterior cruciate ligament
J. Magn. Reson. Imaging 2013;38:757–773.

KNEE INSTABILITY can occur if one or more of the major ligaments are disrupted. The key structures, which contribute to its stability, are the anterior cruciate ligament (ACL), the posterior cruciate ligament (PCL), the medial collateral ligament (MCL), and the posterolateral corner complex (PLC). Knee instability has been identified as a risk factor for meniscal and chondral damage, resulting in early osteoarthritis; therefore, early recognition and treatment is important (1,2). MRI has become the most useful imaging modality due to its superior soft tissue contrast, lack of ionizing radiation and multiplanar capabilities. This review aims to provide a summary of current evidence and standards regarding MRI of structures related to the static stabilizers of the knee.

ANTERIOR CRUCIATE LIGAMENT

Anatomy and Normal ACL Appearance

The ACL originates from the posteromedial aspect of the femoral condyle and consists of two distinct anatomic components based on their insertion at the tibia: an anteromedial band (AMB) and a posterolateral band (PLB) (3–5). The ACL is composed primarily of longitudinally oriented collagen type I fibers (3,4,6) and is surrounded by synovium (3–5). Its main vascular supply is by the middle geniculate artery with additional supply from the inferior medial and lateral geniculate arteries (4). Biomechanically, the ACL is the primary stabilizer to anterior tibial displacement. The AMB becomes tight in flexion and the PLB at extension. Therefore, a failure of the AMB results in anterior instability whereas failure of the PLB results in rotational instability (7), which may be provoked in pivoting sports such as soccer or basketball. Increased signal surrounding and between the bundles of the ACL on short echo time (TE) MR images is considered normal and reflects the orientation of the fascicles to the static magnetic field as well as adjacent fat surrounding the ligament.

ACL Tears

The ACL is the most common injured ligament with approximately 3000 per year in United States and approximately 200,000 ACL reconstructions performed (8). The ACL is most commonly affected in hyperextension injuries, as seen in competitive downhill skiers or football players but also may secondarily tear following valgus loads after primary MCL failure as in the intermediate skier that traverses the slope and sustains a primary valgus moment (Table 1). MRI is the most noninvasive method for diagnosing ACL tears with a sensitivity of 87–94%, specificity of 50–100%, and accuracy of 91–95% (9–11). Most ACL tears occur in the middle portion of the ligament, less frequently at the femoral or tibial attachment (12,13).

Acute Complete ACL Tears

Direct signs of acute, complete ACL tear are (a) complete discontinuity of fibers or (b) irregular contour

Table 1
Location of Bone Marrow Edema and Injured Ligamentous Structures According to the Injury Pattern

Altered mechanics	Example	Location of bone marrow edema pattern		Injury suspected
		Femoral side	Tibial side	
Pivot shift (valgus stress and internal rotation of femur)	Intermediate skier traversing the slope, basketball/football injury	Midportion lateral (above anterior horn lateral meniscus)	Posterolateral	• ACL • MCL/Segond fracture • Posterior joint capsule • Meniscus (posterior medial>lateral)
Hyperflexion (force against anterior tibia with flexed knee)	Motor vehicle dashboard injury	Anteromedial	Anterior tibia (direct trauma)	• PCL • Posterior joint capsule
Hyperextension	Downhill skier with force directed down the slope, soccer player	Anterior	Anteromedial	• ACL • PCL (less common) • Posterior capsule • PLC (with varus) • MCL, PMC (with valgus)
Clip/valgus stress (valgus stress in mild flexion)	Direct blow (football; soccer)	Lateral>medial	None	• MCL (proximal>distal) • ACL • Meniscal injury

ACL, anterior cruciate ligament; MCL, medial collateral ligament; PCL, posterior cruciate ligament; PLC, posterolateral corner; PMC, posteromedial corner.

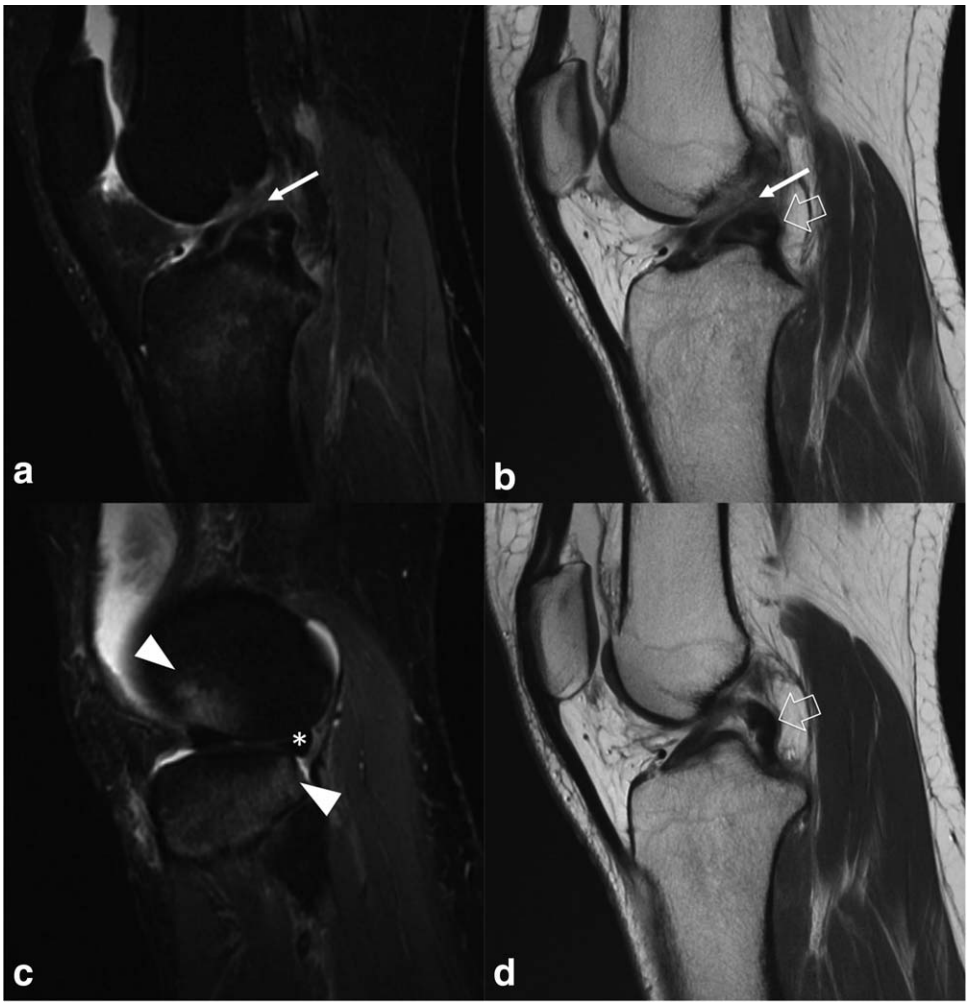

Figure 1. Complete ACL tear in a 15-year-old patient. Sagittal **(a,c)** T2-weighted fat saturated fast spin-echo and **(b,d)** proton density-weighted fast spin-echo images show complete, acute ACL rupture (arrows) in the middle portion of the ligament with transchondral fractures (arrowheads) in the lateral femoral condyle and the lateral tibial plateau as well as buckling of the PCL (open arrow) and undercovering of the posterior horn of the lateral meniscus (*) as secondary signs.

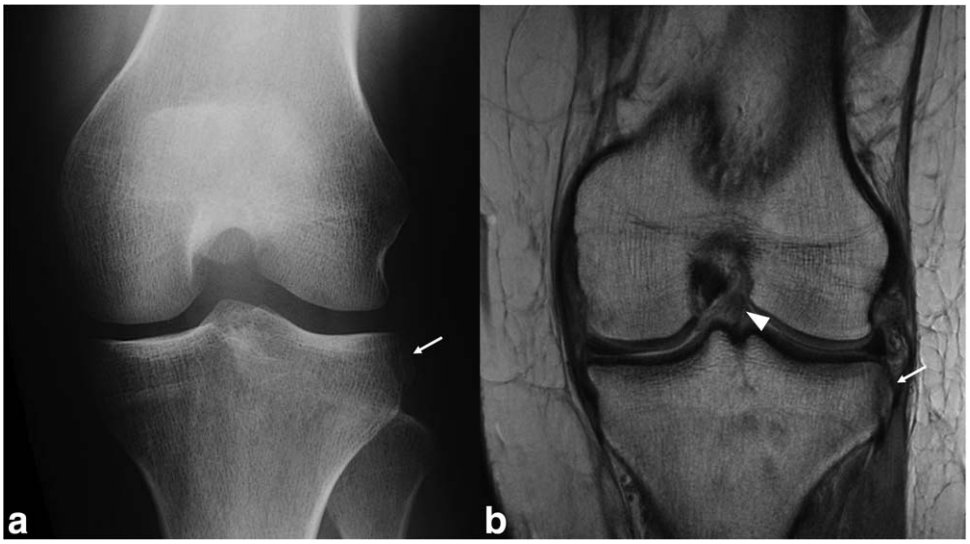

Figure 2. A Segond fracture (arrows), associated with a complete ACL tear (arrowhead) in a 26-year-old patient is shown on **(a)** radiograph and **(b)** a coronal proton density-weighted fast spin-echo.

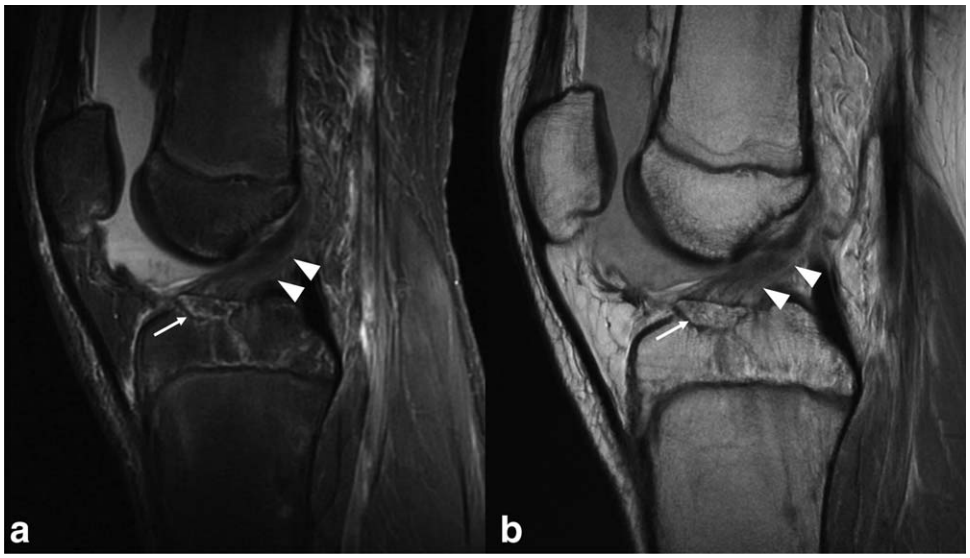

Figure 3. Avulsion fracture of the ACL in a 16-year-old patient. Sagittal **(a)** T2-weighted fat saturated fast spin-echo and **(b)** proton density-weighted fast spin-echo MR images show the avulsion fragment (arrows) at the intercondylar eminence of the tibia. Note thickened, diffusely hyperintense ACL (arrowheads).

with increased signal intensity on water sensitive sequences (13,14) (Fig. 1). Several secondary signs of complete ACL tear have been described with a low sensitivity (34–90%) but a high specificity (91–100%) and, therefore, can be a helpful hint to the diagnosis of ACL tear. The most useful secondary signs are the PCL buckle (Fig. 1), an "uncovering" posterior horn of the lateral meniscus (Fig. 1), the entire lateral collateral ligament (LCL) seen on one coronal image, translational bone contusion in the lateral compartment (Fig. 1), anterior displacement of the tibia (more than 5–7 mm, more pronounced laterally), lateral femoral sulcus (deeper than 1.5 mm), and the posterior PCL line, which is a line drawn parallel to the posterior margin of the distal portion of the PCL and extended proximally (15–19). A PCL line is considered positive if it does not intersect with the medullary cavity of the femur (20). Furthermore, hemarthrosis is often associated with ACL rupture (21,22). It should be noted that the presence of the translational bone marrow edema pattern created by the pivot shift is indicative of recent tibial translation (Table 1) but not the presence of an acute ACL, as these injuries may be seen in the setting of chronic ACL insufficiency.

Furthermore, ACL tears are often associated with injury to additional structures, such as the MCL, meniscal tears, and Segond fractures, an avulsion fracture at the lateral capsular insertion of the tibia, which is found in 6–13% of ACL rupture (23) (Fig. 2). Avulsions fractures of the tibial eminence may occur, mostly noted in children (24). Note should be made that acute eminence avulsions are associated with interstitial load imparted to the ligament before bony failure; thus, the ligament is not entirely "normal" in the setting of a primary footprint avulsion (Fig. 3).

Acute Partial ACL Tears

Partial ACL tears are common (ranges from 20–47% of ACL tears) (7,22,25) and can progress to complete ACL deficiency, particularly when the amount of ligament tear comprises more than half of its substance

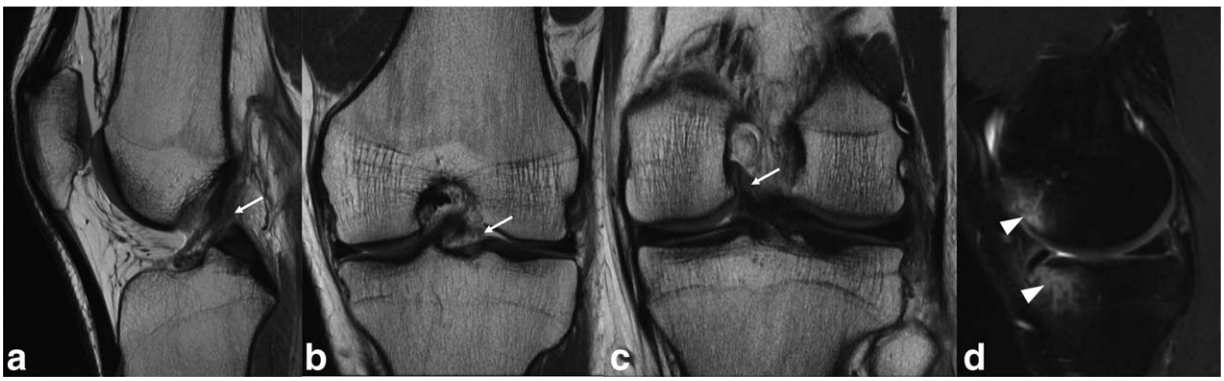

Figure 4. Isolated PLB tear of the ACL in a 24-year-old patient with resultant laxity, who eventually underwent isolated reconstruction of the PLB. **a:** Sagittal and **(b,c)** coronal proton density-weighted fast spin-echo MR images show an isolated tear of the PLB (arrows). **d:** Sagittal T2-weighted fat saturated fast spin-echo MR image shows associated bone marrow edema pattern in the anterior lateral femoral condyle and anterior tibia plateau (arrowheads) due to hyperextension injury.

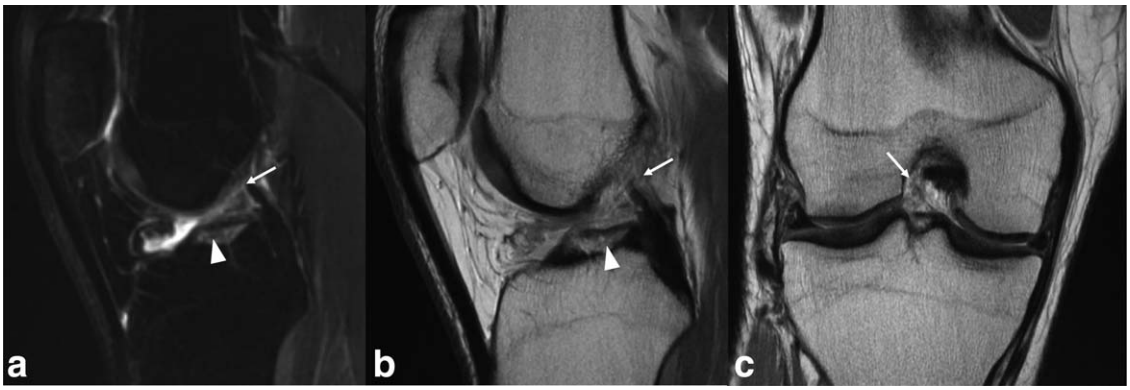

Figure 5. Chronic, complete ACL tear in a 29-year-old patient. The (a) sagittal T2-weighted fat saturated fast spin-echo and (b) proton density-weighted fast spin-echo MR images show absent ACL with hypointense, horizontally oriented remnant fibers and the (c) coronal proton density-weighted fast spin-echo image shows an "empty notch sign."

(26). Partial ACL tears are more difficult to diagnose in MRI than complete tears because of their various tear patterns (25). A higher sensitivity (87%), specificity (87%), and accuracy (87%) has been described by using standard orthogonal sequences plus oblique axial intermediate-weighted images (27). MR signs of partial tears are (a) abnormal intra-ligament signal, (b) bowing of the ligament, and (c) inability to identify all fibers (28). In partial tears, both bundles can be affected partially or one of the two bundle can be torn completely with the AMB more commonly affected than the PLB (12,29) (Fig. 4).

Chronic ACL Tears

Chronic ACL tears may show (a) hypointense horizontally oriented remnant fibers, (b) ACL resorption yielding the "empty notch" sign and/or (c) anterior displacement of the tibia relative to the femur on "nonloaded" MRI (13–15,30,31) (Fig. 5). Careful scrutiny of the individual bundle orientation is necessary to disclose more subtle, chronic partial tears.

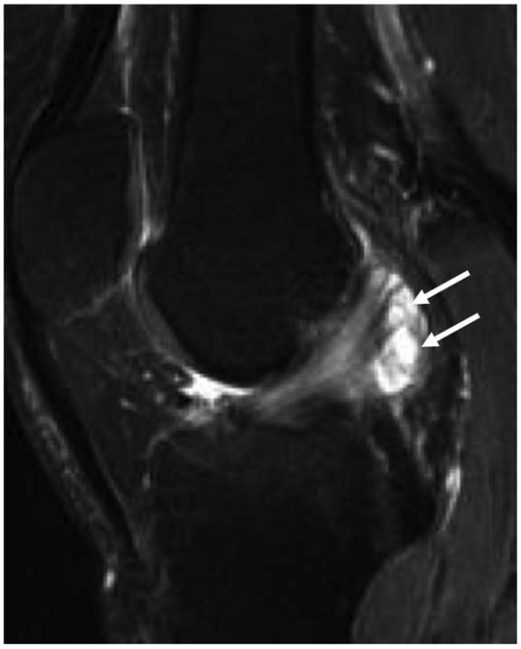

Figure 6. Ganglion cysts of ACL (arrows) in a 60-year-old patient with a stiff knee, shown on sagittal T2-weighted fat saturated fast spin-echo MR image.

Ganglion Cysts of the Cruciate Ligaments

Ganglion cysts consist of mucinous degeneration of connective tissue and/or synovial fluid imbibition (Fig. 6). These cysts may cause intermittent pain or restricted knee motion (particularly the extremes of flexion) but do not necessarily reflect ACL tear (32).

Reconstruction of the ACL

Autograft tendon harvest is the graft of choice in most orthopedic practices instead of the formerly used prosthetic ligament grafts (33–35). The most common autologous grafts are a bone–patellar tendon–bone (BPTB) or a multiple-strand hamstring with semitendinosus and gracilis tendon (34,36,37) (Fig. 7). The use of hamstring grafts is becoming more popular because of low reported graft side morbidity (38). Given that the material properties of the graft are a function of the graft cross sectional diameter, the hamstring tendons are commonly doubled or quadrupled to reinforce the tissue, often interlinked with suture. Given the suture reinforcement, increased susceptibility artifact will be encountered, particularly when scanning at field strengths of 3 Tesla (T) or higher, and the use of wider receiver bandwidth is helpful in reducing the artifact around the graft and at the points of fixation.

The double bundle reconstruction was introduced to restore the AMB and the PLB to maintain the anatomy and kinematics of the knee in comparison to the single bundle reconstruction (Fig. 7). Although many studies failed to show any significant differences between the two techniques (39–41), a recent meta-analysis of eighteen studies states a (a) significant higher negative rate of pivot shift and positive Lachman test, (b) significant differences regarding the International Knee Documentation Committee measurements (IKDC) Score, and (c) relevant decrease in complications (42). Others have documented a

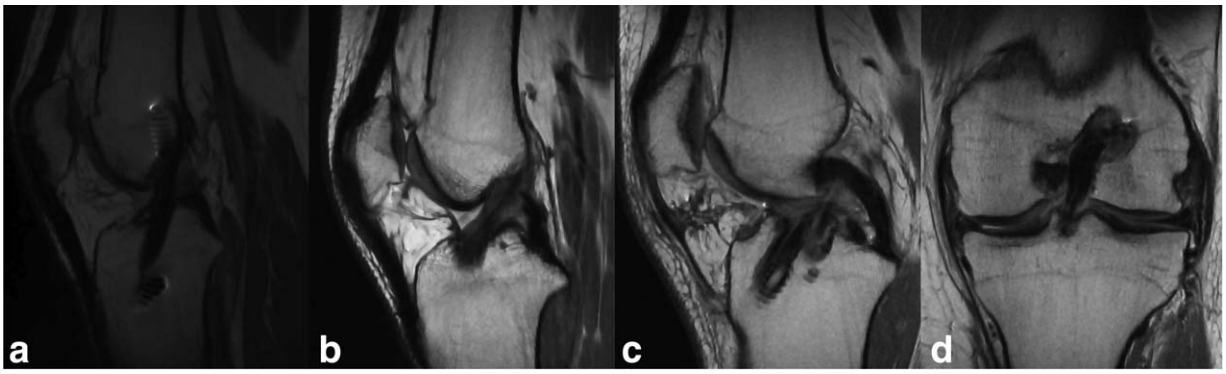

Figure 7. Different ACL reconstructions. Sagittal proton density-weighted fast spin-echo images show **(a)** normal appearance of a single bundle BPTB reconstruction, 6 years postoperative, **(b)** a single bundle reconstruction in a "more anatomic position," 11 months postoperative and **(c,d)** a double bundle reconstruction with a hamstring graft, 7 months postoperative.

Figure 8. Intact BPTB ACL graft with persistent anterior displacement of the tibia (laterally 1.3 cm, normally < 5 mm) (18) in a 19-year-old patient, noted on **(a)** coronal and **(b)** sagittal proton density-weighted fast spin-echo.

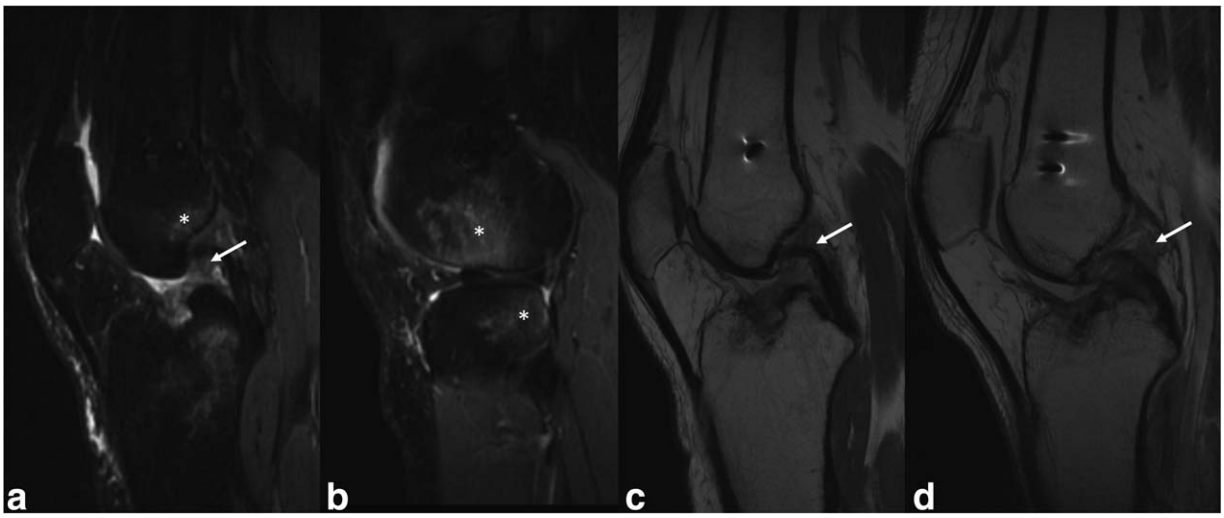

Figure 9. Acute and chronic ACL graft ruptures. Sagittal **(a,b)** T2-weighted fat saturated fast spin-echo and **(c)** proton density-weighted fast spin-echo MR images show acute ACL graft rupture (arrows) in a 41-year-old patient. Note the bone edema pattern within the lateral femoral condyle and in the posterolateral tibial plateau (*). **(d)** Sagittal proton density-weighted fast spin-echo MR image shows chronic ACL graft rupture (arrow) in a 51-year-old patient.

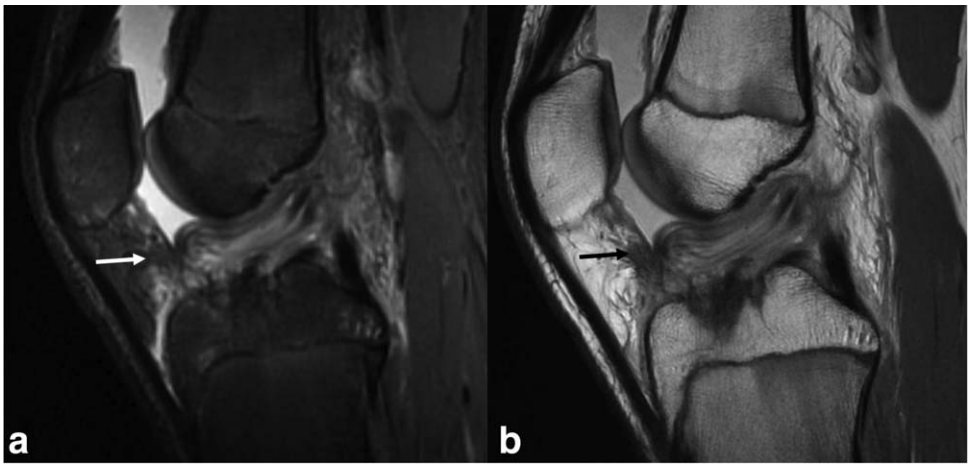

Figure 10. ACL graft impingement in a 15-year-old patient. Sagittal (**a**) T2-weighted fat saturated fast spin-echo and (**b**) proton density-weighted fast spin-echo MR images show a thickened, diffusely hyperintense ACL graft with localized scarring of the Hoffa's fat pad, consistent with a cyclops lesion (arrows).

decreased revision rate in a 2-year follow-up (43). Further studies are needed to prove a superior result with the double-bundle reconstruction (44).

In the setting of a partial tear, partial reconstruction of the affected band may be performed as an augmentation (29). Previous studies have recommended reconstruction of individual bundle tears, as it prevents anterior laxity, preserves neuronal elements and mechanoreceptors, and influences the vascularity and reinnervation, also in regard due to the risk of progression to full thickness tears and functional ACL insufficiency if the partial ACL tear involve more than 50% of the ligament fibers, (26,29).

Normal MRI Appearance of ACL Grafts

A correct surgical placement of the femoral and tibial tunnels is crucial to restore knee homeostasis, resolve functional instability and limit complications of reconstruction such as impingement or graft failure. In the traditional endoscopic techniques, the femoral tunnel is placed as far posterior as possible, and only a 1–2 mm thick cortical rim should remain (36). The opening of the proximal tibial tunnel in the sagittal plane should be immediately posterior to the intersection of the Blumensaat's line and in the coronal plane, at the intercondylar eminence (36). Three-dimensional high spatial resolution sequences are recommended to obtain oblique axial images for better visualization of the double-bundle graft (45–47).

A homogenously hypointense signal on moderate to long TE sequences in the proximal to midportion is considered normal on all pulse sequences in the immediate postoperative period in BPTB and hamstring grafts (48–51), but the latter may have a striated appearance because of the four separate strands and may contain small amounts of fluid collections in the osseous tunnel (34,35,50). After 3–8 months, the graft undergoes revascularization, cellular remodeling, and re-synovialization, which changes the MR signal

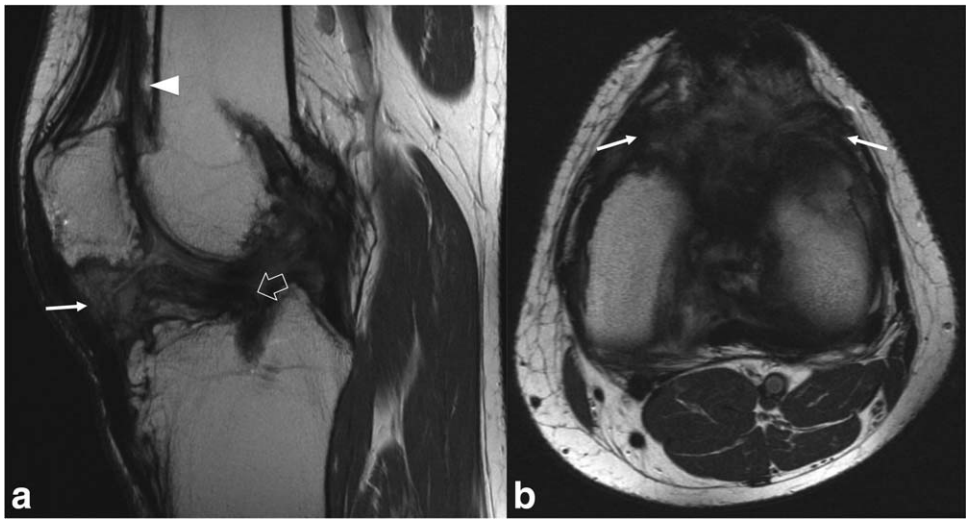

Figure 11. ACL arthrofibrosis with a ruptured ACL graft in a 42-year-old patient. The (**a**) sagittal and (**b**) axial proton density-weighted fast spin-echo MR images show diffuse fibrous scarring of the Hoffa's fat pad (arrows) with extension to the suprapatellar recess (arrowhead). Note remnant of the ACL graft (open arrow).

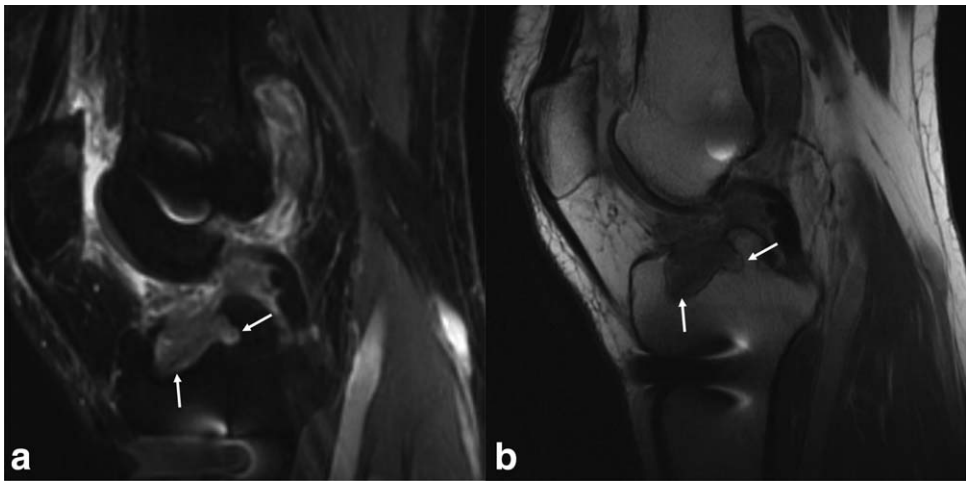

Figure 12. Tunnel widening in a synthetic graft in a 51-year-old patient who underwent ACL reconstruction in the 1980s. Sagittal (**a**) T2-weighted fat saturated fast spin-echo (**b**) proton density-weighted fast spin-echo MR images show reactive synovitis surrounding a synthetic (Gortex) graft with tunnel expansion (arrows).

from hypointense signal to a T1- and T2-weighted intermediate signal (33,52). After 12 months, the graft typically resembles a native ACL histologically (52) and on MRI (47,50) (Fig. 7a). This process has been described as "ligamentization" of the tendon graft (53). After 12 months following ACL graft reconstruction, high sensitivity (100%) and specificity (86%) and accuracy (87%) in diagnosing ACL graft tears can be achieved (54). However, in some cases increased intrasubstance signal may remain for years and may challenge the diagnosis of graft tears (55). It is, therefore, of utmost importance to correlate the MR findings with clinical functions and symptoms. Persistent anterior displacement of the tibia relative to the femur is noted following clinically successful ACL reconstruction, suggesting that the native mechanics of the knee are not fully restored following surgery (Fig. 8).

Note should be made that the more recent trend toward an "anatomic" femoral and tibial footprint brings the graft more inferiorly on the femur in the intercondylar notch and more anteromedially on the tibia (56) (Fig. 7b). This affects the signal properties of the graft, with more prolonged hyperintensity in the delayed perioperative period. It remains unclear if this signal reflects plastic deformation of the graft or the fact that these grafts are "seeing" more load. Further study in this area is warranted.

Complication of ACL Reconstruction

Complications associated with ACL reconstruction include: (a) partial or complete rupture, (b) graft impingement, (c) arthrofibrosis, (d) tunnel expansion/osteolysis, (e) ganglion formation, and (f) infection (33,51).

Graft ruptures are almost always associated with trauma. The MR criteria for graft tear are (a) increased signal intensity within the graft on water sensitive pulse sequences together with (b) partial or complete discontinuity of the fibers, depending on the amount of rupture (33,51) (Fig. 9). Associated findings due to the pivot shift result in bone contusion pattern due to the transchondral fractures (35,57) (Fig. 9b). Most of the secondary signs described for native ACL tears are not helpful in diagnosing ACL graft tears in terms of low sensitivity and specificity (57); for example, an uncovered posterior lateral meniscal horn, a horizontal orientation of the graft, an abnormal PCL line or buckling of the PCL may be due to the persistent anterior displacement of the tibia (57).

Graft impingement is most commonly a result of a mal-positioned proximal tibial tunnel and presents clinically as loss of terminal knee extension (56,58,59). An additional cause is mechanical irritation of the synovium adjacent to the native ACL stump when not entirely debrided. Impingement is best detected on sagittal images on MRI. Increased signal intensity within an intact graft may be seen at the site of impingement (33). A notchplasty can prevent impingement of the graft against the roof of the notch (60,61). Impingement may also lead to focal fibrosis and nodule formation resulting in a cyclops lesion (Fig. 10).

Arthrofibrosis is one of the most serious complications following ligament surgery of the knee with incidences ranging from 4–35% (62), presenting clinically with limited joint motion and ultimately in a mechanical block. It is caused by fibrous scarring of the Hoffa's fat pad with possible extension to the supra- and parapatellar recesses and appears on MRI as a diffuse T1- and T2-weighted hypointense mass (35) (Fig. 11). Arthrofibrosis is a cytokine-mediated globalized capsular contraction (63,64) and is distinguished from the focal mechanical deformation of the synovium in the cyclops lesion. It should not be confused with normal postoperative changes, appearing as a linear low signal intensities within Hoffa's fad pad. A retained native ACL remnant can clinically and on MRI mimic the signs of arthrofibrosis.

Tunnel expansion or osteolysis is most commonly observed within the first 3 months after reconstruction. Signs for tunnel expansion on MRI are (a) tunnel widening and (b) T2-weighted hyperintense signal around the graft within the femoral and tibial tunnels,

Figure 13. ACL graft infection in a 57-year-old patient. **(a)** Sagittal T2-weighted fat saturated fast spin-echo MR image shows multiple lymph nodes within the popliteal fossa (arrows). **(b)** Axial proton density-weighted fast spin-echo MR image shows lamellated synovium (arrowheads) and a lymph node in the popliteal fossa (arrow). The **(c)** sagittal and **(d)** axial proton density-weighted fast spin-echo MR images show widening of the tibial tunnel (open arrows).

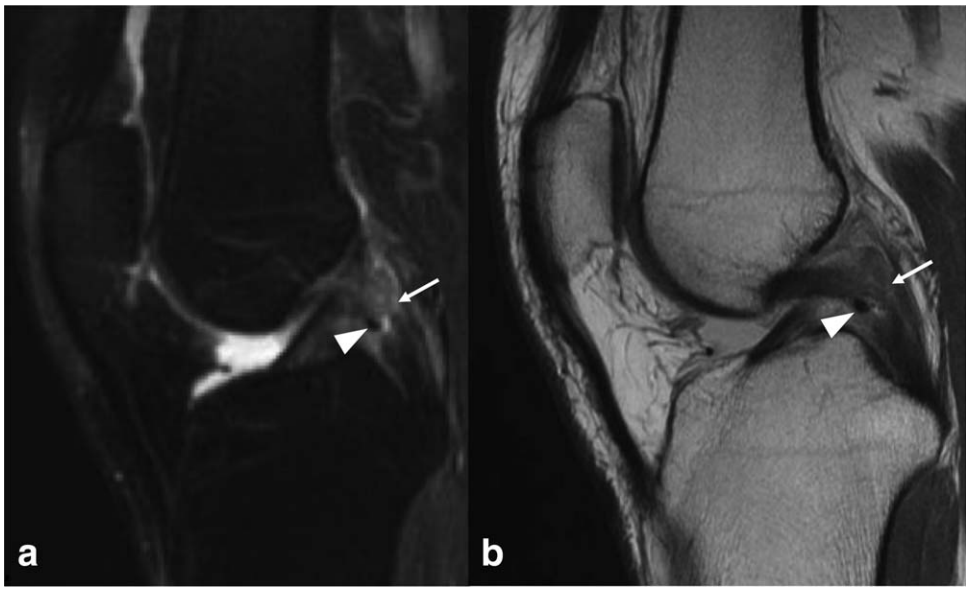

Figure 14. Complete PCL tear in a 27-year-old patient. Sagittal **(a)** T2-weighted fat saturated fast spin-echo and **(b)** proton density-weighted fast spin-echo MR images show a hyperintense, disrupted PCL (arrows). Note intact Humphrey ligament (arrowheads).

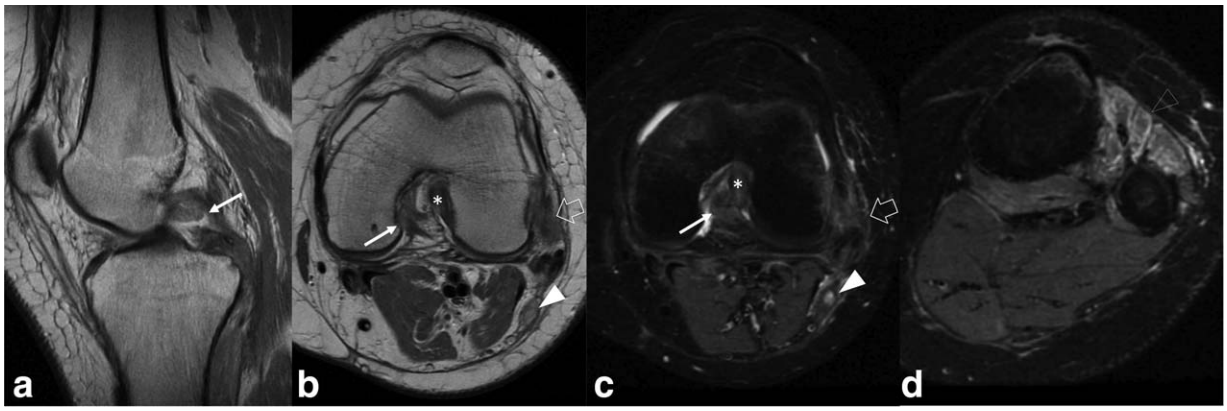

Figure 15. Multiple ligament knee injury with associated nerve injury in a 16-year-old patient. The (**a**) sagittal proton density-weighted fast spin-echo MR image shows complete rupture of the PCL. Axial (**b**) proton density-weighted fast spin-echo and (**c**) T2-weighted fat saturated fast spin-echo MR images show ruptured PCL (arrow), ruptured ACL (*), posterolateral corner injury (open arrow), and hyperintense signal alterations within the common peroneal nerve (arrowhead). (**d**) Axial T2-weighted fat saturated fast spin-echo image shows denervation edema within the extensor compartment (open arrowhead).

representing either fluid and/or granulation tissue (35). Recognition of tunnel expansion must occur early, as a complex two-stage revision becomes required if the tunnel expansion is too pronounced (35,65).

Although no longer commonly used for ligament reconstruction, synthetic grafts yield a distinct appearance on MRI and, in a suitable host, may incite an inflammatory reaction throughout the synovium, resulting in tunnel widening that can pose a challenge at the time of revision, requiring tunnel bone grafting (66) (Fig. 12). When assessing for any adverse synovial response following ligament reconstruction, a knowledge of the surgical used technique is crucial in assessment (33).

Ganglion cysts within the graft tunnel and also pretibial ganglion cyst formation has been reported in a minority of cases (36,67). Tunnel cysts may progress to tunnel widening but only rarely in graft instability. More commonly, the cysts may extent out the tibial tunnel and generate pain in the thin adjacent subcutaneous fat. Reported factors leading to tunnel cysts formation are bioabsorbable interference screws, non-absorbable suture fragments, and joint fluid leakage during failed ACL revision (35).

Graft infection is rare (incidence of 0.1–0.9%) and often found in the early postoperative phase (36). Classic clinical signs of infection might be absent, particularly in low grade infections (36). MR signs for graft infection are synovitis with lamellated synovium, bone erosion, periarticular edema, sinus tract, or abscess formation (36,51) (Fig. 13). In the setting of infection following allograft reconstruction, the allograft bone may serve as a sequestrum and should be removed at the time of debridement.

POSTERIOR CRUCIATE LIGAMENT

Anatomy and Normal MR Appearance

The PCL originates from the lateral aspect of the medial femoral condyle at the intercondylar notch, inserts at the posterolateral aspect of the intra-articular tibia and creates a vertical angle of 30–45°, depending on the amount of flexion (68). The fiber

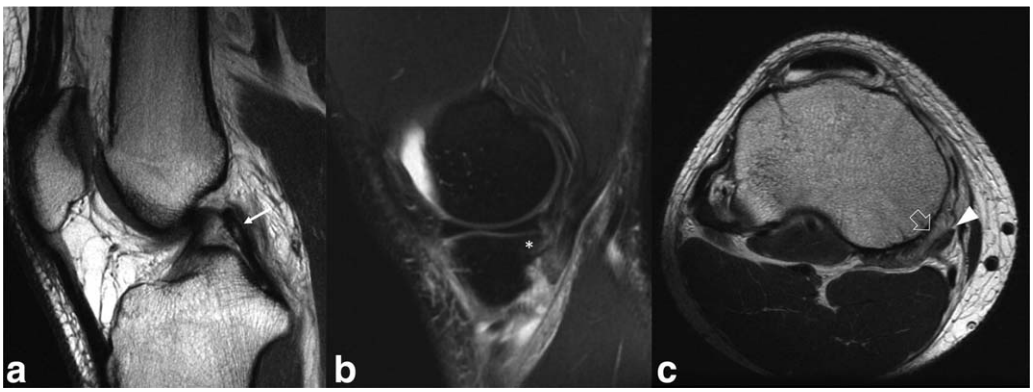

Figure 16. High grade PCL partial tear in a 19-year-old patient who injured his knee while playing football. (**a**) Sagittal proton density-weighted fast spin-echo MR image shows hyperintense signal alteration within the PCL (arrow), (**b**) sagittal T2-weighted fat saturated fast spin-echo MR image shows bone marrow edema pattern in the posteromedial tibial plateau (*) and (**c**) axial proton density-weighted fast spin-echo MR image shows an associated MCL tear (open arrow) and semimembranosus tendon avulsion (arrowhead).

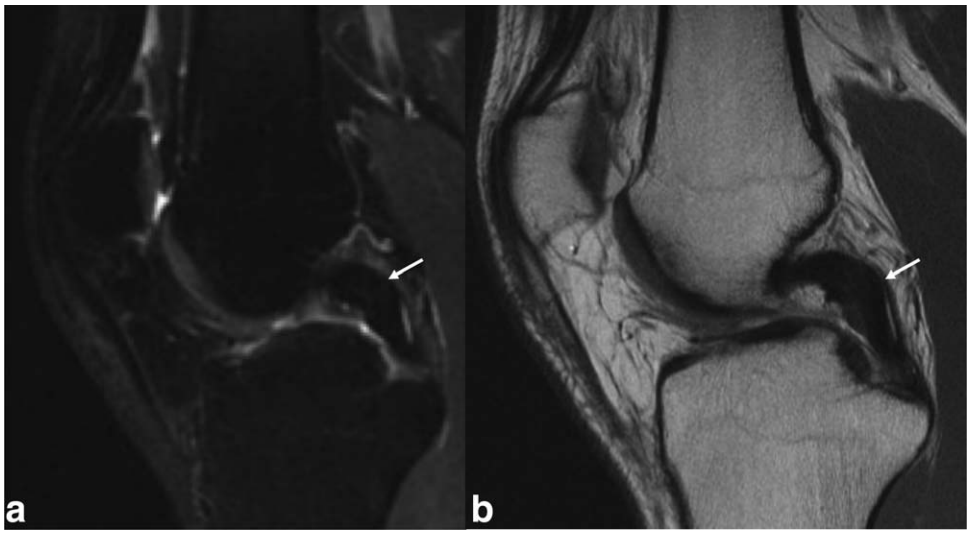

Figure 17. A 26-year-old patient 4 years after a sports injury. The sagittal (a) T2-weighted fat saturated fast spin-echo and (b) proton density-weighted fast spin-echo MR images demonstrate minimal signal alteration and focal thickening on the fat suppression but moderately abnormal signal on the nonfat suppressed images within the PCL (arrows).

bundles of the PCL are spirally oriented and the PCL is thicker and stronger than the ACL (69). It is also extrasynovial and consists of two functional but less well defined anatomic components compared with the ACL bundles; a larger anterolateral bundle (ALB) and a smaller posteromedial bundle (PMB) (68). Biomechanically, the PCL is the primary stabilizer to prevent posterior translation of the tibia (70). At high flexion the ALB is important for the mediolateral translation, whereas the PMB is more important in constraining the anteroposterior translation of the tibia (71). Low signal intensity in a well-defined band on all pulse sequences is a normal MRI appearance (69).

Acute Complete PCL Tears

Most commonly, the PCL is injured by direct high velocity force to the anterior aspect of the flexed knee, as the dashboard injury (Table 1) (72–74). Most often PCL tears occur in its midsubstance (63%) and less commonly proximally (27%) or distally (3%), or as an avulsion injury of the tibial insertion (7%) (69). Direct signs for tears are (a) increased signal intensity within the ligament, (b) discontinuity of the fibers, and (c) redundancy of an avulsed ligament (75) (Figs. 14 and 15). Associated other injuries to the knee are frequent (>50%). Meniscal tears are the most common associated injuries, with the medial side more commonly affected than the lateral side (69). Further associated injuries are other ligament injuries, including the MCL, ACL, and posterolateral corner structures, and direct bone contusions from anterior impaction to the tibia (30,69). Abnormal bone alignment may be noted as a posterior shift of the tibia (30). Complete PCL tears are often associated with multiple ligament injuries resulting in complete knee

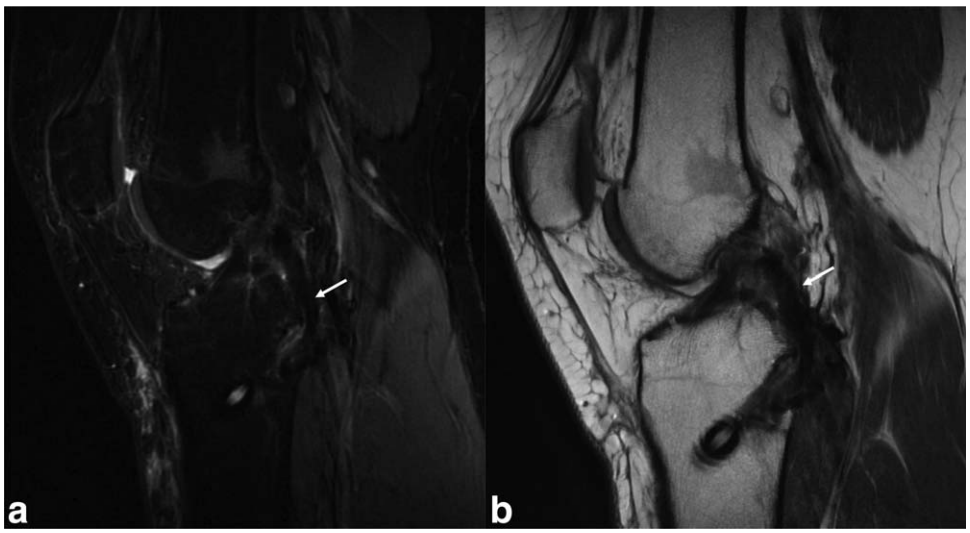

Figure 18. Intact PCL reconstruction in a 22-year-old patient shown on sagittal (a) T2-weighted fat saturated fast spin-echo and (b) proton density-weighted fast spin-echo.

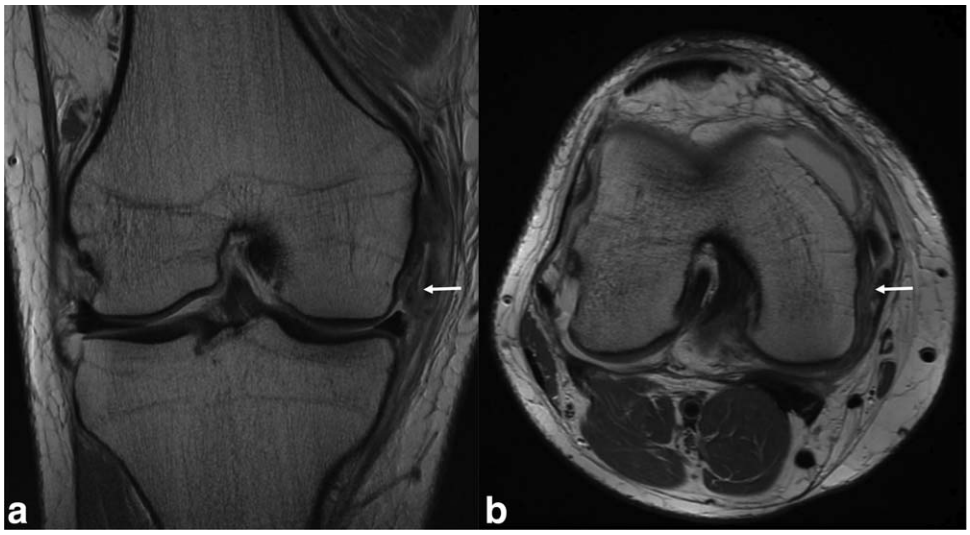

Figure 19. Complete MCL tear in a 27-year-old patient. The (**a**) coronal and (**b**) axial proton density-weighted fast spin-echo MR images show complete disrupted MCL (arrows). Note that the injury has extended to the medial patellofemoral ligament on the axial image.

dislocation and adjacent popliteal artery (up to 45%) or nerve injuries, with the peroneal nerve as the most common injured nerve (12,76–78) (Fig. 15). Nerve thickening, intrasubstance hyperintense signal abnormalities or disruption of the nerve and surrounding edema are indicators for nerve damage. It has been shown that nerve injuries are often observed by MRI and surgery in patients who have clinically significant symptoms (12). The implementation of contrast-enhanced MR angiography (MRA) is useful in patients who are presenting with multiple ligament injured knees, in the presence or even in the absence of decreased palpable popliteal or dorsalis pedis pulses (12,79).

Acute and Chronic Partial PCL Tears

Acute partial PCL tears demonstrate hyperintense signal alterations on water sensitive pulse sequences without complete disruption of the ligament (Fig. 16). Without history of trauma and a more extensively increased signal on short TE images, mucoid degeneration must be considered (80). Chronic PCL partial tears or scarring after an injury may demonstrate minimal signal alteration and focal thickening of the PCL (Fig. 17).

Reconstruction of the PCL

The incidence of PCL injuries is far less common than that of ACL, somewhere between 1 and 44% of injured knees (69,73). Therefore, there are fewer outcome studies available and the single bundle reconstruction is more often used (81). In comparison to formerly conservative treatment of PCL injuries, reconstruction of the PCL is becoming progressively important because of the emphasis that chronic instability is

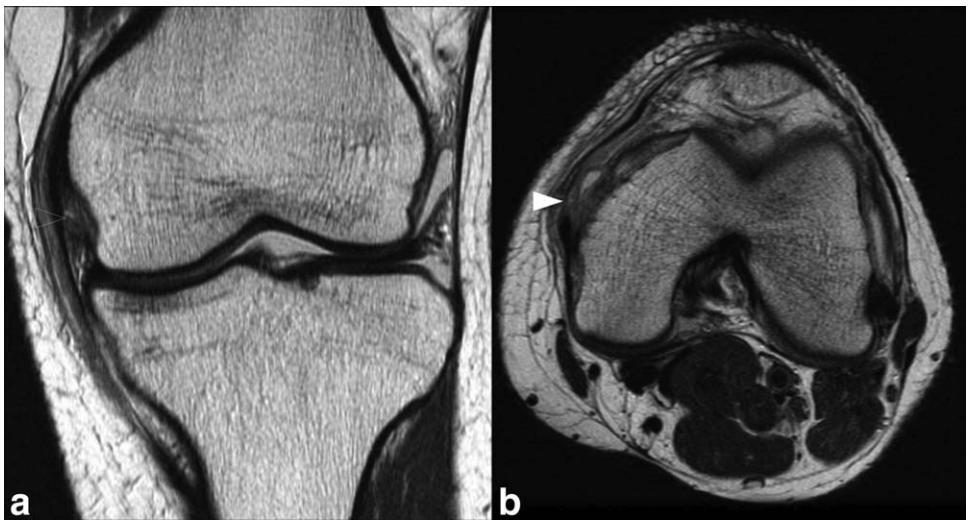

Figure 20. Partial MCL tear dissecting into the patellofemoral ligament in a 17-year-old patient. The (**a**) coronal and (**b**) axial proton density-weighted fast spin-echo MR images show disruption of the deeper layer of the MCL (open arrowhead) with meniscocapsular separation and a partial tear of the medial patellofemoral ligament (arrowhead).

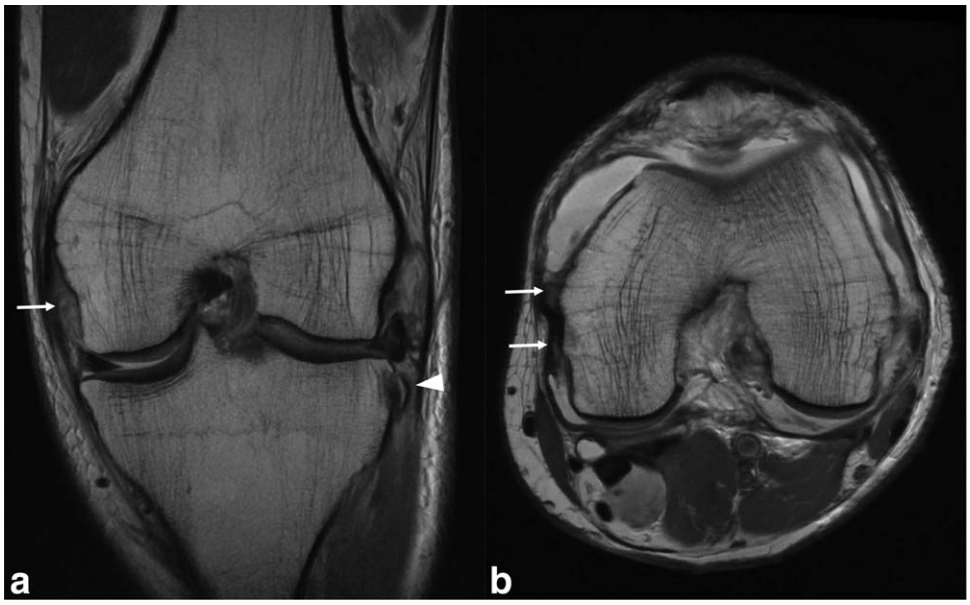

Figure 21. MCL partial tear in a 45-year-old patient. The (**a**) coronal and (**b**) axial proton density-weighted fast spin-echo MR images show disrupted fibers of the deep layer of the MCL (arrows). Incidentally, a Segond avulsion is noted (arrowhead).

leading to early degenerative changes (82). For PCL reconstruction, autografts such as BPTB, hamstring, quadriceps tendon and allografts such as Achilles, tibialis anterior and tibialis posterior tendon can be used (83), with the BPTB and hamstring as the most commonly used grafts. The normal MR appearance of the PCL grafts parallels the findings of the ACL grafts (35) (Fig. 18). Some authors have noted persistent increased intrasubstance signal on both T1- and T2-weighted image in serial evaluation in the first year (84).

MEDIAL COLLATERAL LIGAMENT

Anatomy and Normal MCL Appearance

The MCL originates from the medial epicondyle of the femur posteriorly and attaches at the proximal metaphysis of the tibia approximately 6 cm below the joint capsule (85). It contains two dominant components: superficial and deep fibers. At the anterior third of the medial aspect of the knee joint, the superficial MCL layer and the crural fascia are fused and form the medial retinaculum (86,87). At the posterior third, the superficial and the deep MCL layer fuse to form the posterior oblique ligament (POL) (86,87). The POL together with the semimembranosus tendon and their aponeurotic extensions form the posteromedial corner (87,88). The deep layer of the MCL inserts directly in the medial meniscus (86) and consists of a meniscofemoral and meniscotibial ligament whose attachments are either at the femoral condyle or at the superficial MCL layer and at the tibia inferiorly to the joint space, respectively (85,87–89). Between the superficial and deep layers, there is a bursa and variable amount of fatty tissue (86). The MCL is normally thin and of low signal intensity in all MR pulse sequences and it is best seen in coronal or axial images (30,86).

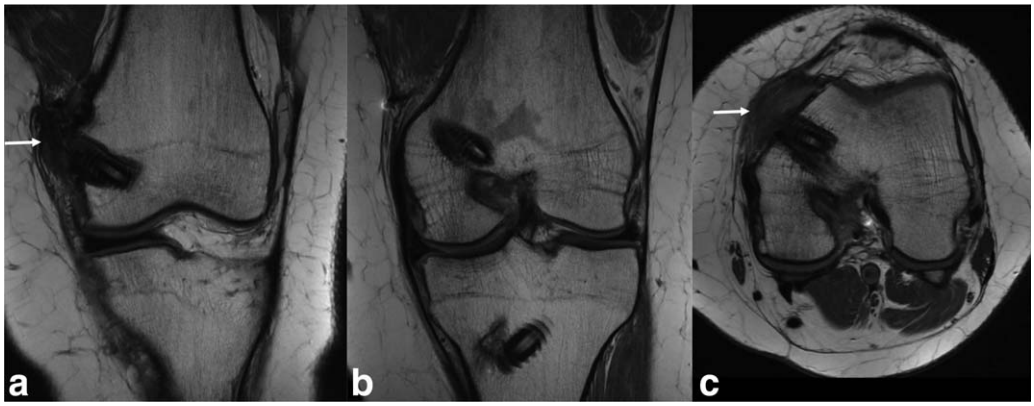

Figure 22. MCL repair in a 22-year-old patient shown on (**a,b**) coronal and (**c**) axial proton density-weighted fast spin-echo MR images. Note the hypertrophic scarring at the femoral origin (arrows).

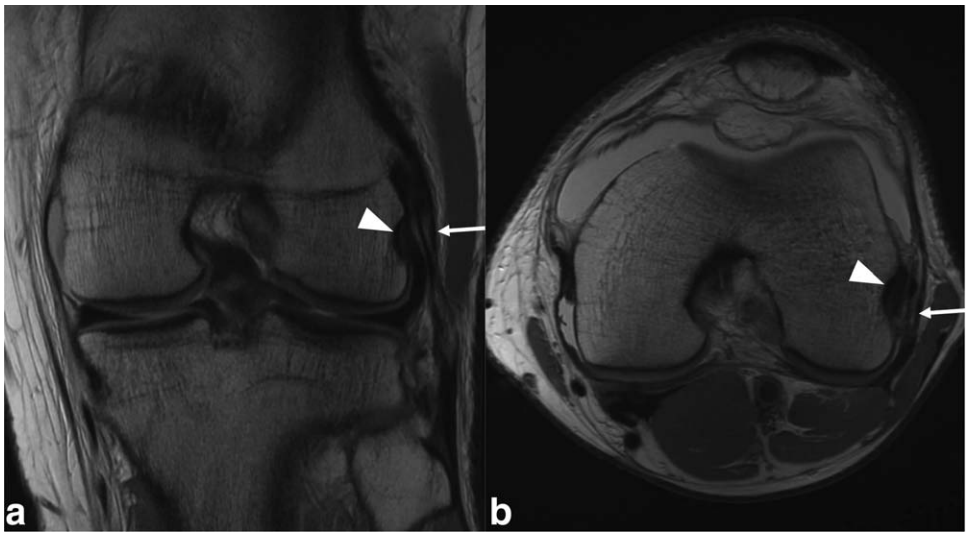

Figure 23. Posterolateral corner injury in a 25-year-old patient. The (**a**) coronal and (**b**) axial proton density-weighted fast spin-echo MR image show signal alteration within the LCL (arrow) and of the popliteus tendon (arrowhead) at their origin, corresponding to high-grade partial tears.

Pathologic MRI MCL Appearance

MCL tears most often occur following valgus stress, clipping injuries in valgus and pivot shift injuries (Table 1) (74). MCL tears are most common in the proximal fibers, followed by distal and midsubstance (12). A complete MCL tear results in discontinuity and hyperintense signal on all MR pulse sequences (Fig. 19). Associated avulsion fractures at the attachment site or an associated valgus compression fractures of the lateral compartment may be found (30,90). When diagnosing anterior MCL tears at the femur on coronal MR images, careful scrutiny of the axial images is necessary to determine the integrity of the medial patellofemoral ligament and retinaculum (Figs. 19 and 20). In severe injuries, dissection may continue to the vastus medialis obliquus (VMO) fibers or to the semimembranosus tendon (Fig. 16).

Partial tears demonstrate hyperintense signal on all pulse sequences and discontinuity of at least some fibers, whereas low grade injuries are typically manifest as a thickened, mildly hyperintense MCL on all pulse sequences and perifocal edema (30) (Figs. 20 and 21). Surrounding edema is often observed in any acute MCL injuries, although it is nonspecific and can also be present in other knee problems, such as meniscal tears or osteoarthritis (91).

Chronic MCL tears demonstrate a thickened ligament and may be associated with calcification or ossification of the medial collateral ligament, also known as the Pellegrini-Stieda disease (92,93).

MCL Reconstruction and Normal MR Appearance

MCL fibroblasts have a higher capacity to remodel to functional capacity compared with ACL fibroblasts. As such, the MCL rarely undergoes primary repair; when necessary, this is typically performed as an augmentation using autologous hamstring tendon (Bosworth procedure) (94). In the setting of a multiple ligament injured knee, the deficient MCL is reconstructed with allograft tissue.

The postoperative MCL is denoted as a thickened ligament and may persist thickened for many years. The signal intensity in the T1- and T2-weighted images are initially increased and starts decreasing over time (Fig. 22). Postoperative ossification may occur (Pellegrini-Stieda) (35).

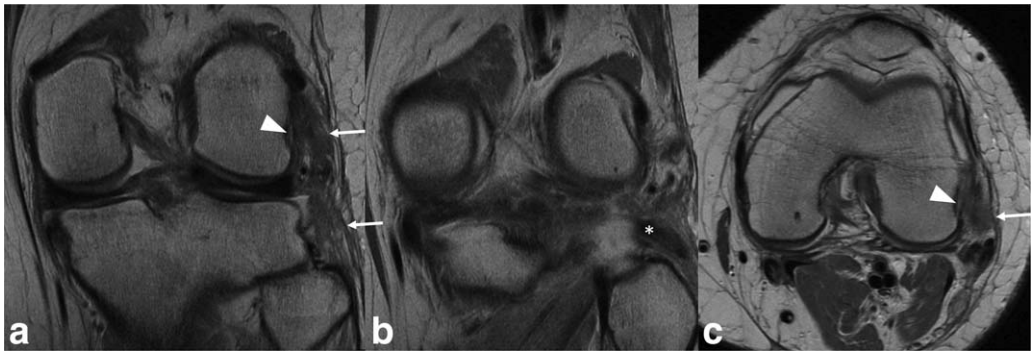

Figure 24. Severe posterolateral corner injury in a 16-year-old patient who had a multiple ligament knee injury. The (**a**,**b**) coronal and (**c**) axial proton density-weighted fast spin-echo MR images show complete rupture of the LCL (arrows) and the popliteus tendon (arrowheads), the latter of which displaced onto the popliteofibular ligament (*).

POSTEROLATERAL CORNER

Anatomy and Normal PLC Appearance

The lateral capsular structures are best divided in an anterolateral and posterolateral stabilizing complex. The anterolateral stabilizing complex contains the fascia lata, which continues as the iliotibial tract and together form the lateral patellar retinaculum and insert at the tubercle of Gerdy (95). The posterolateral stabilizing complex or posterolateral corner structures include: (a) the LCL, (b) the posterolateral capsule, (c) the arcuate ligament, (d) the popliteofibular ligament, (e) the fabellofibular ligament, (f) popliteus tendon/muscle, (g) biceps femoris tendon, and (h) the lateral head of the gastrocnemius (35,95,96). The popliteus muscle is a rotatory stabilizer; thus, its course is obliquely oriented, running from medial to lateral and posterior to anterior on serial coronal MR images. The term "posterolateral corner" usually refers to those components that are subject to eventual reconstruction, including the LCL, popliteus tendon, and the popliteofibular ligament.

The LCL originates from the lateral femoral condyle immediately below the lateral gastrocnemius muscle and insert as conjoined tendon with the biceps femoris tendon at the head of the fibula, laterally (88,97). The popliteus tendon arises from the lateral femoral condyle intra-articular below the lateral collateral ligament and attaches at the posteromedial surface of the proximal tibia (97). The popliteus tendon is connected to the fibula by the popliteofibular ligament, which inserts medially at the head of the fibula and further to the lateral meniscus by the popliteal meniscal ligament (95,98). The arcuate ligament is a thickening of the joint capsule, has an Y-shaped configuration and inserts at the head of the fibula immediately medially to the conjoined tendon of the LCL and biceps femoris (95). The oblique popliteal ligament reinforces together with the semimembranosus tendon the capsule (95). The lateral gastrocnemius tendon originates from the epicondylar process of the femur. The fabellofibular ligament is an inconsistent ligament that arises from the fabella, an osseous or cartilaginous body adjacent to the gastrocnemius tendon, and inserts at the lateral base of the fibular head between the popliteofibular ligament and the arcuate ligament (88,97).

The posterolateral corner structures are best identified using the coronal and axial MRI planes. Some investigators have found superior visualization of the ligaments by the use of a coronal oblique plane with the popliteus tendon as the key structure (99).

Pathologic MRI PLC Appearance

Posterolateral corner injuries are most often observed in severe extension and varus stress injuries with multiple ligament knee injuries (Table 1) (74). On MRI the LCL, popliteus tendon, popliteofibular ligament, and biceps femoris tendon injuries are denoted as increased signal intensity with disruption of fibers. Injuries of the popliteus tendon are most often found at the muscle-tendon junction and less commonly at its origin (Fig. 23). Isolated popliteus injury, however, may occur and the attachment at the femur should be routinely assessed on MR imaging, regardless of the suspected clinical diagnosis (100). Injuries of the PLC structures are often associated with other ligamentous injuries, particularly ACL, MCL, and PCL tears (96,101) (Table 1; Figs. 15 and 24). In the setting of a severe PLC injury, the adjacent peroneal nerve should be assessed for the presence of traumatic neuritis or disruption of nerve fascicles (Fig. 15). Similarly, the alignment of the tibiofibular joint should be determined, as well as the integrity of the capsular ligaments.

CONCLUSION

MRI allows reliable assessment of knee ligament structures and therefore is the image modality of choice in diagnosing knee ligament instability. This review demonstrates the MRI signal characteristics of the knee ligaments and helps understanding the complex anatomy of the knee joint. Depending on the mechanism of injury, attention should be directed toward specific knee ligament(s). The science of ligament reconstruction is a dynamic one, and the evolution of graft choices, tunnel placement and graft mechanics requires a continuous update on current orthopedic surgical techniques to ensure accurate and reproducible image interpretation.

REFERENCES

1. Lee J-J, Choi Y-J, Shin K-Y, Choi C-H. Medial meniscal tears in anterior cruciate ligament-deficient knees: effects of posterior tibial slope on medial meniscal tear. Knee Surg Relat Res 2011; 23:227–230.
2. Shefelbine SJ, Ma CB, Lee K-Y, et al. MRI analysis of in vivo meniscal and tibiofemoral kinematics in ACL-deficient and normal knees. J Orthop Res 2006;24:1208–1217.
3. Petersen W, Zantop T. Anatomy of the anterior cruciate ligament with regard to its two bundles. Clin Orthop Relat Res 2007;454: 35–47.
4. Giuliani JR, Kilcoyne KG, Rue J-PH. Anterior cruciate ligament anatomy: a review of the anteromedial and posterolateral bundles. J Knee Surg 2009;22:148–154.
5. Siegel L, Vandenakker-Albanese C, Siegel D. Anterior cruciate ligament injuries: anatomy, physiology, biomechanics, and management. Clin J Sport Med 2012;22:349–355.
6. Petersen W, Tillmann B. [Anatomy and function of the anterior cruciate ligament]. Orthopade 2002;31:710–718.
7. Siebold R, Fu FH. Assessment and augmentation of symptomatic anteromedial or posterolateral bundle tears of the anterior cruciate ligament. Arthroscopy 2008;24:1289–1298.
8. National Institutes of Health (NIH), National Institute of Arthritis and Musculoskeletal and Skin Diseases (NIAMS), Vanderbilt University, United States.A Multicenter Cohort Study. Available at: http://clinicaltrials.gov/ct2/show/NCT00463099. Accessed March 1, 2011.
9. Delin C, Silvera S, Coste J, et al. Reliability and diagnostic accuracy of qualitative evaluation of diffusion-weighted MRI combined with conventional MRI in differentiating between complete and partial anterior cruciate ligament tears. Eur Radiol 2013;23: 845–854.
10. Lee JK, Yao L, Phelps CT, Wirth CR, Czajka J, Lozman J. Anterior cruciate ligament tears: MR imaging compared with arthroscopy and clinical tests. Radiology. 1988;166:861–864.
11. Vellet AD, Lee DH, Munk PL, et al. Anterior cruciate ligament tear: prospective evaluation of diagnostic accuracy of middle-

and high-field-strength MR imaging at 1.5 and 0.5 T. Radiology 1995;197:826–830.
12. Potter HG, Weinstein M, Allen AA, Wickiewicz TL, Helfet DL. Magnetic resonance imaging of the multiple-ligament injured knee. J Orthop Trauma 2002;16:330–339.
13. Remer EM, Fitzgerald SW, Friedman H, Rogers LF, Hendrix RW, Schafer MF. Anterior cruciate ligament injury: MR imaging diagnosis and patterns of injury. Radiographics 1992;12:901–915.
14. Robertson PL, Schweitzer ME, Bartolozzi AR, Ugoni A. Anterior cruciate ligament tears: evaluation of multiple signs with MR imaging. Radiology 1994;193:829–834.
15. Boeree NR, Ackroyd CE. Magnetic resonance imaging of anterior cruciate ligament rupture. A new diagnostic sign. J Bone Joint Surg Br 1992;74:614–616.
16. Tung GA, Davis LM, Wiggins ME, Fadale PD. Tears of the anterior cruciate ligament: primary and secondary signs at MR imaging. Radiology 1993;188:661–667.
17. Al-Dadah O, Shepstone L, Marshall TJ, Donell ST. Secondary signs on static stress MRI in anterior cruciate ligament rupture. Knee 2011;18:235–241.
18. Hill PF, Vedi V, Williams A, Iwaki H, Pinskerova V, Freeman MA. Tibiofemoral movement 2: the loaded and unloaded living knee studied by MRI. J Bone Joint Surg Br 2000;82:1196–1198.
19. Gentili A, Seeger LL, Yao L, Do HM. Anterior cruciate ligament tear: indirect signs at MR imaging. Radiology 1994;193:835–840.
20. Schweitzer ME, Cervilla V, Kursunoglu-Brahme S, Resnick D. The PCL line: an indirect sign of anterior cruciate ligament injury. Clin Imaging 1992;16:43–48.
21. DeHaven KE. Diagnosis of acute knee injuries with hemarthrosis. Am J Sports Med 1980;8:9–14.
22. Noyes FR, Bassett RW, Grood ES, Butler DL. Arthroscopy in acute traumatic hemarthrosis of the knee. Incidence of anterior cruciate tears and other injuries. J Bone Joint Surg Am 1980; 62:687–695, 757.
23. Goldman AB, Pavlov H, Rubenstein D. The Segond fracture of the proximal tibia: a small avulsion that reflects major ligamentous damage. AJR Am J Roentgenol 1988;151:1163–1167.
24. Lafrance RM, Giordano B, Goldblatt J, Voloshin I, Maloney M. Pediatric tibial eminence fractures: evaluation and management. J Am Acad Orthop Surg 2010;18:395–405.
25. Van Dyck P, De Smet E, Veryser J, et al. Partial tear of the anterior cruciate ligament of the knee: injury patterns on MR imaging. Knee Surg Sports Traumatol Arthrosc 2012;20:256–261.
26. Noyes FR, Mooar LA, Moorman CT, McGinniss GH. Partial tears of the anterior cruciate ligament. Progression to complete ligament deficiency. J Bone Joint Surg Br 1989;71:825–833.
27. Ng AWH, Griffith JF, Hung EHY, Law KY, Yung PSH. MRI diagnosis of ACL bundle tears: value of oblique axial imaging. Skeletal Radiol 2013;42:209–217.
28. Umans H, Wimpfheimer O, Haramati N, Applbaum YH, Adler M, Bosco J. Diagnosis of partial tears of the anterior cruciate ligament of the knee: value of MR imaging. AJR Am J Roentgenol 1995;165:893–897.
29. Ochi M, Adachi N, Deie M, Kanaya A. Anterior cruciate ligament augmentation procedure with a 1-incision technique: anteromedial bundle or posterolateral bundle reconstruction. Arthroscopy 2006;22:463.e1–e5.
30. Mohana-Borges AVR, Resnick D, Chung CB. Magnetic resonance imaging of knee instability. Semin Musculoskelet Radiol 2005;9: 17–33.
31. Chen W-T, Shih TT-F, Tu H-Y, Chen R-C, Shau W-Y. Partial and complete tear of the anterior cruciate ligament. Acta Radiol 2002;43:511–516.
32. Garcia-Alvarez F, Garcia-Pequerul JM, Avila JL, Sainz JM, Castiella T. Ganglion cysts associated with cruciate ligaments of the knee: a possible cause of recurrent knee pain. Acta Orthop Belg 2000;66:490–494.
33. Schatz JA, Potter HG, Rodeo SA, Hannafin JA, Wickiewicz TL. MR imaging of anterior cruciate ligament reconstruction. AJR Am J Roentgenol 1997;169:223–228.
34. Gnannt R, Chhabra A, Theodoropoulos JS, Hodler J, Andreisek G. MR imaging of the postoperative knee. J Magn Reson Imaging 2011;34:1007–1021.
35. Sanders TG. Imaging of the postoperative knee. Semin Musculoskelet Radiol 2011;15:383–407.
36. Bencardino JT, Beltran J, Feldman MI, Rose DJ. MR imaging of complications of anterior cruciate ligament graft reconstruction. Radiographics 2009;29:2115–2126.
37. Siegel MG, Barber-Westin SD. Arthroscopic-assisted outpatient anterior cruciate ligament reconstruction using the semitendinosus and gracilis tendons. Arthroscopy 1998;14:268–277.
38. Lawhorn KW, Howell SM. Principles for using hamstring tendons for anterior cruciate ligament reconstruction. Clin Sports Med 2007;26:567–585.
39. Gobbi A, Mahajan V, Karnatzikos G, Nakamura N. Single- versus double-bundle ACL reconstruction: is there any difference in stability and function at 3-year followup? Clin Orthop Relat Res 2012;470:824–834.
40. Ahldén M, Samuelsson K, Sernert N, Forssblad M, Karlsson J, Kartus J. The Swedish National Anterior Cruciate Ligament Register: a report on baseline variables and outcomes of surgery for almost 18,000 patients. Am J Sports Med 2012;40:2230–2235.
41. Ventura A, Legnani C, Terzaghi C, Borgo E. Single- and Double-Bundle Anterior Cruciate Ligament Reconstruction in Patients Aged Over 50 Years. Arthroscopy 2012;28:1702–1709.
42. Zhu Y, Tang R-K, Zhao P, Zhu S-S, Li Y-G, Li J-B. Double-bundle reconstruction results in superior clinical outcome than single-bundle reconstruction. Knee Surg Sports Traumatol Arthrosc 2013;21:1085–1096.
43. Suomalainen P, Moisala A-S, Paakkala A, Kannus P, Jarvela T. Double-bundle versus single-bundle anterior cruciate ligament reconstruction: randomized clinical and magnetic resonance imaging study with 2-year follow-up. Am J Sports Med 2011;39: 1615–1622.
44. Tiamklang T, Sumanont S, Foocharoen T, Laopaiboon M. Double-bundle versus single-bundle reconstruction for anterior cruciate ligament rupture in adults. Cochrane Database Syst Rev 2012;11:CD008413.
45. Steckel H, Vadala G, Davis D, Fu FH. 2D and 3D 3-tesla magnetic resonance imaging of the double bundle structure in anterior cruciate ligament anatomy. Knee Surg Sports Traumatol Arthrosc 2006;14:1151–1158.
46. Poellinger A, Scheffler S, Hamm B, Asbach P. Magnetic resonance imaging of double-bundle anterior cruciate ligament reconstruction. Skeletal Radiol 2009;38:309–315.
47. Murakami Y, Sumen Y, Ochi M, Fujimoto E, Adachi N, Ikuta Y. MR evaluation of human anterior cruciate ligament autograft on oblique axial imaging. J Comput Assist Tomogr 1998;22:270–275.
48. Howell SM, Clark JA, Blasier RD. Serial magnetic resonance imaging of hamstring anterior cruciate ligament autografts during the first year of implantation. A preliminary study. Am J Sports Med 1991;19:42–47.
49. Recht MP, Piraino DW, Applegate G, et al. Complications after anterior cruciate ligament reconstruction: radiographic and MR findings. AJR Am J Roentgenol 1996;167:705–710.
50. Rispoli DM, Sanders TG, Miller MD, Morrison WB. Magnetic resonance imaging at different time periods following hamstring harvest for anterior cruciate ligament reconstruction. Arthroscopy 2001;17:2–8.
51. Papakonstantinou O, Chung CB, Chanchairujira K, Resnick DL. Complications of anterior cruciate ligament reconstruction: MR imaging. Eur Radiol 2003;13:1106–1117.
52. Arnoczky SP, Tarvin GB, Marshall JL. Anterior cruciate ligament replacement using patellar tendon. An evaluation of graft revascularization in the dog. J Bone Joint Surg Am 1982;64:217–224.
53. Amiel D, Kleiner JB, Roux RD, Harwood FL, Akeson WH. The phenomenon of "ligamentization": anterior cruciate ligament reconstruction with autogenous patellar tendon. J Orthop Res 1986;4:162–172.
54. Nakayama Y, Shirai Y, Narita T, Mori A, Kobayashi K. The accuracy of MRI in assessing graft integrity after anterior cruciate ligament reconstruction. J Nippon Med Sch 2001;68:45–49.
55. Saupe N, White LM, Chiavaras MM, et al. Anterior cruciate ligament reconstruction grafts: MR imaging features at long-term follow-up--correlation with functional and clinical evaluation. Radiology 2008;249:581–590.
56. Iriuchishima T, Shirakura K, Fu FH. Graft impingement in anterior cruciate ligament reconstruction. Knee Surg Sports Traumatol Arthrosc 2013;21:664–670.

57. Horton LK, Jacobson JA, Lin J, Hayes CW. MR imaging of anterior cruciate ligament reconstruction graft. AJR Am J Roentgenol 2000;175:1091–1097.
58. Howell SM. Principles for placing the tibial tunnel and avoiding roof impingement during reconstruction of a torn anterior cruciate ligament. Knee Surg Sports Traumatol Arthrosc 1998;(Suppl 1):S49–S55.
59. Bedi A, Maak T, Musahl V, et al. Effect of tibial tunnel position on stability of the knee after anterior cruciate ligament reconstruction: is the tibial tunnel position most important? Am J Sports Med 2011;39:366–373.
60. Akamatsu Y, Mitsugi N, Taki N, Takeuchi R, Saito T. Simultaneous anterior cruciate ligament reconstruction and opening wedge high tibial osteotomy: report of four cases. Knee 2010;17:114–118.
61. Hame SL, Markolf KL, Hunter DM, Oakes DA, Zoric B. Effects of notchplasty and femoral tunnel position on excursion patterns of an anterior cruciate ligament graft. Arthroscopy 2003;19:340–345.
62. DeHaven KE, Cosgarea AJ, Sebastianelli WJ. Arthrofibrosis of the knee following ligament surgery. Instr Course Lect 2003;52:369–381.
63. Chen MR, Dragoo JL. Arthroscopic releases for arthrofibrosis of the knee. J Am Acad Orthop Surg 2011;19:709–716.
64. Murakami S, Muneta T, Furuya K, Saito I, Miyasaka N, Yamamoto H. Immunohistologic analysis of synovium in infrapatellar fat pad after anterior cruciate ligament injury. Am J Sports Med 1995;23:763–768.
65. Wilson TC, Kantaras A, Atay A, Johnson DL. Tunnel enlargement after anterior cruciate ligament surgery. Am J Sports Med 2004;32:543–549.
66. Muren O, Dahlstedt L, Brosjo E, Dahlborn M, Dalen N. Gross osteolytic tibia tunnel widening with the use of Gore-Tex anterior cruciate ligament prosthesis: a radiological, arthrometric and clinical evaluation of 17 patients 13–15 years after surgery. Acta Orthop 2005;76:270–274.
67. Deie M, Sumen Y, Ochi M, Murakami Y, Fujimoto E, Ikuta Y. Pretibial cyst formation after anterior cruciate ligament reconstruction using auto hamstring grafts: two case reports in a prospective study of 89 cases. Magn Reson Imaging 2000;18:973–977.
68. Amis AA, Gupte CM, Bull AMJ, Edwards A. Anatomy of the posterior cruciate ligament and the meniscofemoral ligaments. Knee Surg Sports Traumatol Arthrosc 2006;14:257–263.
69. Sonin AH, Fitzgerald SW, Hoff FL, Friedman H, Bresler ME. MR imaging of the posterior cruciate ligament: normal, abnormal, and associated injury patterns. Radiographics 1995;15:551–561.
70. Veltri DM, Deng XH, Torzilli PA, Warren RF, Maynard MJ. The role of the cruciate and posterolateral ligaments in stability of the knee. A biomechanical study. Am J Sports Med 1995;23:436–443.
71. Papannagari R, DeFrate LE, Nha KW, et al. Function of posterior cruciate ligament bundles during in vivo knee flexion. Am J Sports Med 2007;35:1507–1512.
72. Hayes CW, Brigido MK, Jamadar DA, Propeck T. Mechanism-based pattern approach to classification of complex injuries of the knee depicted at MR imaging. Radiographics 2000;20(Spec No):S121–S134.
73. Schulz MS, Russe K, Weiler A, Eichhorn HJ, Strobel MJ. Epidemiology of posterior cruciate ligament injuries. Arch Orthop Trauma Surg 2003;123:186–191.
74. Sanders TG, Medynski MA, Feller JF, Lawhorn KW. Bone contusion patterns of the knee at MR imaging: footprint of the mechanism of injury. Radiographics 2000;20(Spec No):S135–S151.
75. Grover JS, Bassett LW, Gross ML, Seeger LL, Finerman GA. Posterior cruciate ligament: MR imaging. Radiology 1990;174:527–530.
76. Frassica FJ, Sim FH, Staeheli JW, Pairolero PC. Dislocation of the knee. Clin Orthop Relat Res 1991;263:200–205.
77. Almekinders LC, Logan TC. Results following treatment of traumatic dislocations of the knee joint. Clin Orthop Relat Res 1992;284:203–207.
78. Green NE, Allen BL. Vascular injuries associated with dislocation of the knee. J Bone Joint Surg Am 1977;59:236–239.
79. Welling RE, Kakkasseril J, Cranley JJ. Complete dislocations of the knee with popliteal vascular injury. J Trauma 1981;21:450–453.
80. Hodler J, Haghighi P, Trudell D, Resnick D. The cruciate ligaments of the knee: correlation between MR appearance and gross and histologic findings in cadaveric specimens. AJR Am J Roentgenol 1992;159:357–360.
81. Dennis MG, Fox JA, Alford JW, Hayden JK, Bach BR. Posterior cruciate ligament reconstruction: current trends. J Knee Surg 2004;17:133–139.
82. Dandy DJ, Pusey RJ. The long-term results of unrepaired tears of the posterior cruciate ligament. J Bone Joint Surg Br 1982;64:92–94.
83. Höher J, Scheffler S, Weiler A. Graft choice and graft fixation in PCL reconstruction. Knee Surg Sports Traumatol Arthrosc 2003;11:297–306.
84. Sherman PM, Sanders TG, Morrison WB, Schweitzer ME, Leis HT, Nusser CA. MR imaging of the posterior cruciate ligament graft: initial experience in 15 patients with clinical correlation. Radiology 2001;221:191–198.
85. LaPrade RF, Engebretsen AH, Ly TV, Johansen S, Wentorf FA, Engebretsen L. The anatomy of the medial part of the knee. J Bone Joint Surg Am 2007;89:2000–2010.
86. De Maeseneer M, Van Roy F, Lenchik L, Barbaix E, De Ridder F, Osteaux M. Three layers of the medial capsular and supporting structures of the knee: MR imaging-anatomic correlation. Radiographics 2000;20(Spec No):S83–S89.
87. Warren LF, Marshall JL. The supporting structures and layers on the medial side of the knee: an anatomical analysis. J Bone Joint Surg Am 1979;61:56–62.
88. Malone WJ, Verde F, Weiss D, Fanelli GC. MR imaging of knee instability. Magn Reson Imaging Clin N Am 2009;17:697–724, vi–vii.
89. Hughston JC, Andrews JR, Cross MJ, Moschi A. Classification of knee ligament instabilities. Part I. The medial compartment and cruciate ligaments. J Bone Joint Surg Am 1976;58:159–172.
90. Garvin GJ, Munk PL, Vellet AD. Tears of the medial collateral ligament: magnetic resonance imaging findings and associated injuries. Can Assoc Radiol J 1993;44:199–204.
91. Wen DY, Propeck T, Kane SM, Godbee MT, Rall KL. MRI description of knee medial collateral ligament abnormalities in the absence of trauma: edema related to osteoarthritis and medial meniscal tears. Magn Reson Imaging 2007;25:209–214.
92. Wang JC, Shapiro MS. Pellegrini-Stieda syndrome. Am J Orthop 1995;24:493–497.
93. Niitsu M, Ikeda K, Iijima T, Ochiai N, Noguchi M, Itai Y. MR imaging of Pellegrini-Stieda disease. Radiat Med 1999;17:405–409.
94. Bosworth DM. Transplantation of the semitendinosus for repair of laceration of medial collateral ligament of the knee. J Bone Joint Surg Am 1952;34:196–202.
95. Recondo JA, Salvador E, Villanua JA, Barrera MC, Gervas C, Alustiza JM. Lateral stabilizing structures of the knee: functional anatomy and injuries assessed with MR imaging. Radiographics 2000;20(Spec No):S91–S102.
96. Miller TT, Gladden P, Staron RB, Henry JH, Feldman F. Posterolateral stabilizers of the knee: anatomy and injuries assessed with MR imaging. AJR Am J Roentgenol 1997;169:1641–1647.
97. Munshi M, Pretterklieber ML, Kwak S, Antonio GE, Trudell DJ, Resnick D. MR imaging, MR arthrography, and specimen correlation of the posterolateral corner of the knee: an anatomic study. AJR Am J Roentgenol 2003;180:1095–1101.
98. Maynard MJ, Deng X, Wickiewicz TL, Warren RF. The popliteofibular ligament. Rediscovery of a key element in posterolateral stability. Am J Sports Med 1996;24:311–316.
99. Yu JS, Salonen DC, Hodler J, Haghighi P, Trudell D, Resnick D. Posterolateral aspect of the knee: improved MR imaging with a coronal oblique technique. Radiology 1996;198:199–204.
100. Brown TR, Quinn SF, Wensel JP, Kim JH, Demlow T. Diagnosis of popliteus injuries with MR imaging. Skeletal Radiol 1995;24:511–514.
101. Levy BA, Stuart MJ, Whelan DB. Posterolateral instability of the knee: evaluation, treatment, results. Sports Med Arthrosc 2010;18:254–262.

PRINTED HOME STUDY EDUCATIONAL SEMINARS

Qty.	Vol.	CE	Home Studies Title
	1.1	3.5	Functional MRI: Capabilities and Limitations
	1.2	3.0	Concepts in MR Physics
	2.1	3.5	Considerations in Low Field MRI
	2.2	3.0	Directions in Basic Cardiac Imaging
	2.3	3.0	Directions in Advanced Cardiac Imaging
	2.4	1.5	The Basics of Magnetic Resonance Angiography
	3.1	3.0	Introduction to Spectroscopy
	3.2	1.0	Renal MR Imaging
	3.3	3.0	A Primer on MR Pulse Sequences
	3.4	2.5	Artifacts Encountered in Abdominal MRI
	4.1	3.0	Safety Aspects in MRI
	4.2	3.0	Directions in MRI of the Liver
	4.3	2.0	MR Techniques in the Evaluation of the Uterus
	4.4	3.0	Fundamental Principles for MR Imaging of the Brain
	5.1	2.5	Atlas of Cranial Neuroanatomy
	5.2	2.0	MRI of the Ankle & Foot
	5.3	3.0	MR Imaging of the Breast
	5.4	1.0	Diffusion-Weighted Imaging of the Brain
	6.1	1.0	Directions in MRA of the Abdominal Aorta and Lower Extremities
	6.2	3.5	Fundamental Principles of MR Imaging of the Head, Neck, and Spine
	6.3	1.5	Advances in Interventional MRI
	6.4	1.5	Diffusion-Weighted MR Imaging of the Pediatric Brain
	7.1	2.0	The Role of Neuroimaging in the Diagnosis of Alzheimer's Disease
	7.2	2.5	Cardiovascular MRI: Update I
	7.3	2.5	K-Space in the Clinic
	7.4	3.0	MR Imaging and Spectroscopy of the Prostate
	8.1	1.0	Atlas of Knee Anatomy
	8.2	2.0	Cardiovascular MRI: Update II
	8.3	2.5	Update: Safety in MR Examinations
	8.4	2.0	Parallel MR Imaging

Qty.	Vol.	CE	Home Studies Title
	9.1	3.0	MRI of Breast Cancer: Update I
	9.2	2.5	MR Atlas of the Shoulder
	9.3	3.0	Exploring Magnetic Field Strengths: Challenges and Opportunities
	9.4	4.0	MRI of Breast Cancer: Update II
	10.1	4.0	MR Imaging of Perfusion
	10.2	3.0	MR Imaging Artifacts:Appearance, Cause & Cure
	10.3	4.0	Techniques in Cardiovascular MR Imaging
	10.4	3.0	MRI of the Brain
	11.1	4.0	Update: Musculoskeletal MRI*
	11.2	2.5	Contrast Media in MRI Examinations*
	11.3	2.0	Head and Neck MRI at 3.0T
	11.4	3.0	MR Imaging of the Abdomen*
	12.1	3.0	Contrast-Enhanced Musculoskeletal MR Imaging
	12.2	3.0	Neuro MRI: Principles and Protocols*
	12.3	2.0	MR Imaging of the Spine*
	12.4	3.0	MR Imaging of the Liver*
	13.1	3.0	MR Imaging Sequences: Gradient-Recalled Echo (GRE)*
	13.2	3.5	Techniques in Cardiac MR Imaging*
	13.3	2.5	Phase Contrast MR Imaging: Techniques and Applications*
	13.4	2.0	MRI of Spinal Cord Lesions*
	14.1	3.0	Breast MRI: DCIS and Skin Lesions*
	14.2	3.5	Pediatric Magnetic Resonance Imaging*
	14.3	2.5	MR Imaging Physics Tutorial*
	14.4	2.5	Safety and Screening in MRI*
	15.1	2.0	MR of the Abdomen: Kidney*
	15.2	2.5	3D Musculoskeletal MR Imaging*
	15.3	2.5	MR Physics: Gradient Echo & Parallel Imaging*
	15.4	1	MRI Atlas of the Abdomen*

All home study educational seminars following Volume 15.4 will be available ONLINE ONLY.

*Home Study Educational Seminars available online at no cost to SMRT members.

HOME STUDY EDUCATIONAL SEMINARS ORDER FORM

Back issues of SMRT educational seminars are for sale to SMRT members only!

YOU MAY ORDER PAST ISSUES OF HOME STUDY EDUCATIONAL SEMINARS ONLINE:

http://cds.ismrm.org/protected/ehs/hsorder.htm

TO ORDER BY MAIL, PLEASE FILL OUT AND MAIL THIS FORM, INCLUDING YOUR QUANTITY AND CHOICE OF ISSUES FROM PREVIOUS PAGE

CALCULATE YOUR ORDER HERE

Total quantity ordered: _____ x US$25 each = $_____ Subtotal = US$_____

SHIPPING:

Shipping is included on orders of four volumes or less. **Shipping is charged on orders of five volumes or more.** We will contact you with the shipping cost before we process your order. No orders will be processed before you have confirmed the actual shipping cost.

PAYMENT OPTIONS & BILLING INFORMATION

PAYMENT WITHIN USA:

Personal checks, money orders, cashier's checks and company checks are acceptable. Institutional purchase orders are acceptable and will be invoiced, but payment must still be received prior to shipment.

PAYMENT FROM OUTSIDE USA:

Checks: The check must be payable "to" (NOT "through") a U.S. bank in U.S. Dollars. The check must be imprinted with the computer encoding and routing information authorized by the American Banking Association.

Traveler's Checks: Traveler's checks in U.S. dollars for the exact amount, properly counter-signed, are acceptable.

International Money Order: The money order must be in U.S. dollars and be imprinted with the computer encoding and routing information authorized by the American Banking Association. U.S. dollar International Postal Money Orders imprinted as stated above are acceptable.

Wire: Wire payments are not accepted.

SMRT Member ID# (REQUIRED)_____

Name_____

Address_____

City_____State/Province_____Postal Code/ZIP + 4_____Country_____

Phone_____Fax_____E-mail_____

❒ Credit Card: ❒ VISA ❒ MasterCard ❒ AMEX ❒ Discover

(Credit card orders may be faxed directly to SMRT: +1 510 841 2340)

Card Number: _____Expiration Date:_____Security Code:_____

Billing Address_____Billing Zip + 4/Postal Code:_____

Signature:_____

WE ARE A NETWORK OF KNOWLEDGE

SMRT – A Global Community

The Section for Magnetic Resonance Technologists (SMRT) of the International Society for Magnetic Resonance in Medicine (ISMRM) is the leading non-profit organization that provides an international forum for education, information and research in magnetic resonance for technologists and radiographers throughout the world.

The SMRT was established by technologists, clinicians and scientists of the ISMRM as a forum for technologists and radiographers to share their expertise and educational resources, with a common goal of improving healthcare for people worldwide.

As an organization, we are committed to promoting communication and the dissemination of cutting-edge MR developments. The objective of the SMRT is to advance education and training, while striving to promote a high level of knowledge and professionalism in the field of MR technology and radiography.

SMRT Member
Filip De Ridder, R.N., FSMRT
Universitair Ziekenhuis Brussel

SMRT

ISMRM
SECTION FOR MAGNETIC RESONANCE TECHNOLOGISTS

2030 ADDISON STREET
SUITE 700
BERKELEY, CALIFORNIA, 94704 USA
TEL: +1 510 841 1899
FAX: +1 510 841 2340
INFO@ISMRM.ORG/SMRT